Characterization and Mitigation of Solidification Defects in Aluminum Casting and Welding

Dissertation

Presented in Partial Fulfillment of the Requirements for the Degree Doctor of Philosophy in the Graduate School of The Ohio State University

By

Nicole Trometer, B.S., M.S.

Graduate Program in Department of Materials Science and Engineering

The Ohio State University

2024

Dissertation Committee:

Dr. Alan Luo, Advisor

Dr. Glenn Daehn

Dr. Xun Liu

Dr. Ahmet Selamet

Abstract

Aluminum is increasingly favored in the automotive sector for its favorable mechanical properties and good strength-to-weight ratio. Laser welding finds utility in electric vehicle battery assemblies, while high pressure die castings (HPDC) are used in vehicle body construction. Nonetheless, defects pose a risk to the mechanical robustness of aluminum welds and cast parts. These defects include hydrogen porosity, entrapped air, and externally solidified crystals (ESCs). In this study, defects in die-cast and welded aluminum were investigated to understand their formation mechanisms and to explore methods for their prevention.

Laser welding of aluminum and copper is commonly used in the battery assemblies of electric vehicles. However, aluminum is prone to forming hydrogen porosity when welded. The investigation of hydrogen porosity in aluminum welds involved the utilization of scanning electron microscope (SEM), energy dispersive spectroscopy (EDS), microcomputed tomography (μ-CT), and LECO® analysis. It was observed that the oxide layer on anodized aluminum served as heterogeneous nucleation sites for hydrogen porosity. Anodized aluminum can contribute to increased hydrogen content in the liquid phase. As liquid aluminum solidifies, hydrogen is forced into the melt, leading to a state of supersaturation in the liquid. This supersaturation prompts the nucleation and growth of hydrogen porosity. Additionally, a cellular automaton (CA) model was expanded to predict hydrogen porosity under different

hydrogen concentrations, laser speeds, and powers. To mitigate hydrogen porosity, it is necessary to either improve the cleaning process of the anodized aluminum or utilize an alternative corrosion-resistant material.

Die-cast aluminum is frequently employed to reduce vehicle weight. However, the turbulent flow inherent in the die casting process can easily entrap air, leading to gas porosity. The impact of vacuum on entrapped air during die casting was investigated using a combination of MAGMASOFT® and ProCAST flow simulations, water analog experiments, and die casting trials. The water analog experiments demonstrated consistent repeatability and concurred with the flow simulations. It was observed that the introduction of vacuum resulted in a reduction in the quantity of entrapped air and porosity within the samples. Samples cast with a strong vacuum, below 100 mbar, exhibited greater density and enhanced mechanical properties compared to those cast with a weaker vacuum or none at all.

Externally solidified crystals (ESCs) are defects characterized by a distinct microstructure compared to the matrix. Two types of ESCs are commonly found in die-cast samples. Type I ESCs are very large dendrites, approximately 150 µm in size. Type II ESCs have a finer microstructure within the matrix and exhibit a clear boundary with it. This boundary can cause a signification reduction in elongation. The formation mechanism of ESCs was investigated using computer simulations, water analog experiments, and die casting trials, revealing that ESCs primarily form in the shot sleeve after pouring. Type II ESCs form on the walls of the shot sleeve, benefiting from a rapid cooling rate that encourages a finer microstructure. Conversely, Type I ESCs form further away from the shot sleeve wall, where a slower cooling rate facilitates their growth into larger dendrites. Turbulence during the filling process

breaks up both the large Type II and Type I ESCs, pushing them into the die cavity. Increasing the melt temperature decreases the occurrence of ESCs in die-cast samples.

In conclusion, this research offers valuable insights into optimizing the performance of aluminum in automotive applications.

This is dedicated to my friends and family for their support.

Acknowledgments

First of all I want to thank everyone who has supported me throughout graduate school. Just because I do not mention everyone here does not mean I am not eternally grateful.

First I would like to thank my advisor Dr. Alan Luo for his support and guidance throughout my studies. I would also like to thank my committee members Dr. Glenn Daehn and Dr. Xun Liu for their support and suggestions for improvement.

I would also like to thank the group members of the Lightweight Materials and Manufacturing Research Lab for all of their support. Especially Dr. Thomas Avey, Dr. Janet Meier, Dr. Jianyue Zhang, Dr. Matt Hartsfield, Dr. Michael Moodispaw, and Emmanuel Chen for their support and helpful discussions. I also want to thank my undergraduate assistant Rui Wang who has helped my with sample preparation in these last few months. I truly could not have gotten to this point in graduate school and life without their support.

I also want to thank the industry partners who have supported my projects and research. Specifically I want to thank Larry Godlewski from Ford and Dr. Wayne Cai from GM for their support and for giving me the opportunity to study die casting and welding of aluminum.

Additionally, I want to thank the staff in the OSU MSE department, at the Center for Design and Manufacturing Excellence (CDME), and at the Center for

Electron Microscopy and Analysis (CEMAS) for all of their help. Specifically I want to thank Wayne Papageorge for his support for helping me prepare my samples and Jose Smokowski for his help in analyzing the data from the micro-CT scans.

Ford Motor Company, General Motors, and the North American Die Casting Association have provided financial support for my research.

Lastly I want to thank my family and friends for their support of my journey through graduate school. Specifically my friends Stephanie Almquist and Irem Efe as both supportive friends and roommates. My mom Lisa, my aunt Lindy, and my cousin Nathaniel for their love and encouragement even though they do not fully understand what I do. I also want to thank my cat Cinder for her love and cuddles. Finally, I want to thank my dad for this unwavering support and encouragement because even though he passed away before I started graduate school, the knowledge of his pride and his love has given me the strength to get to this point in graduate school.

Vita

2019-present	PhD, Materials Science and Engineering, The Ohio State University.
2019-2022	M.S. Materials Science and Engineering, The Ohio State University, USA
2014-2019	B.S. Materials Science and Engineering, University of Florida, USA

Publications

Research Publications

Nicole Trometer, Buwei Chen, Michael Moodispaw, Wayne Cai, Teresa Rinker, Shardul Kamat, Zachary Velasco, Alan A. Luo "Modeling and Validation of Hydrogen Porosity Formation in Aluminum Laser Welding". *Accepted to Journal of Manufacturing Processes*, June 2024.

Trometer, N., Godlewski, L. A., Prabhu, E., Schopen, M., Luo, A. A. "Effect of Vacuum on Die Filling in High Pressure Die Casting: Water Analog, Process Simulation and Casting Validation". *International Journal of Metalcasting*, 2023.

Zhang, J., **Trometer N.**, Luo, A.A., "An Investigation of Externally Solidified Crystal Formation in Aluminum High Pressure Die Casting", *NADCA Transactions*, 2022.

Trometer, N., Huang, X., Cinkilic, E., Luo, A.A., Godlewski, L., Prabhu, E., Zindel, J., "Water Analog Experiments and Simulation of Vacuum High-Pressure Die Casting of Aluminum", *NADCA Die Casting Congress*, T20-011 2020.

Fields of Study

Major Field: Department of Materials Science and Engineering

Table of Contents

Page

List of Tables

List of Figures

Figure **Page**

Chapter 1: Introduction

Lightweighting is crucial for the automotive industry, as it can improve the fuel efficiency and reduce the energy required for driving. Aluminum is commonly used for this purpose due to its higher strength-to-weight ratio compared to steel.

Another significant trend in the automotive industry is the replacement of gas-powered vehicles with electric vehicles. Aluminum's excellent electrical conductivity makes it particularly desirable for use in battery joint in electric vehicles.

However, both of these applications of aluminum encounter defects. These defects include air entrapment, hydrogen porosity, shrinkage porosity, inclusions, blisters, hot/cold cracks, externally solidified crystals (ESCs), and keyhole collapse porosity. Hydrogen porosity, in particular, can manifest in both cast and welded aluminum. This chapter provides an overview of laser welding and high-pressure die casting of aluminum, highlighting these defects. Additionally, it discusses gaps in the existing literature on these topics.

1.1 Laser Welding of Aluminum

Laser welding employs a focused laser beam to raise the temperature of metals, allowing them to join. This technique is utilized to bond aluminum and copper foils for battery applications in electric vehicles. It offers a high-quality joining method

with minimal distortions post-welding [3]. However, porosity can develop in the joints, often due to keyhole fluctuations or hydrogen entrapment within the solidifying metal [4].

Keyhole collapse, a well-documented cause of porosity in the literature, results in irregularly shaped porosity [5]. This phenomenon occurs during keyhole mode welding, a high-energy process operating at approximately 10^5 W/cm^2 [6]. When the keyhole collapses, any gas present is trapped, leading porosity [7]. Additionally, keyhole collapse can cause air entrapment within the welds [8].

Porosity in welds may also stem from the evaporation of low-melting temperature elements such as magnesium and zinc [9]. These pores can be distinguished by a diminished magnesium, or other element, concentration within the weld zone [10]. However, in alloys containing fewer low-boiling temperature elements, this form of porosity is less prevalent [11].

1.1.1 Hydrogen Porosity in Aluminum Laser Welds

As previously noted, hydrogen porosity is a common occurrence in both the casting and welding of aluminum. Typically, hydrogen pores exhibit a round shape with smooth edges [5], generally measuring smaller than 1 µm in diameter [10]. The nucleation of hydrogen pores arises from the reduction in hydrogen solubility within aluminum upon solidification [12]. Figure 1.1 showcases the variation in hydrogen solubility with temperature, sourced from [1] and supplemented with insights from [2]. According to the graph, hydrogen solubility in aluminum diminishes by approximately 95% during the solidification process. Consequently, the hydrogen is expelled into the melt, leading to a state of supersaturation in the remaining liquid [13, 14, 5].

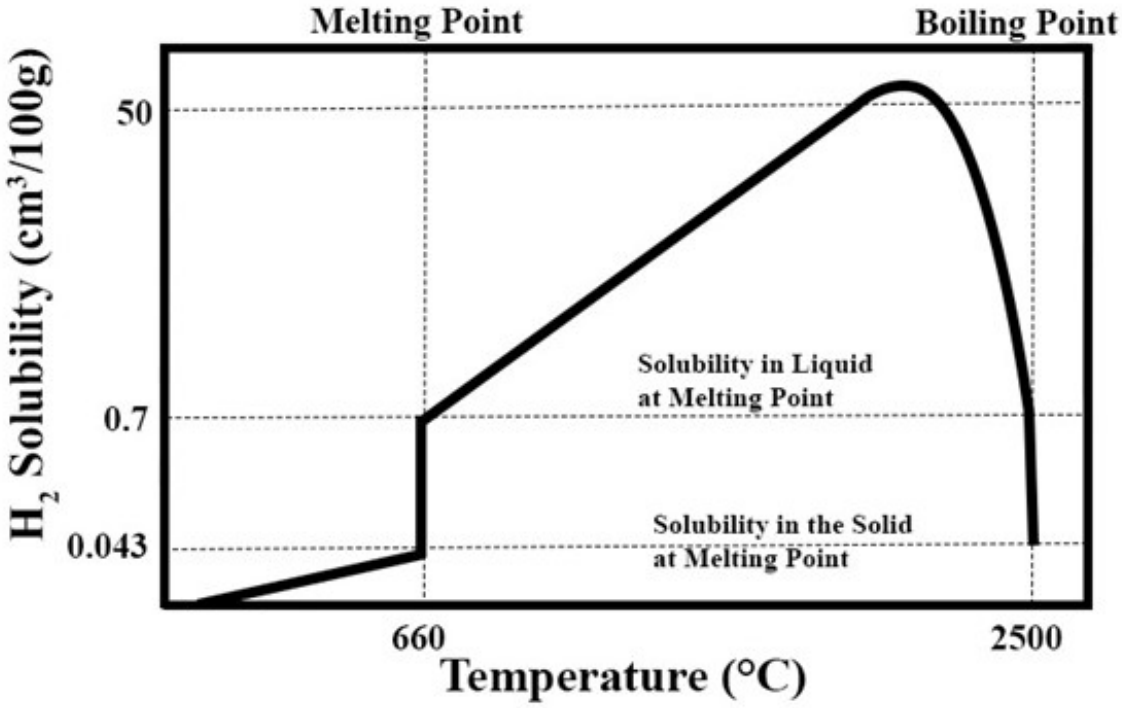

Figure 1.1: This figure depicts a schematic diagram illustrating the relationship between solubility of hydrogen in aluminum and temperature, incorporating date from [1] and supplementary information from [2]

Hydrogen porosity can reduce both the strength [15] and formability of welded joints [16]. Notably, researchers have observed rounded porosity on fracture surfaces [5]. In a separate investigation, it was noted that samples welded without shielding gas exhibited lower tensile strength compared to those welded with shielding gas [17]. This reduction in strength can be attributed to the decreased load-bearing area caused by porosity [18] particularly impacting the effective joint area in welding scenarios [4]. Consequently, reducing or eliminated porosity is crucial for achieving superior joint quality.

One method to reduce porosity during welding is the use of shielding gas [17, 19]. By enveloping the weld area, the shielding gas acts as a barrier, preventing the ingress of hydrogen and other atmospheric gases that might otherwise become trapped within the weld [17]. However, it's noteworthy that porosity can still arise from the rejection of shielding gas, akin to the formation of hydrogen porosity [20]. Helium is often favored as a shielding gas due to its propensity to generate less porosity [20]. Moreover, accurately modeling the impact of shielding gas in simulations poses challenges, potentially complicating the precise depiction of the welding process [21].

The various laser parameters employed during welding significantly influence the defects observed within the weld zone. Lowering the laser power can result in the formation of small porosities, yet it's the laser speed that predominantly impacts porosity levels [22]. The laser power influences the cooling rate of the weld; thus, higher power settings can lead to increased porosity due to reduced time for pores to escape before solidification, owing to the faster cooling rate [23]. Moreover, higher laser power levels entail greater metal melting during welding, [24], resulting in wider and deeper weld pools [25]. Conversely, increasing the laser speed generally reduces

porosity [22], albeit at the expense of less time for pore to escape from the weld pool, owing to the shorter duration of molten state [26, 25]. Paleocrassas and Tu [27] observed significant porosity in welds produced at slow laser speeds. Additionally, employing a laser beam that oscillates, rather than moving linearly, can enhance weld quality [28].

1.1.2 Anodized Aluminum

Anodized aluminum is frequently used in welding due to its corrosion-resistant properties [29]. This material is produced through an electrochemical process involving acid, inducing the formation of a protective oxide layer [29]. The oxide layer is characterized by numerous pores capable of absorbing hydrogen [20], with hydrated aluminum oxide having the potential to release hydrogen into the molten aluminum during welding[11, 20]. While high-temperature formed oxide proves resistant to removal by heating, oxide formed during storage at room temperature can be eliminated through heating [12]. Typically, prior to welding, this oxide layer is removed via polishing [23], resulting in diminished porosity in the final weld [30, 11].

An alternative approach involves breaking the oxide layer on the aluminum surface before welding using ultrasonic vibration [31]. Researchers observed that welds prepared with oxide broken prior to welding exhibited reduced porosity compared to those without ultrasonic vibration [31]. Furthermore, if this oxide layer is not removed, it can be broken apart by the laser during welding, releasing hydrogen into the melt pool.

The presence of an oxide layer on the welded surface can lead to a rise in porosity levels [32]. This is attributed to the oxide fragments broken by the laser, which can

serve as heterogeneous nucleation sites for porosity formation [15, 31]. According to classical nucleation theory, homogeneous nucleation of hydrogen porosity in pure aluminum is highly improbable [33]. Additionally, those oxide fragments may also function as initiation sites for cracks [34].

Extensive research has examined the correlation between aluminum oxide films and hydrogen porosities, particularly in castings [35, 36, 37]. Bifilms, which are folded oxide films, are widely believed to contribute to porosity formation in aluminum castings [35]. A comparable mechanism may also be at play during the welding process of anodized aluminum.

1.1.3 Cellular Automaton

Modelling is employed to gain a better understanding of the laser welding process. Vital information, such as fluid flow and temperature gradients, can be challenging to obtain from experiments [7], but can be effectively derived through computer modeling. Cellular Automaton (CA) can be used to predict the porosity and grain structure post-processing [14]. CA utilizes both local and global equations to simulate the evolving grain structure during solidification. The CA domain is divided into 3D cubic cells, with each cell's state determined by its six nearest neighbors [38]. Zhang et al [39] employed a lattice Boltzmann cellular automaton-finite difference method to simulate gas porosity formation and movement. However, their code does not account for a moving heat source, which is crucial for grain growth in laser welding [39]. CA simulations can be integrated with finite element analysis (FEA) and other models to enhance the efficiency of CA code [40].

Gas porosity nucleation is based on hydrogen solubility in molten aluminum, as discussed in Section 1.1.1. Pores nucleate when the hydrogen concentration in the liquid reaches the solubility limit [14]. The growth of these pores depends on the availability of hydrogen in the surrounding melt; when the hydrogen concentration falls below the local saturation level, the pores can no longer grown [14]. As grains grow simultaneously with the pores, they can block pore growth, leading to irregularly shaped pores [41]. The initial hydrogen concentration's impact on the nucleation and growth of hydrogen porosity can be simulated [41].

1.2 High Pressure Die Casting of Aluminum

In high-pressure die casting (HPDC), molten metal undergoes a rapid process where it's poured into a shot sleeve and then injected into a die cavity with significant speed and pressure. Prior to pouring, the molten metal is degassed to reduce the hydrogen content [42]. This pouring process, known as dosing, involves transferring the metal from a furnace into a cooler shot sleeve using a ladle typically made from ceramic or steel [43]. Once in the shot sleeve, the metal awaits the activation of the plunger, which drives it into the die cavity at high velocity. The duration the metal spends in the shot sleeve before plunger action commences is termed the dwell time [43]. The high speed of metal can cause it to separate from the leading edge upon entering the gate, a phenomenon referred to as the spray effect or atomization. Figure 1.2 depicts a water analog experiment demonstrating this effect. Following filling, intensification pressure is applied to ensure the metal solidifies under high pressure [43].

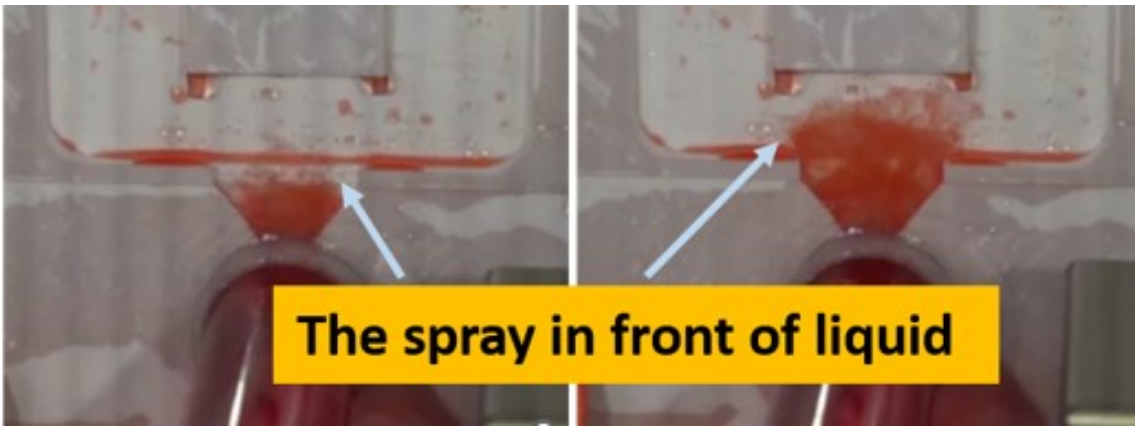

Figure 1.2: The spray effect observed in water analog experiments.

Die casting produces thin-walled, near-net-shape castings with excellent surface finish. HPDC parts are known for their outstanding mechanical properties, particularly elongation [43]. This process allows for the economical production of high-volume cast aluminum parts. Recently, there has been a trend toward manufacturing large single piece castings, especially for electric vehicles. However, the high turbulence, pre-solidification, and high velocities inherent in HPDC often result in defects in these parts.

1.2.1 Partial Shots in Die Casting

Partial Shots or short shots occur when a reduced amount of metal is cast, or when the plunger movement is halted before the end of the shot, resulting in an incomplete filling of the die casting [44]. The flow of metal is frozen, showing the flow front. This technique is used to observe the flow of metal during the filling process, allowing for comparisons with computer simulations or water analog experiments [45]. Partial shots are valuable for validating computer simulations and water analog experiments.

1.2.2 Defects in Die Casting of Aluminum

Defects are common in cast parts and include air entrapment, hydrogen porosity, shrinkage porosity, inclusions, blisters, hot and cold cracks, and externally solidified crystals (ESCs). As casting sizes increase, the impact of these defects becomes more significant. Numerous parameters in die casting influence the presence of defects. Larger castings experience more turbulent flow, which can result in a high incidence of defects. Additionally, controlling the temperature in larger volumes of metal is more challenging, which can further contribute to defects such as ESCs. The slow shot speed must also be carefully selected to ensure it is fast enough to minimized the formation of solidified metal, known as ESCs, in the shot sleeve, but not so fast that it creates a crashing wave, which traps air and increases gas porosity [46].

Porosity in Die Cast Aluminum

Air entrapment is a common issue in die-cast aluminum due to the turbulent flow of metal, which traps air [43]. Gas porosity can arise from die lubricants and the hydrogen content in molten aluminum [44], as well as from entrapped air during the filling process, especially when a wave in the shot sleeve crashes and traps air [47]. This gas porosity can lead to blistering during heat treatments, degrading the surface finish and potentially causing the part to be scrapped [48]. Gas porosity reduces the effective area within a sample, potentially causing heightened stress concentrations in the remaining metal. Consequently, this facilitates easier formation of cracks [49].

Using a vacuum in die casting can reduce porosity and enhance mechanical properties by removing air from the die cavity before filling, thereby minimizing the amount of air that can be entrapped when the metal enters the cavity [50, 43, 44]. Cao et al

[51] studied the impact of vacuum on an Al-Si-Cu HPDC alloy, testing three vacuum levels: 500 mbar, 200 mbar, and 100 mbar. They observed that samples subjected to the weakest vacuum exhibited lower mechanical properties and larger porosity. The porosity contributed to reduced stress-bearing area, thereby lowering the tensile strength [51].

Hu et al [52] investigated an Al-12Si-Fe alloy with vacuum levels of 275 mbar, 112 mbar, and 72 mbar. They found that stronger vacuum levels improved mechanical properties due to increased stress-bearing area during mechanical testing, attributed to fewer pores in the samples [52].

In another study, researchers examined vacuum die castings using absolute pressures of 1013 mbar, 200 mbar, and 100 mbar with an Al-9Si-3Cu alloy [53]. They explained that stronger vacuum reduced the formation of eddy currents, thereby decreasing the mixing of gas with the molten aluminum and subsequently reducing entrapped air [53].

Niu et al [54] compared vacuum-assisted die casting to conventional die casting and observed decreased gas porosity in samples cast under vacuum conditions. Similarly, Bo et al [55] investigated the mechanical properties of aluminum alloys cast under different vacuum strengths, finding improvements in ultimate tensile strength, yield strength, and elongation with the use of a vacuum [55].

Li et al [49] investigate the impact of vacuum on the mechanical properties of a Mg alloy, noting increases in tensile strength, yield strength, and elongation with the application of vacuum. They attributed this enhancement to the vacuum's role in removing air from the cavity during casting, while the fast shot speed compressed the

remaining air [49]. This process resulted in reduced air mixing with the molten metal during the injection [49].

The vacuum level achieved during casting can be influenced by varying the slow shot speed [56]. Cinkilic et al [42] used the varying slow shot speeds to change the vacuum strength during casting. This method allowed more time for vacuum levels to increase within the die cavity. However, this method could lead to more ESCs forming in the casting.

A super-vacuum, lower than 50 mbar in strength, has been shown to significantly diminish entrapped air and improve mechanical properties [57, 58]. Dong et al [57] conducted HPDC trials and achieved a vacuum as strong as 19 mbar. This strong vacuum substantially reduced porosity and resulted in improved mechanical properties compared to samples produced via conventional HPDC methods [57].

Shrinkage porosity occurs due to the contraction of aluminum during solidification, and feeding issues prevent additional molten metal from filling the resulting voids [59]. Unlike gas porosity, shrinkage porosity is often narrow and sharp, leading to stress concentrations and providing sites for crack nucleation [60]. These shrinkage pores can connect to form extensive porous regions, creating pathways for crack propagation and reducing mechanical strength [60]. Additionally, gas porosity can exacerbate shrinkage porosity, as shown in simulations with pure Mg alloy [61]. Researchers have found that cracks typically originate not from round gas pores, but from irregular shrinkage pores or combined gas-shrinkage pores [62]. This combined porosity negatively impacts the final casting by reducing the metal area available for stress and increasing areas of stress concentration [61].

Externally Solidified Crystals in Die Cast Aluminum

When the metal is poured into the shot sleeve during a die casting trial, the shot sleeve is at a much lower temperature than the molten metal [43]. This lower temperature causes the solidification of the metal on the shot sleeve wall. Helenius et al [63] made an industrial sized shot sleeve to determine the heat transfer coefficient (HTC) and the temperature variations in a shot sleeve when molten metal is poured into the shot sleeve. They found that the removal of an oxide layer on the surface of the shot sleeve can increase the HTC and turbulence during filling can reduce the HTC along with entrapping air [63]. The superheat of the metal was gone around 120 mm from the pour hole and the HTC was high at that location [63]. The solidification in the shot sleeve can lead to the formation of ESCs.

Externally solidified crystals (ESCs) are commonly found in die cast parts, but their formation mechanisms are not well understood. ESCs have a crystalline structure that is different from the matrix structure. Two types are commonly found in castings. Type I are primary alpha-Al dendrites larger than 10 µm in size [64]. While Type II are much larger than Type I, Type II generally have a width of 500 µm and a length of 1100 µm. Type II tend to have a much finer microstructure than the matrix and are separated from the matrix by a clear boundary. Type II are also called "Cold Flakes" in the literature.

A volume fraction of about 20% Type I ESCs is generally present in HPDC samples [65]. The ESCs tend to be mostly in the center of the castings [66]. Type I ESCs can lead to shrinkage porosity being present in the castings. Jiao et al [64] used CT and in-situ tensile tests to show a relationship between shrinkage porosity and ESCs. The presence of shrinkage porosity by ESCs can lead to a decrease in mechanical

properties [64]. Other research groups were more focused on the movement of ESCs and the forces that impact ESCs. Bi et al [67] developed a mathematical model to show the movement of ESCs during filling and the impact Type I ESCs have on the defect band. Han and Zhang [68] determined that the Magnus force causes pre-solidified dendrites (PSDs) to be more in the center of the casting and causes the skin to have fewer ESCs. The Magnus force is a force that cause the particle to be in the area of higher velocity [68]. Yuan et al [69] also found ESCs in the center of their casting and Wang and Xiong [56] also found a higher density of ESCs in the center of their specimens. These results agree with the results Timelli and Fabrizi found [66], they found fewer ESCs in the skin layer of the casting. Otarawanna et al [70] also found that Type I ESCs have a higher concentration in the center of the casting. The researchers also found that the amount of ESCs is higher closer to the gate [70]. Other researchers found that during the turbulent flow, the ESCs can break apart [68]. Smaller Type I ESCs have a lesser effect on the mechanical properties of the final casting.

Type II ESCs have an oxide film at the boundary [71]. The Type II ESCs can be reduced by increasing the shot sleeve temperature and the temperature of the molten metal [71]. Kopper and Monroe [71] varied the temperature in their computer simulations, however, they did not confirm their results with die casting trials. The molten metal temperature is important for Type II ESC formation because it determines how much superheat the metal has. Superheat is how high above the liquidus temperature the metal is cast at. A larger superheat means that more heat needs to be removed from the metal before it solidifies. The shot sleeve removes some heat and the metal starts to solidify in the shot sleeve, more solidification would occur with

Sample	Yield Strength (MPa)	Elongation (%)	Ultimate Tensile Strength (MPa)
Without Type II	159	3.3	270
With Type II	162	1.5	221

Table 1.1: An example of the effect of Type II ESCs on mechanical properties.

less superheat. Timelli and Fabrizi also found Type II ESCs in their die castings and determined that they were formed in the shot sleeve [66]. This method of formation is similar to that of Type I ESCs, but the difference of formation of fine or coarse microstructure is not well described in the literature.

The presence of Type II ESCs in the cast samples have a great effect on the mechanical properties. As seen in Figure 1.3 and Table 1.1, the elongation is greatly decreased when the fracture is caused by a Type II ESC. The boundary between the Type II ESC and the matrix creates a weak spot and can be a crack initiation spot. Figure 1.4 shows an example of a Type II ESC present on the fracture surface. This is a large ESC and takes up the center of the surface. Most ESCs take up a majority of the fracture surface and are easily visible without an imaging. The ESC shows brittle fracture while the surrounding material shows evidence of ductile fracture. This image was taken on a SEM in order to see more detail. Usually the elongation is around 1% if Type II are present. Type I ESCs typically have less of an effect on the mechanical properties.

Computer Modeling to Simulate Defects

Various software programs are available to simulate the casting process, including flow and solidification dynamics. ProCAST is a finite element modeling tool used for

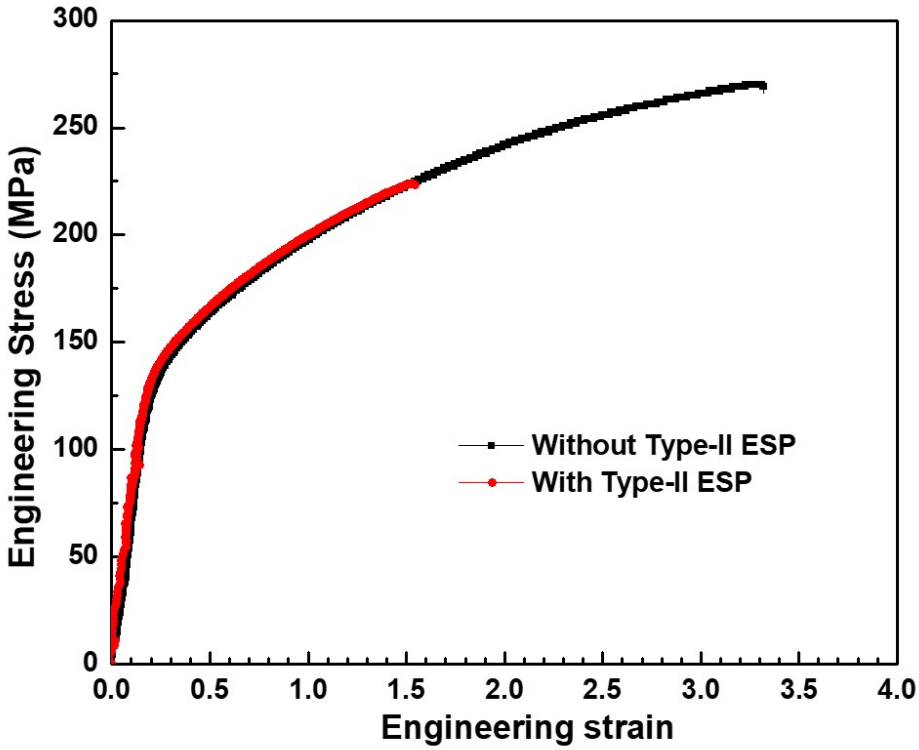

Figure 1.3: An example of the impact Type II ESCs have on mechanical properties.

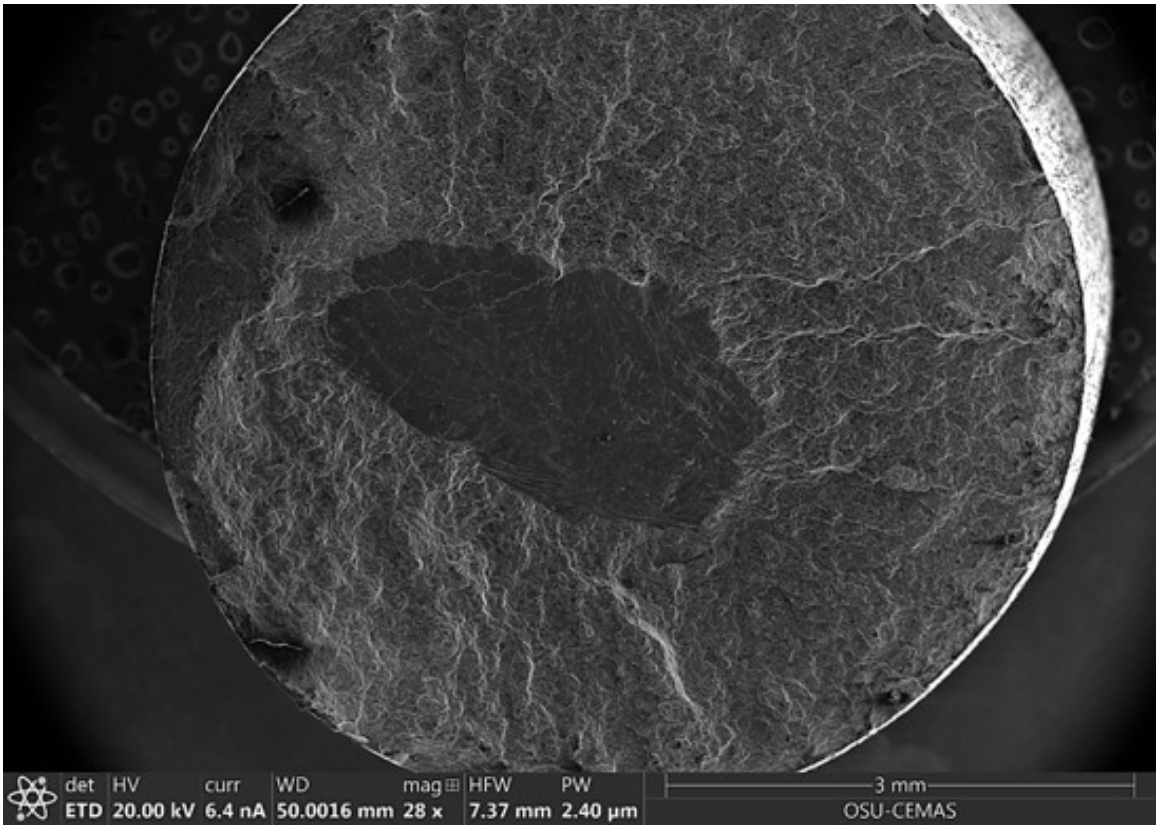

Figure 1.4: An example of a SEM image of a fracture surface with a Type II ESC present.

this purpose, employing the energy equation, continuity equation, and momentum equation to model the fluid flow and solidification [72]. Dou et al [46] utilized this software to simulate the entire HPDC process, from filling the shot sleeve to injecting the molten metal into the die cavity. Their findings indicated that metal solidified in the shot sleeve due to cooling along the sleeve walls [46], potentially forming Type II ESCs. Through computer simulations validated by HPDC trials, researchers determined that the optimal slow shot velocity should be between 0.4 and 0.6 m/s [46]. While this recommendation is specific to their model parameters, using computer simulations to determine appropriate speeds highly beneficial.

Other research groups have also utilized ProCAST to model the HPDC process, focusing on studying pre-solidification in the shot sleeve [73]. They identified that the most probable location for ESCs formation is at the end of the shot sleeve near the wall, where the temperature gradient is the most significant [73]. To reduce the occurrence of ESCs, they suggest increasing the temperature of the molten metal [73], although this may introduce other challenges such as decreased die life. Additionally, computer modeling can be employed to simulate shrinkage porosity [74].

MAGMASOFT® stands as another widely utilized software for simulating the casting process. This finite volume method-based software employs the Navier-Stokes equation, energy equation, continuity equation, and finite differential equation to model fluid flow and solidification dynamics [75]. Jeong et al [76] employed the software to simulate the die casting of clutch housing products, successfully identifying shrinkage porosity within the castings. However, upon validation against HPDC trials, they observed inconsistencies between the predicted location of shrinkage porosity

in the simulation and its actual occurence in the HPDC specimens [76]. While computer simulations are valuable tools, their accuracy relies on validation through die casting trials.

Gunasegaram et al [77] utilized the software to simulate solidification within the shot sleeve, revealing that the fraction solid in the shot sleeve before initiating the shot was 12.5%. Similarly, Rudack et al [78] employed the same software to investigate the impact of dosing time and dwell time on ESC formation in the shot sleeve. They found that a shorter dwell time benefits casting quality by reducing metal solidification in the shot sleeve [78]. Consequently, the researchers recommended longer dosing times and shorter dwell times for optimal casting quality [78]. Casting software proves invaluable in determining optimal dosing and dwell times tailored to specific casting metals and mold geometries. However, most casting software overlook heat loss and solidification occurring in the ladle during dosing [78]. Hence, comparing the solidification results with samples from casting trials is necessary to ascertain the best dosing and dwell times that minimize the presence of Type I and II ESCs in the casting.

FLOW-3D is another casting software commonly used to model die casting. The code is a computational fluid dynamics (CFD) code. Koru and Serçe used FLOW-3D to model the effect of vacuum on porosity during die casting. Wang et al [79] used FLOW-3D to simulate the ladle pouring into the shot sleeve. They found that there was not a lot of temperature loss from the ladle, but the pouring rate had an impact on the wave and turbulence in the shot sleeve [79].

Water Analog Experiments

Water analog experiments are frequently employed to investigate flow dynamics during filling processes. These experiments serve to validate computer simulations

and provide a basis for comparison with die casting samples. Water is an effective analog because its kinematic viscosity at room temperature is similar to that of molten aluminum, resulting in comparable flow patterns [80]. To enhance visibility, food dye is often added to the water [81]. However, Hao et al [82] opted not to use food dye due to concerns that it might alter the water's surface tension.

in contrast, Zamora et al [83] conducted experiments with both clear and dyed water and found no observable difference in flow patterns. They used a device to detect the onset of water movement, which did not require dyed water to function effectively [83]. Nevertheless, dyed water facilitates easier observation of flow in video recordings. Additionally, another group measured the amount of entrapped air in the water using photoelectric switches [47], and several other methods for detecting entrapped air also necessitate the use of colored water.

Cleary et al [81] employed a pressurized accumulator operating at a constant 6 bar pressure to drive water into the mold. However, this setup posed challengers in controlling the speed of the water accurately due to the consistent pressure. Consequently, other experimental parameters became difficult to measure, complicating comparisons with computer models and introducing additional issues into the design [81].

Viswanath et al [84] utilized the FLOW-3D computer simulation model to complement their water analog experiments. However, they encountered discrepancies when comparing these experiments and simulations to magnesium die casting. The lower density of water compared to molten magnesium resulted in mismatched results, as water moved faster than molten magnesium [84]. This disparity also presents a challenge when comparing water analog experiments to molten aluminum casting.

To address this issue, some researchers, including Park [85], introduced glycerin into the water. Glycerin effectively reduced the density and viscosity of the water, bringing it closer to the characteristics of molten aluminum [85].

Garber [86] conducted water analog experiments to investigate the fluid movement within the shot sleeve and the influence of varying velocities on entrapped air. However, the study solely compared its findings to equations predicting water flow and omitted comparisons to cast samples [86].

Hao et al [87] employed water analog experiments to study atomization phenomena in die casting. However, due to the significant difference in surface tension between aluminum and water, equations had to be developed to extrapolate the experimental results to die casting trials [87]. The ability to observe atomized flow is a notable advantage of water analog experiments, as such phenomena are challenging to visualize directly during die casting processes.

1.3 Machine Learning

Machine learning (ML) is a valuable tool for predicting complicated interactions between many parameters. Die casting of aluminum is a complex process that involves many variables. Understanding which variables are important to defect formation and mechanical properties can greatly benefit the die casting industry. Therefore using a ML model to predict defects and mechanical properties could be beneficial. Kopper et al [88] found that the prediction of the ultimate tensile strength using machine learning and neural network regression was accomplished and was better than traditional predicting methods. Another potential use for machine learning is the prediction of Type II ESCs in die-cast samples.

1.4 Objectives

The main objective of this research is (1) to determine the mechanism of defect formation for hydrogen porosity, entrapped air, and externally solidification crystals and (2) to investigate methods to reduce the presence of these defects in aluminum laser welds and high pressure die casting samples.

1.5 Organization of this Thesis

This thesis is organized into 5 chapters. This first chapter is the introduction chapter. Chapter 2 is on the welding of commercially pure aluminum and understanding hydrogen porosity in the welds. Chapter 3 is about entrapped air and gas porosity during high pressure die casting of aluminum and how the use of a vacuum can reduce the amount of entrapped air. Chapter 4 is also about die cast aluminum, but this chapter focuses on externally solidified crystals and their formation mechanism. Chapters 2 - 4 are all organized as publications with an introduction, methods, results, and conclusion section. Section 4.6 is organized as an introduction to machine learning and methods of a project using machine learning to predict the presence of ESCs in die cast aluminum samples. Chapter 5 is the final chapter and will summarize the conclusions of all the chapters and present future work based on this work.

Chapter 2: Laser Welding of Aluminum

This is chapter that will discuss hydrogen porosity in aluminum laser welds and how the porosity is affected by welding anodized aluminum. FEA simulations, CA modeling and welding experiments are used to study the impact anodized aluminum, and hydrogen has on porosity formation in aluminum laser welds.

2.1 Introduction

Commercially pure aluminum welding finds applications in electric vehicles for their battery systems. Laser welding offers a reliable means of creating robust welds and stands out as an efficient technique for joining aluminum. Nevertheless, porosity may arise, leading to a reduction joint strength, as highlighted by [15]. Furthermore, the existence of porosity can diminish both the tensile shear strength [4] and the peel strength [34].

Porosity in welds results from various factors, including pores formed by keyhole collapse [30] and pores induced by entrapped hydrogen [4]. Hydrogen, originating from the atmosphere and other sources, can dissolve into the molten aluminum at elevated temperatures. As the aluminum cools post-welding, the solubility of hydrogen diminishes [13], leading to a hydrogen supersaturation in the remaining liquid [14]. Molten aluminum has a higher solubility limit of hydrogen than solid aluminum,

therefore when solidification occurs some of the hydrogen in the melt is rejected and forms gas porosity [89]. The expulsion of hydrogen from the solidified metal results in it supersaturated within the liquid phase. Such supersaturation initiates the nucleation and expansion of hydrogen porosity [12]. Due to the rapid cooling rates typical of laser welding, hydrogen becomes trapped [23], giving rise to gas porosity [90].

The solidified metal acts as a barrier, preventing the bubbles from escaping the weld pool [91]. Han et al [28] observed that deeper weld pools led to increased porosity due to prolonged bubble escape time. Nevertheless, upward-growing grains within the solidifying pool can air porosity expulsion given sufficient time [92]. However, Huang et al [19] noted slower bubble escape rates in aluminum alloys compared to Inconel alloys, resulting in heightened porosity. Miyagi et al [93] confirmed the predominance of hydrogen in gas pores within laser-welded pure aluminum by vacuum drilling into the pores. Similarly, Ono et al [32] identified O_2, H_2, He, CO and CO_2 in welds, with He (helium) originating from the shielding gas. Pastor et al [10] discovered microporosity in laser-welded aluminum alloys 5182 and 5754, attributing it to hydrogen supersaturation. Notably, this microporosity was observed in welds where the helium shielding gas had been bubbled through water beforehand [10].

Hydrogen in molten aluminum can originate from various sources. Firstly, aluminum can react with water vapor in the atmosphere, yielding hydrogen [94]. Moreover, the interaction of aluminum with water vapor generates hydrogen gas and aluminum oxide [5]. Additionally, aluminum oxide has the potential to form a hydrate [11], and the oxide layer on anodized aluminum may absorb water vapor during manufacturing or storage [17]. Due to aluminum oxide's higher melting point compared to aluminum, it remains solid during welding [94]. However, the application of a

laser can destabilize hydrated aluminum, causing it to decompose and and released additional hydrogen into the liquid aluminum [12, 94]. Moreover, Wang et al [22] observed the release of gas from SiC_p/6092 aluminum matrix composites during welding, contributing to porosity formation.

Aluminum oxide can act as nucleation sites for porosity [15]. Aoki et al [91] observed an increase in porosity in the weld region upon increasing the amount of aluminum oxide before welding. Similarly, Kwon et al [31] detected oxide adjacent to porosity in the weld zone when welding Al alloy 1060-H18 foils and tabs. Improper cleaning, failing to remove surface oxides prior to welding, led to porosity in weld joints, as Cheever et al [95] reported. Cleaning the samples before welding can remove surface contaminants that can introduce more hydrogen into the weld [20] and cause welds of poor quality [94].

Micro voids are frequently found alongside aluminum oxide [96]. Moreover, the correlation between aluminum oxide films and hydrogen porosities is extensively documented in aluminum castings, El-Sayed et al [35] observed oxide films to porosity in aluminum A365 alloy cast under reduced pressure. Similarly, Liu et al [36] discovered numerous pores containing aluminum oxide upon casting an Al-Si alloy.

Griffiths and Raiszadeh [37] visualized the growth of an air bubble using X-ray imaging in liquid commercially pure aluminum; hydrogen diffusion into the pore contributed to its expansion.

Developing models to simulate porosity and analyze the impact of various laser parameters on hydrogen porosity can offer valuable insights into its nucleation and growth. Zhou and Tsai [90] employed modeling techniques to predict porosity in laser welding processes.

A three-dimensional cellular automaton (CA) model has proven effective in predicting porosity and modeling grain structure across various applications, such as castings [14], ternary aluminum solidification [41], and assessing the influence of cooling rates [97] and other process parameters. Kang et al [23] utilized the CA-FE (finite element) method to anticipate grain growth and porosity evolution during the laser welding of 6061 aluminum alloy.

In a different approach, Zhang et al [39] employed a lattice Boltzmann-cellular automaton-finite difference model to simulate hydrogen porosity nucleation and growth during the solidification of an aluminum alloy. Their study revealed a coupling between hydrogen porosity and grain growth, grains interacting with the bubbles [39].

Current research is dedicated to understanding keyhole porosity collapse in laser welding [7], high-speed camera imaging of the keyhole during [98], and simulation of the keyhole formation [99, 21]. However, there is relatively less focus on porosity resulting from entrapped hydrogen and welding anodized aluminum.

In this study, a 3D cellular automaton model was developed to forecast hydrogen porosity and grain growth in laser welds. The investigation delved into the impact of hydrogen concentration in the liquid metal and pore nucleation density on the size and quantity of formed pores. Furthermore, the influence of varying laser speed and power on porosity was explored through finite element analysis (FEA) and CA modeling.

Validation of the model was conducted by welding commercially pure aluminum and anodized aluminum tabs. Microstructure analyses, including scanning electron

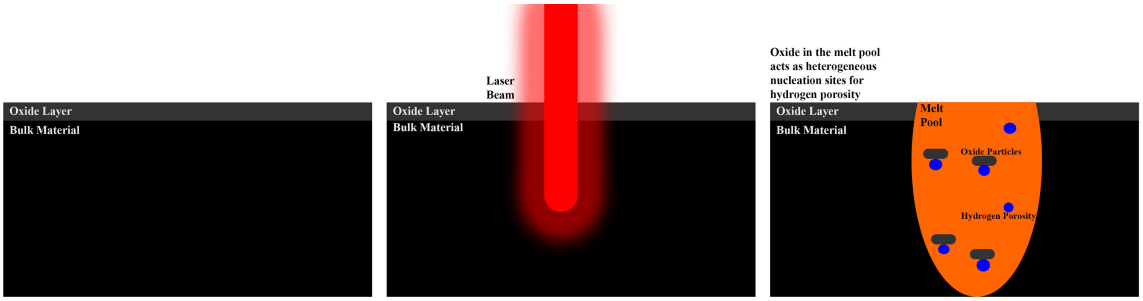

Figure 2.1: A depiction depicting the oxide layer present on anodized aluminum. During welding, the laser breaks up the oxide layer, leading to the formation of fragmented oxide particles. These fragmented particles serve as heterogeneous nucleation sites for hydrogen porosity.

microscopy, energy dispersive spectroscopy (EDS), X-ray microcomputed tomography, and LECO analysis for hydrogen measurements, were employed to characterize the porosity.

When welding anodized aluminum, the laser breaks apart the oxide layer with the broken oxide fragments serving as heterogeneous nucleation sites for hydrogen porosity. Figure 2.1 provides an illustration of this process.

2.2 Experimental Design

The welds were conducted using 0.2mm thick commercially pure aluminum. The tabs comprised bare Al 1100-O alloy and clear anodized Al 1145-H19 alloy. Both alloys consists of a minimum of 99.0% and 99.45% aluminum, respectively, with a maximum content of 0.05% Cu, Mn, Mg, Zn, Si, and Fe. A 2kW IPG YLS-2000 fiber laser with a wavelength was 1.065µm was employed for welding, connected to a 3D blackbird scanner. The spot size measured 115.9µm. The laser beam was positioned at a 90° angle to the test plate and was focused on the top surface. Tabs were welded

in lap joint configuration for similar and dissimilar welds. Similar welds included bare-to-bare tabs and anodized-to-anodized tabs. Dissimilar weld configurations comprised welding a bare tab welded to an anodized tab, and vice versa.

Figure 2.2(a) depicts the bare tabs welded together, while Figure 2.2(b) illustrates the anodized tabs welded together. Both configurations were welded using a laser power of 668 W and a laser speed of 330 mm/s. The bare tab has a shiny top while the anodized layer creates a dull finish. Figure 2.3(a) showcases a bare tab welded to an anodized tab, whereas Figure 2.3(b) exhibits an anodized tab welded to a bare tab. These welds were executed at a laser power of 668 W and a laser speed of 300 mm/s. The weld bead in Figure 2.3(a) is missing in many locations of the weld. The bare tab welded to an anodized tab did not create sound welds.

Figure 2.4(a) illustrates the channel flat fixture used for securing the tabs during welding, while Figure 2.4(b) depicts a cross-section of the tabs secured in the fixture. The laser moved along a straight path and no shielding gas was used. Laser powers of 668 W and 1170 W were employed, with laser speeds of 270, 300, 330, 360, and 600 mm/s.

The selection of laser powers and speeds aimed to assess the impact of varying these parameters while ensuring adequate weld penetration. Notably, the sample surfaces were not cleaned before welding. The welding conditions were deliberately chosen to induce some porosity. The aim of these experiments was to generate welds both with and without porosity to provide data for the CA model. As outlined in Section 2.1, pre-weld cleaning and the application of shielding gas are methods known to mitigate porosity in weld.

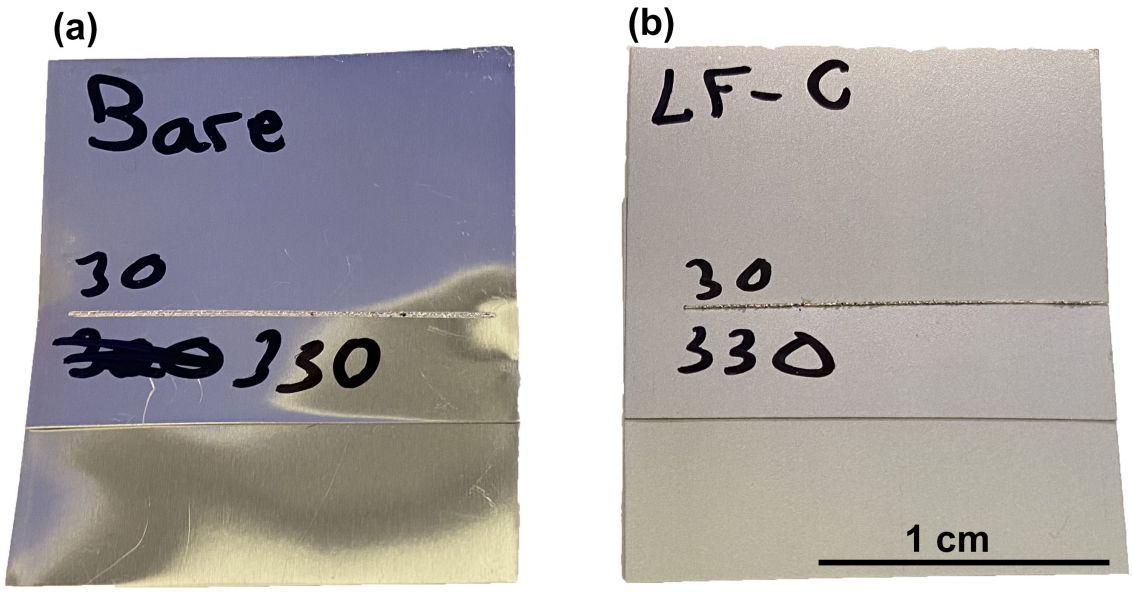

Figure 2.2: Both (a) and (b) were welded using a laser power of 668 W and a laser speed of 330 mm/s. In, (a) two bare tabs are welded together, while in (b) two anodized tabs are welded together.

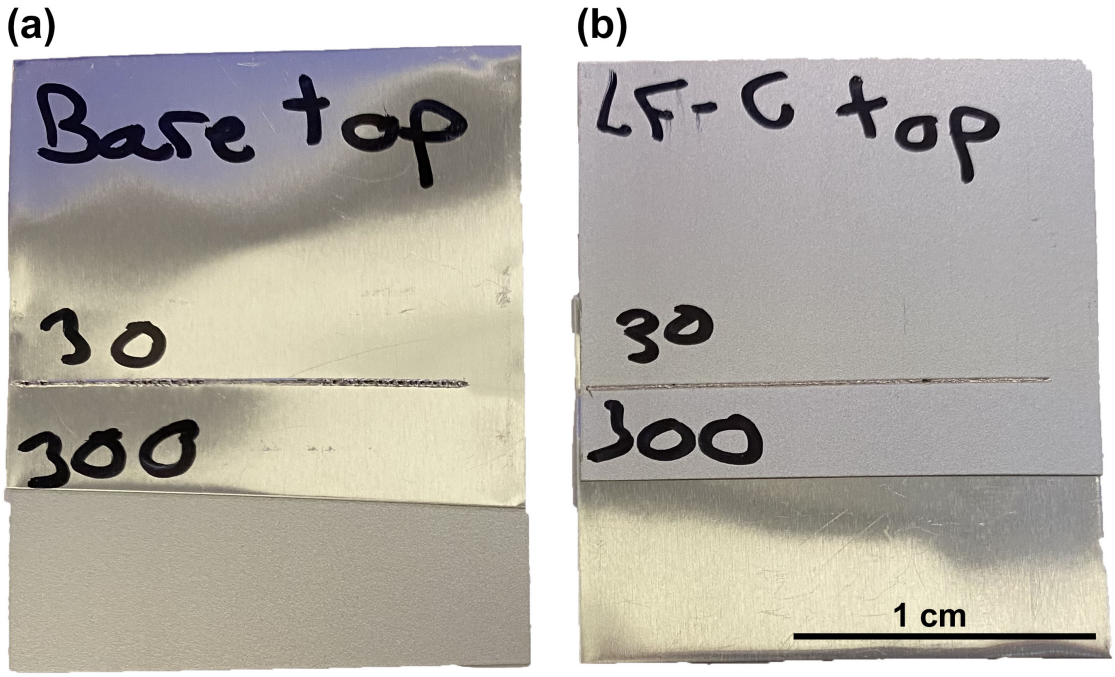

Figure 2.3: Both (a) and (b) were welded using a laser power of 668 W and a laser speed of 300 mm/s. In, (a) a bare tab is welded to an anodized tab, while in (b) an anodized tab on top is welded to a bare tab.

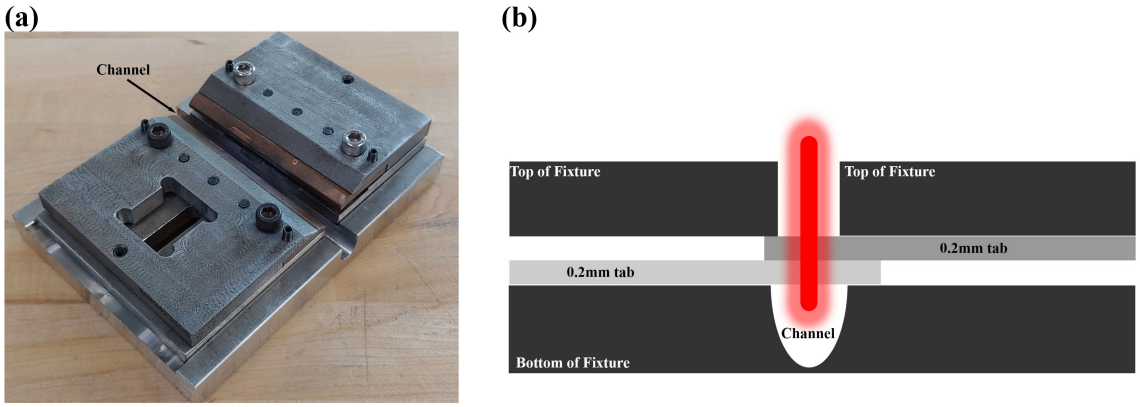

Figure 2.4: (a) The channel flat fixture utilized for welding, and (b) a cross-sectional view of the two tabs within the fixture during welding.

To test the effect of moisture on the amount of porosity, some samples were wrapped with a damp paper towel for five minutes prior to welding. After five minutes, the excess water was toweled off before the samples were welded. To test the effect of removing water from the samples. Other samples were preheated in an oven at 150 °C for 30 minutes prior to welding.

The welded samples underwent lap-shear testing using an Instron machine equipped with pneumatic side action grips, operating at a crosshead speed of 1 mm/min. General metallographic preparation techniques were employed to cut and prepare the samples. Some welds were subjected to etching using Keller's etchant.

Characterization of porosity in the weld seams and analysis of weld material composition were conducted using optical microscopy, scanning electron microscopy, energy dispersive spectroscopy, and microcomputed tomography (µ-CT). The µ-CT utilized a voxel size of 2 µm, scanning a total length of 20 mm, with data analysis performed using Avizo (version 2019.2).

Hydrogen content analysis was conducted using LECO® analysis, involving heating the sample to release hydrogen, which is then oxidized to form H_2O and detected using an infrared detector. Two samples were analyzed for each condition and welding speed. For half of the anodized samples, the anodized layer was removed by grinding with 240-grit sandpaper. Samples were then cut to a mass of 0.25 g for analysis, with both ground and as-received samples being examined.

2.3 Simulation Methods and Procedure

The thermal profile of the weld pool was simulated using a Finite Element Analysis (FEA) model. Subsequently, this thermal profile was integrated into the Cellular Automaton (CA) model by employing a fitting curve to match the temperature data.

2.3.1 FEA Thermal Simulations

The temperature profile for laser welding was obtained using SYSWELD v.17.0 (2021.0), a commercial FEA software dedicated to welding process simulation. The model consisted of 103,680 three-dimensional (3-D) elements. Laser powers of 668, 922, and 1170 W were utilized, along with laser speeds of 300 and 600 mm/s for comparison with experimental results. Additionally, speeds of 400 and 500 mm/s were employed to further explore the impact of laser processing speed.

The shape of the weld pool was determined by analyzing optical images of the weld pool obtained from experimental samples, which were specifically prepared to facilitate simulation. Thermal properties of pure aluminum from Simufact (2021) were employed for the simulation, as listed in Table 2.1. These properties, including density, thermal conductivity, and specific heat as functions of temperature are illustrated in Figure 2.5.

Figure 2.6 depicts a top view of the weld pool temperature profile alongside a segment of the mesh utilized in the FEA model.

2.3.2 CA Method Description

A cellular automaton (CA) model was employed to forecast porosity and grain structure in the context of aluminum laser welding. This model originates from a

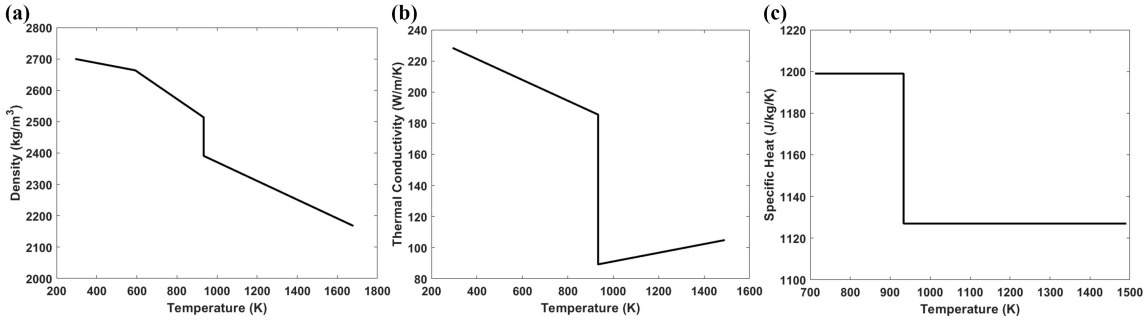

Figure 2.5: The properties utilized in the FEA simulation include (a) density versus temperature, (b) thermal conductivity versus temperature, and (c) specific heat versus temperature. These properties were sourced from *Simufact (2021)*.

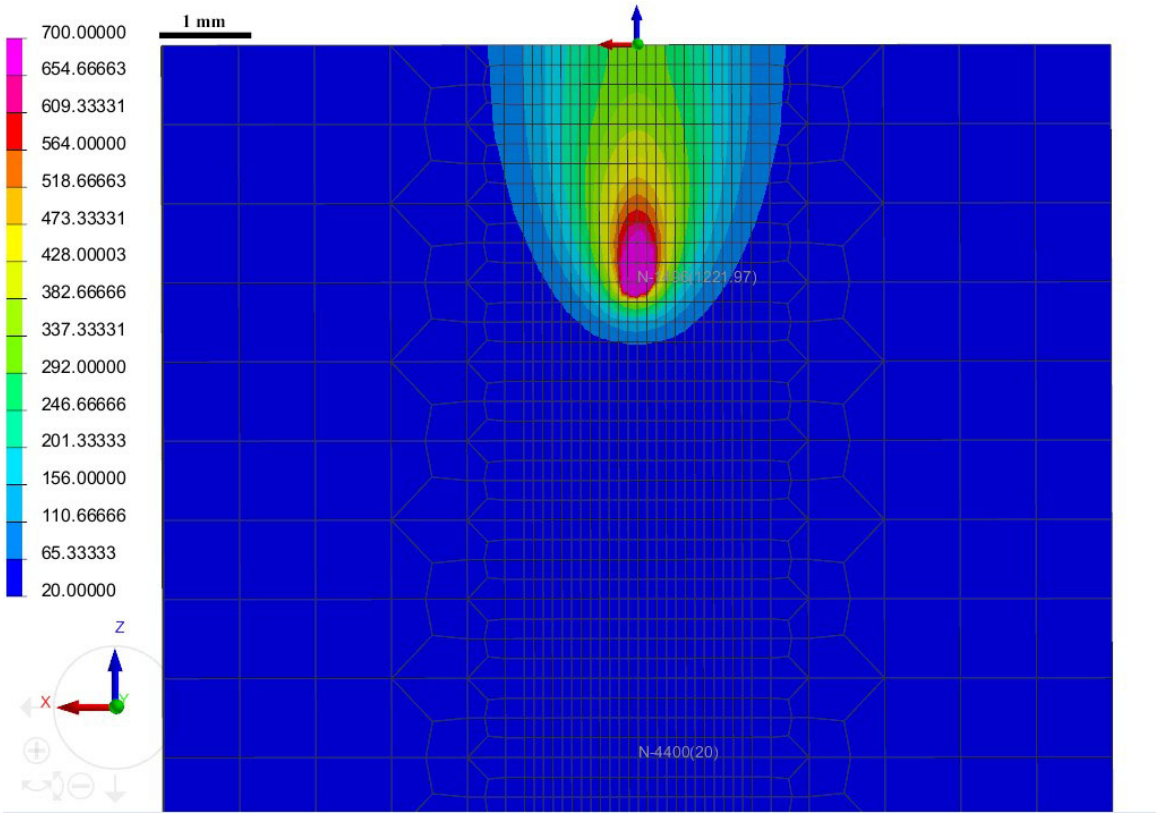

Figure 2.6: The top view display of the temperature profile of the weld pool for a specific case from the FEA model. Additionally, the mesh utilized in the FEA model is visible in the image.

Parameter	Symbol	Units	Value
Melting Temperature	TP	K	933.47
Density	DL	kg/m^3	2700
Heat of Fusion		J/kg	360,000
Specific Heat	SH	$J/(kg \cdot K)$	903
Latent Heat of freezing	LF	J/kg	396,000
Thermal Conductivity	TC	$(W/m \cdot K)$	237
Emissivity	$emmissivity$	W/m^3	0.8
Shrinkage Pressure	PS	Atm	101325
Maximum pore nucleation saturation	${S_H}^{max}$	$mL/100gAl$	2.3
Minimum pore nucleation saturation	${S_H}^{min}$	$mL/100gAl$	1.6
Critical saturation criterion	${S_H}^{N}$		1.7
Partial coefficient of hydrogen	k_H		0.069

Table 2.1: The properties of pure aluminum utilized in the simulations at standard room temperature.

code initially developed to simulate grain structure [40] and gas porosity growth [14] in aluminum casting. Adaptions were made to the casting code to suit applications in additive manufacturing and laser welding processes.

The model encompasses a 3D domain divided into discrete 3D cells, each containing local temperature data, and phase status [41]. The state of each cell is determined by that of its 6 nearest neighbors, with possible states including solid, gas, liquid, or a combination thereof [38]. At the global level, the model adheres to thermodynamic principles, diffusivity, melt temperature, solidus temperature, and initial concentrations. These global behaviors are encapsulated in the following equations.

Porosity initiates at random sites of a predetermined size once the atomic hydrogen concentration surpasses the hydrogen solubility limit [41]. Additionally, gas porosity can nucleate on oxide films [14]. The alteration in porosity density is determined by the subsequent equation [14].

$$\frac{dn_{\mathrm{H}}}{dV} = \begin{cases} \frac{{N_{\mathrm{H}}}^{\max}}{{S_{\mathrm{H}}}^{\max} - {S_{\mathrm{H}}}^{\min}}; (\frac{{C_{\mathrm{H}}}^{\mathrm{L}}}{{S_{\mathrm{H}}}^{\mathrm{L}}} > {S_{\mathrm{H}}}^{\mathrm{N}})(\frac{{C_{\mathrm{H}}}^{\mathrm{L}}}{{S_{\mathrm{H}}}^{\mathrm{L}}} \leq {S_{\mathrm{H}}}^{\mathrm{N}}) \\ 0 \end{cases} \tag{2.1}$$

The equation is structured as follows, where ${N_H}^{max}$ represents the maximum pore nucleation density, ${S_H}^{max}$ denotes the maximum pore nucleation saturation, and ${S_H}^{min}$ signifies the minimum pore nucleation saturation. Local parameters include ${C_H}^L$ for the local hydrogen concentration and ${S_H}^L$ for the local hydrogen saturation, while ${S_H}^N$ indicates the critical saturation criterion for porosity nucleation. The hydrogen saturation within the liquid is determined using an equation derived from Sievert's Law [14].

$${S_{\mathrm{H}}}^{\mathrm{L}} = \sqrt{\frac{P_{\mathrm{G}}}{P_0}} 10(-\frac{2760}{T} + 2.796) \tag{2.2}$$

The parameter P_0 represents the standard atmospheric pressure [41]. The internal pressure of a gas pore, denoted as P_G, is determined by the subsequent equation.

$$P_{\mathrm{G}} = P_0 + \frac{2\gamma}{r_{\mathrm{p}}} \tag{2.3}$$

In this equation, γ represents the surface tension at the gas/liquid interface, and r_p signifies the radius of the pore. This formula is utilized to ascertain whether the pore enlarges or remains unchanged owing to the capillary pressure.

The diffusion of hydrogen is governed by the ensuing equation. Hydrogen near the porosity will be absorbed, prompting further hydrogen diffusion into the surrounding melt.

$$\frac{\partial {C_{\mathrm{H}}}^{\mathrm{E}}}{\partial t} = \nabla \bullet ({D_{\mathrm{H}}}^{\mathrm{E}} \nabla {C_{\mathrm{H}}}^{\mathrm{E}}) + {C_{\mathrm{H}}}^{\mathrm{E}}(1 - k_{\mathrm{H}})\frac{\partial f_{\mathrm{s}}}{\partial t} - (1 - f_{\mathrm{s}} - f_{\mathrm{G}}) \tag{2.4}$$

The parameter k_H represents the partition coefficient of hydrogen [41]. The fraction of gas at the gas/liquid interface is determined by

$${f^{t+\Delta t}}_{\mathrm{G}}(i,j,k) = {f_{\mathrm{G}}}^{\mathrm{t}}(i,j,k) + \Delta f_{\mathrm{G}}(i,j,k) \tag{2.5}$$

Where

$$\Delta f_{\mathrm{G}}(i,j,k) = \frac{\Delta V(i,j,k)}{V_{\mathrm{cell}}} \tag{2.6}$$

2.3.3 CA Model Description

Table 2.1 presents the properties of pure aluminum utilized within the code. A minimum initial hydrogen concentration of 0.69 mL/100g Al was employed, as this

level is deemed necessary for porosity formation [96]. The initial hydrogen concentration remains uniform throughout the model. Given the brief duration of the laser welding process, typically lasting less than a second, hydrogen is unable to escape the domain. Therefore, in the current model, no hydrogen from the atmosphere was permitted to enter the domain.

The domain size of the CA code is 1.4 mm x 2.1 mm x 0.4 mm, with a mesh size of 7.5 µm. Fluid flow is not accounted for in the code initially to simplify the model, owing to the absence of a fluid flow, the code is not capable of accurately simulating the melt flow and porosity escape from the weld pool during welding.

Furthermore, the influence of interface air during welding is solely considered as a source of hydrogen, reacting with molten aluminum. However, air entrapment, which can be minimized through welding process control, is not addressed in the model. The simulation continued until the temperature of the domain fell below the melting point of pure aluminum.

2.4 Simulation Results and Discussion

2.4.1 CA Results

Effect of Initial Hydrogen Concentration and Maximum Pore Nucleation Density

The impact of varying the initial hydrogen concentration and the maximum pore nucleation density on the quantity and dimensions of pores was investigated using a 3D CA model. These simulations were conducted with a laser speed of 300 mm/s and laser power of 668 W.

Figure 2.7 illustrates the evolution of hydrogen concentration during solidification for the model with an initial hydrogen concentration of 1 mL/100g Al and a maximum

pore nucleation density of 2E9 $m^{-}3$. At 0.0139 seconds since the start of welding, as shown in Figure 2.7(a), hydrogen is predominantly concentrated in the liquid phase. Subsequently, at 0.0197 seconds from the start of welding Figure 2.7(b), pores begin to form, represented by red spheres, with localized decreases observed in the initial hydrogen concentration upon pore formation. As welding progress, at 0.0278 since the start Figure 2.7(c), nearing the end of the process, porosity within the weld becomes more pronounced. Similar to the earlier stage, the formation of porosity results in a decrease in the localized hydrogen concentration. Finally, at the conclusion of welding, 0.0579 seconds after initiation Figure 2.7(d), complete solidification occurs, with porosity present in the weld and minimal hydrogen remaining in the solid metal.

The nucleation of porosity occurs when the hydrogen concentration in the liquid reaches its saturation point, after which porosity absorbs more hydrogen from the surrounding melt, leading to a reduction in local concentration. Consequently, additional hydrogen diffuses towards the porosity, facilitating further growth.

Figure 2.8 illustrates the grain structures observed in the computational analysis. Figures (a) and (b) depict the initial and final grain structures respectively, obtained from the CA model with an initial hydrogen concentration of 1 mL/100g Al and a maximum pore nucleation density of 2E9 $m^{-}3$. In Figure 2.8(c), the weld zone of two bare tabs joined together is displayed. For visual clarity, the sample underwent etching to reveal the grains. The welding process was executed using a laser power of 922 W and a speed of 400 mm/s. In Figure 2.8(a), the grain structure prior to welding displays elongation along the rolling direction of the tabs. The initial grain structure is consistent with the grain structure seen away from the weld zone in Figure 2.8(c), corroborating the model's accuracy. The final grain structure depicted

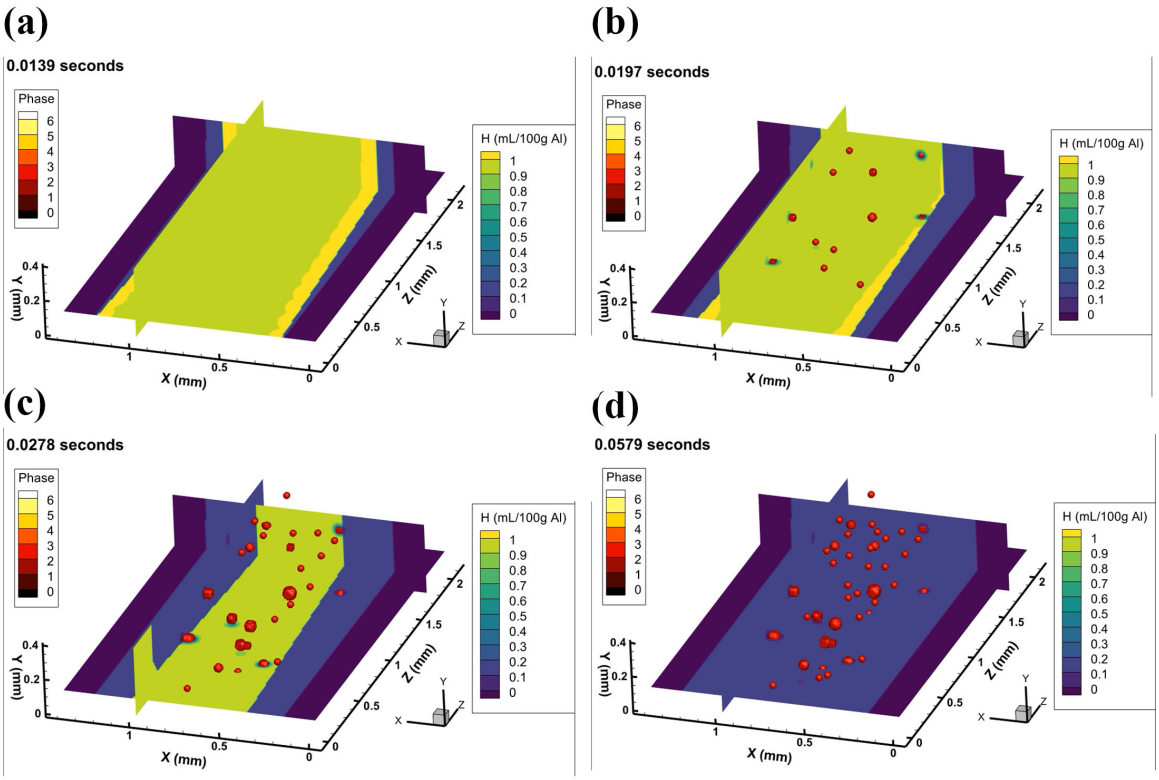

Figure 2.7: The evolution of hydrogen concentration over time for the model featuring an initial hydrogen concentration of 1 mL/100g Al and 2E-9 $m^{-}3$ maximum pore nucleation density.

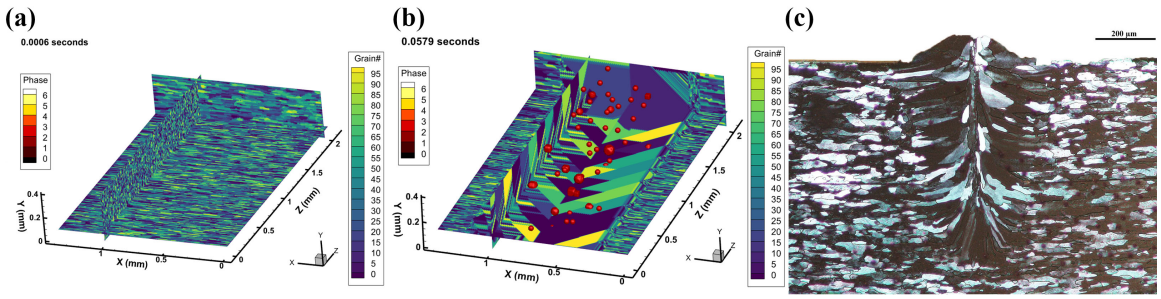

Figure 2.8: Figures (a) and (b) display the initial and final grain structures post-welding respectively, for the model featuring an initial hydrogen concentration of 1 mL/100g Al and a maximum pore nucleation density of 2E-9 $m^{-}3$. Figure (c) shows the etched grain structure of the weld zone following welding. The weld was performed on two bare tabs using a laser power of 922 W and a laser speed of 400 mm/s.

in Figure 2.8(b) demonstrates the regrowth of grains along the temperature gradient induced by the laser, accompanied by the presence of pores within the laser's path. This outcome aligns with the observed grain structure shown in Figure 2.8(c).

Figure 2.9 showcases the final grain structure for the models featuring different initial hydrogen concentrations: (a) 0.69 mL/100g Al and (b) 1 mL/100g Al. All models shared a maximum pore nucleation density of 2E9 $m^{-}3$. Table 2.2 provides insight into the total number of pores in these models, with Figure 2.9(a) exhibiting 56 pores, and Figure 2.9(b) showing 59 pores. Notably, the figures highlight that the size of porosity increases with increasing initial hydrogen concentration. Elevated hydrogen concentration in the liquid phase facilitates enhanced hydrogen diffusion and pore growth. Moreover, the heightened hydrogen content in the liquid phase leads to increased porosity nucleation due to more liquid attaining hydrogen saturation. The absorption of more hydrogen during sample preparation or laser heating contributes to the formation of larger and more numerous pores. Hydrogen can originate

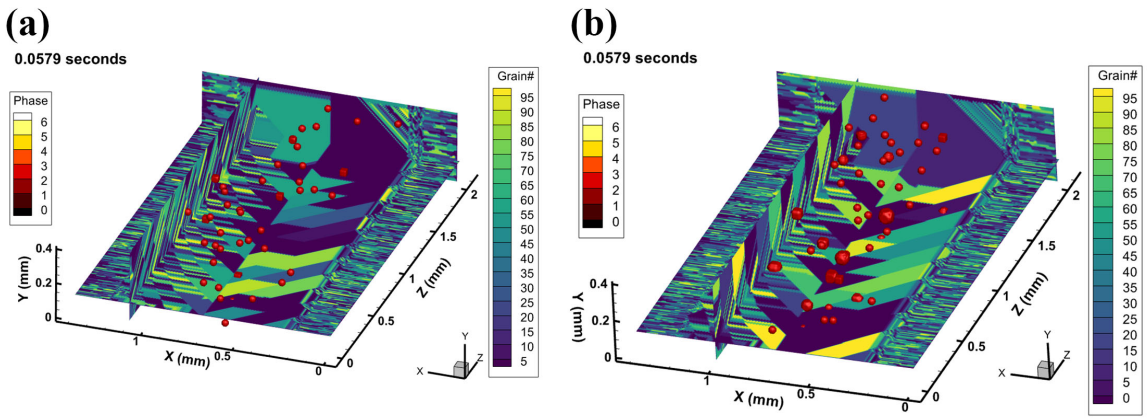

Figure 2.9: The ultimate microstructure of two models featuring a maximum pore nucleation density of 2E9 m^-3 and initial hydrogen concentration of (a) 0.69 mL/100g Al and (b) 1 mL/100g Al.

from ambient air or, in welding scenarios, from the anodized aluminum, wherein the breaking up of the oxide releases additional hydrogen. Consequently, anodized welds typically exhibit larger and more abundant porosities compared to bare aluminum welds.

Figure 2.10 depicts the final grain structure alongside the porosity for models executed with (a) 2E7 m^-3 and (b) 2E9 m^-3 maximum pore nucleation density, both featuring an initial hydrogen concentration of 1 mL/100g Al. Table 2.2 presents the final number of pores post-solidification. The reduction in maximum pore nucleation density correlates with a decrease in the number of pores, attributed to the diminished availability of potential nucleation sites. The maximum pore nucleation density directly influences the capacity for pore nucleation; for instance, the presence of oxide fragments within the weld melt pool can offer additional heterogeneous nucleation sites.

Hydrogen Concentration (mL/100g Al)	Pore Nucleation Density (m^-3)	Total Number of Pores
1	2E7	0
0.69	2E9	56
1	2E9	59

Table 2.2: The results from the CA simulations, exploring the effects of different initial hydrogen concentrations and maximum pore nucleation densities.

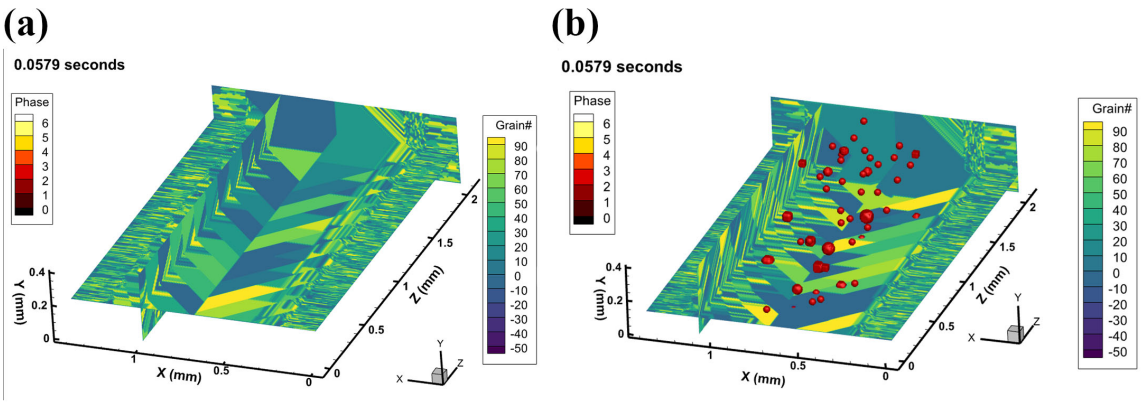

Figure 2.10: The concluding grain structure of two models featuring am initial hydrogen concentration of 1 mL/100g Al and maximum pore nucleation densities of (a) 2E7 m^-3 and (b) 2E9 m^-3.

Effect of Laser Speed and Power

The influence of altering the laser speed and laser power on the predicted porosity by CA was investigated. All the models were conducted with an initial hydrogen concentration of 1 mL/100g Al and a maximum pore nucleation density of 2E9 $m^{-}3$. Table 2.3 outlines the total pores count at the simulation's conclusion.

When the laser speed increases, both the energy density and the width of the melt pool decrease. Consequently, there is a reduction in the weld pool's size and the duration it remains molten. This results in a decreased presence of hydrogen within the melt pool, consequently lowering the porosity in the final weld. Figure 2.11 presents the final microstructure images for models employing varying laser speeds: (a) 300 mm/s, (b) 400 mm/s, (c) 500 mm/s, and (d) 600 mm/s.

Furthermore, Table 2.3 also demonstrates the impact of laser power on the porosity. Increasing the laser power augments the energy density and extends the duration of molten stage for the weld pool. A slower cooling rate of the weld pool allows for increased hydrogen diffusion into the molten aluminum, thereby elevating the hydrogen content and subsequently the porosity. Figure 2.12 illustrates the final grain structure images for models employing varying laser powers: (a) 668 W, (b) 922 W, and (c) 1170 W.

Interestingly, in Figure 2.12, there is an unexpected decrease in the size of porosity with increasing laser power. This contrary trend may suggest an underestimation in the CA model's representation of the effect of solidification time alterations on porosity. Further investigation into this phenomenon is warranted for future research endeavors. When importing the temperature profile into CA, a cutoff temperature was used to correct for some overestimation of temperature in the FEA model. This

Laser Speed (mm/s)	Laser Power (W)	Total Number of Pores
300	669	59
400	668	32
500	668	23
600	668	9
300	922	113
300	1170	169

Table 2.3: The results from the CA simulations examining the effects of changing laser speed and power.

cutoff temperature could lead to the discrepancy in the effect of laser power, as the higher temperature with higher laser power could have a larger effect on the size of porosity. As seen in Figure 1.1 the solubility of hydrogen in aluminum increases with increasing melt temperature. The increase in hydrogen concentration in the melt would then cause an increase in the size of porosity. The use of a cutoff temperature should be further investigated in future work.

2.5 Experimental Results

2.5.1 Micro-CT Results

Figure 2.13 presents the 3D results obtained from micro-CT scanning of two welds, covering a total weld length of 20 mm. Figure 2.13(a) and (b) depict the anodized weld sample, welded with a laser power of 668 W and a laser speed of 330 mm/s, while Figure 2.13(c) and (d) represent the bare tabs welded together using a laser power of 668 W and a laser speed of 300 mm/s. The blue spheres in the images represent the detected porosity.

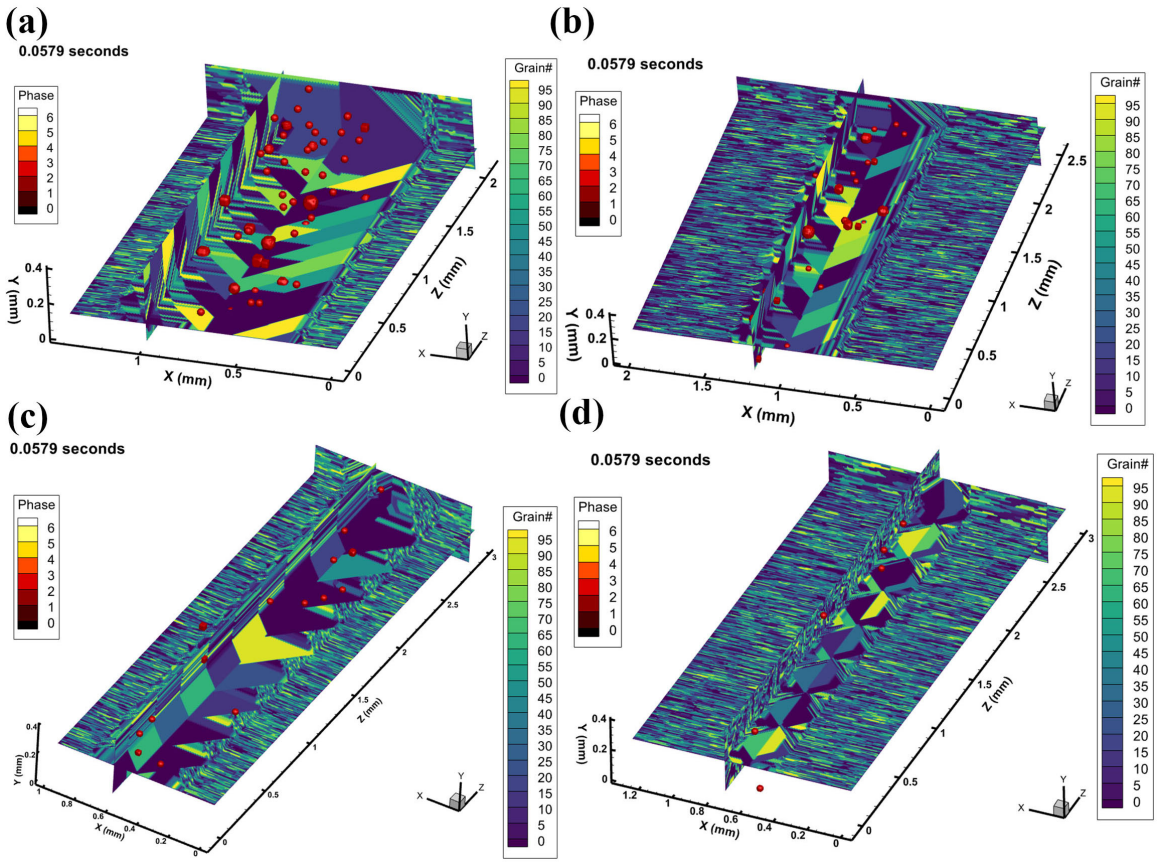

Figure 2.11: The final grain structure outcomes from laser welding with a laser power of 668 W and laser speeds of (a) 300 mm/s, (b) 400 mm/s, (c) 500 mm/s, and (d) 600 mm/s.

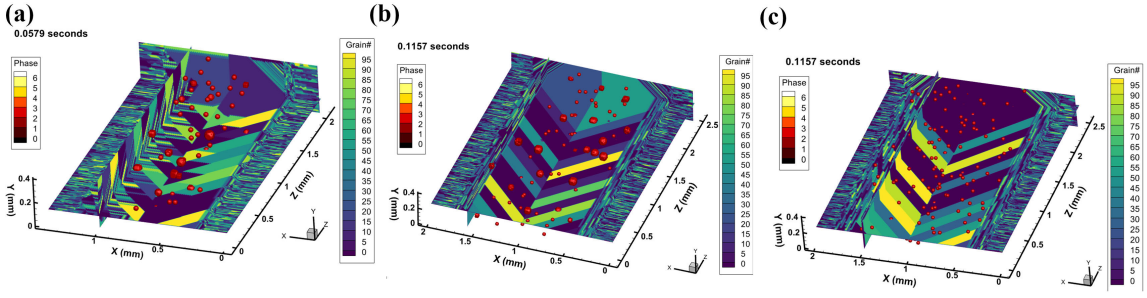

Figure 2.12: The final microstructure results from laser welding with a laser speed of 300 mm/s and laser powers of (a) 668 W, (b) 922 W, and (c) 1170 W.

Sample	Laser Speed (mm/s)	Largest Pore Volume (mm^3)	Largest Pore Diameter (mm)	Total Number of Pores
Anodized	330	1.94E-3	0.155	11,558
Bare	300	1.07E-4	0.059	89

Table 2.4: The micro-CT findings of both the anodized and bare welds, conducted with a laser power of 668 W.

These results reveal a notable disparity in porosity between the anodized and bare welds, with the former exhibiting a higher porosity level. The majority of this porosity is attributed to hydrogen, the welds' shallow depth precludes keyhole collapse and keyhole-induced porosity [99]. Table 2.4 depicts the total number of pores, revealing 11,558 pores in the anodized weld compared to 89 pores in the bare weld. This substantial difference quantifies the contrast between the anodized and bare welds.

It's worth noting that the total number of pores detected by micro-CT exceeds the predictions of the CA model, indicating the presence of pores originating from sources other than hydrogen. Additionally, Table 2.4 presents the largest pore volume and diameter identified by micro-CT. The anodized weld exhibits significantly larger porosity compared to the bare weld, suggesting higher hydrogen content and more nucleation sites during solidification. This finding aligns with the trends observed in the CA results, where increasing hydrogen concentration led to larger pores, as seen in Figures 2.9 and 2.10.

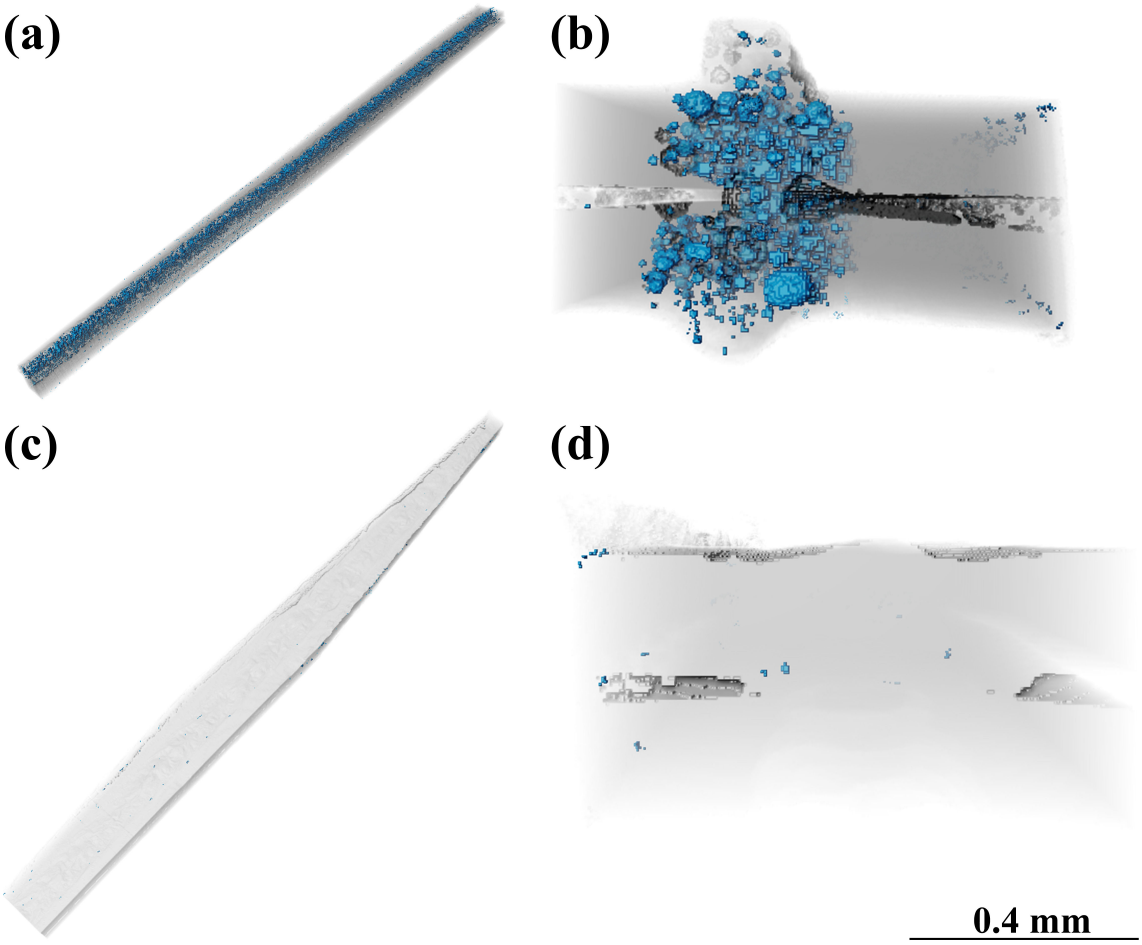

Figure 2.13: The 3D results obtained from the micro-CT scan depict the following: (a) and (b) represent the welding of two anodized Al tabs using a laser power of 668 W and a laser speed of 330 mm/s. (c) and (d) showcase the welding of two bare tabs with a laser power of 668 W and a laser speed of 300 mm/s. In these images, the blue spheres denote porosity.

Effect of Laser Power and Speed

To explore the impact of laser power and speed on porosity within the weld pool, two additional welded samples were subjected to micro-CT scanning. Figure 2.14 displays the 3D result of three anodized welds examined via micro-CT. Figure 2.14(a) and (b) represent a weld conducted with a laser power of 668 W and a laser speed of 330 mm/s. Figure 2.14(c) and (d) depict a weld executed with a laser power of 1170 W and a laser speed of 300 mm/s. Figure 2.14(e) and (f) showcase a weld performed with a laser power of 1170 W and a laser speed of 600 mm/s.

Table 2.5 enumerates the largest pore volume and diameter detected in the micro-CT results when altering the laser speed and power. An increase in laser power from 668 W to 1170 W correlates with an increase in the diameter of the largest pore, from 0.155 to 0.233 mm. Additionally, the number of pores escalates from 11,558 to 44,640 with the rise in laser power. The augmentation in molten aluminum volume and temperature, resulting from higher laser power, enhances the likelihood of hydrogen diffusion into the weld pool, as depicted in Figure 1.1. This increased hydrogen content in the liquid phase can lead to larger pores due to heightened hydrogen availability, facilitating pore enlargement.

Conversely, an elevation in laser speed from 300 mm/s to 600 mm/s correlates with a decrease in the number of pores from 44,640 to 18,253. This reduction is attributed to the reduction in the size of the melt pool associated with a faster laser speed. This trend aligns with the findings from the CA simulations, as shown in Table 2.3 and Figures 2.11 and 2.12. However, in the CA results, pore size decreased with the increase in laser power. This discrepancy could be attributed to the presence of other

Laser Power (W)	Laser Speed (mm/s)	Largest Pore Volume (mm^3)	Largest Pore Diameter (mm)	Total Number of Pores
668	330	1.94E-3	0.155	11,558
1170	300	6.63E-3	0.233	44,640
1170	600	1.81E-2	0.326	18,253

Table 2.5: The micro-CT findings of anodized welds, subjected to variations in laser speed and power.

pore types, such as shrinkage pores, which are not accounted for in the current CA model but are observed in the weld.

2.5.2 Microstructure Results

Figure 2.15(a) displays an SEM image capturing the weld zone of two bare Al tabs joined together. Notably, no visible porosity is observed within the weld area; however, the presence of weld crack tips is noted as the primary defects. Conversely, in Figure 2.15(b), an SEM image showcases two anodized Al tabs welded together, distinctly revealing the presence of porosity within the weld. It's worth mentioning that both welds depicted in Figure 2.15 were welded utilizing a laser power of 668 W and a laser speed of 300 mm/s.

Moving on to Figure 2.16, (a) depicts an SEM image illustrating the weld zone where a bare tab is welded onto an anodized tab, while Figure 2.16(b) showcases an SEM image portraying an anodized tab welded onto a bare tab. Similar laser parameters of 668 W power and 300 mm/s speed were employed for both welds in Figure 2.16. Notably, in Figure 2.16(a), the majority of porosity is concentrated

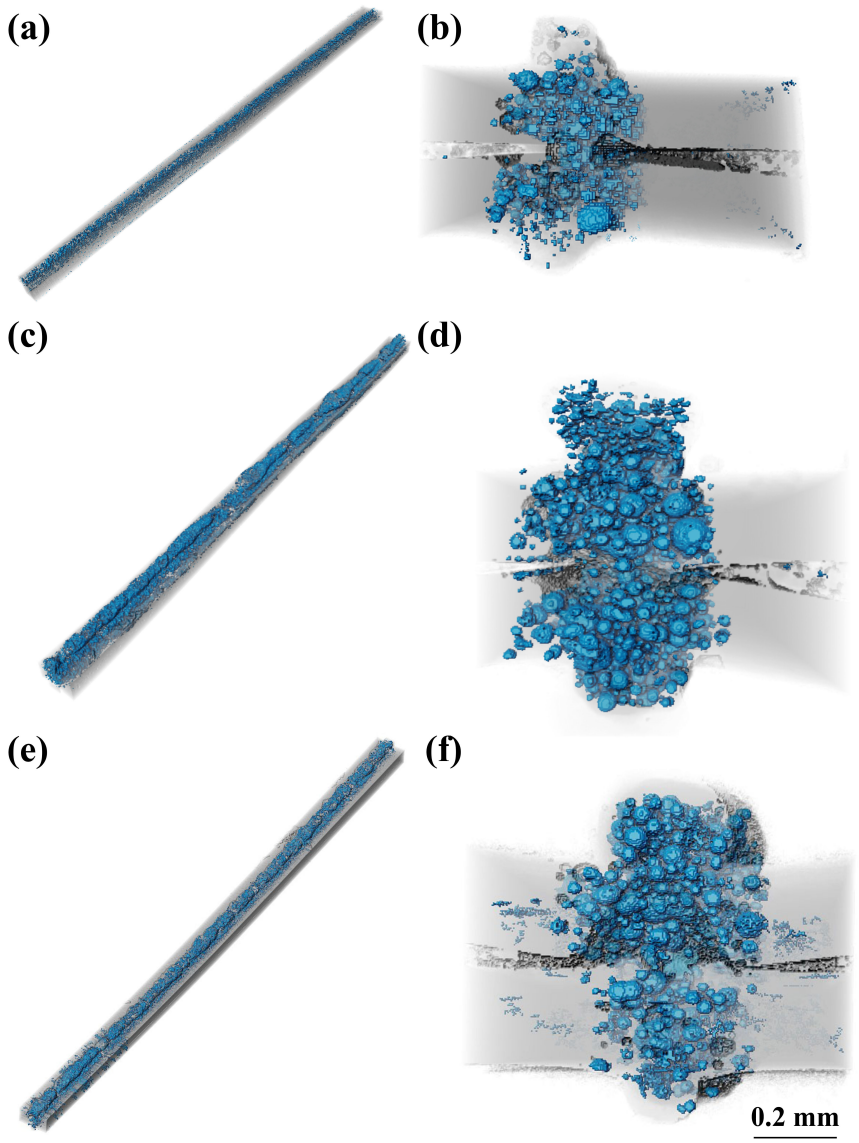

Figure 2.14: The 3D results from the micro-CT scan depict three anodized welds under the following laser welding parameters: (a) and (b) a laser power of 668 W with a laser speed of 330 mm/s. (c) and (d) a laser power of 1170 W and a laser speed of 300 mm/s. (e) and (f) a laser power of 1170 W with a laser speed of 600 mm/s. In these images, the blue spheres represent the porosity.

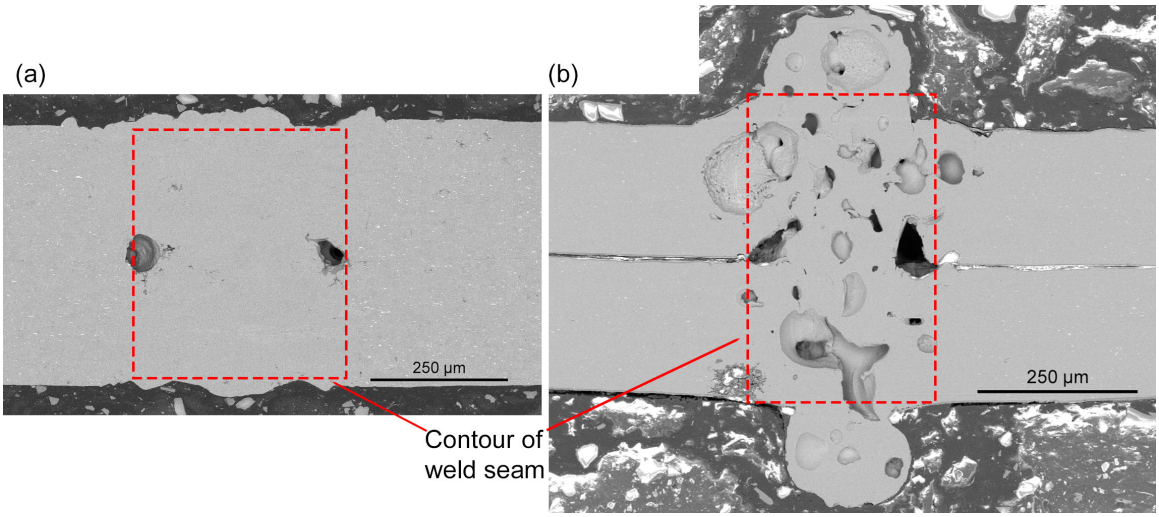

Figure 2.15: The SEM images depict the weld zone of (a) two bare tabs and (b) two anodized tabs welded together, utilizing a laser power of 668 W and a speed of 300 mm/s. The red box outlines the weld seam's contour.

within the bottom tab. This phenomenon is attributed to the reduction in the number of aluminum oxide layer 4 to two layers when dissimilar tabs are welded together. Consequently, a decrease in aluminum oxide within the weld zone leads to a reduction in heterogeneous nucleation sites for hydrogen porosity. The red box encircling the contour of the weld seam is present in both Figure 2.15 and 2.16.

Figure 2.17 illustrates a segment of the anodized layer. In Figure 2.17(a), an SEM image displays the weld zone of two anodized tabs welded together using a laser power of 668 W and a speed of 300 mm/s. Figure 2.17(b) offers a magnified view of the boxed area in (a), focusing on the anodized layer adjacent to the weld. Figure 2.17(c)-(e) presents an EDS map of the region within the rectangle in (b). Figure 2.17(c) depicts a carbon map revealing the carbon mount. Figure 2.17(d) portrays an oxygen map, distinctly delineating the approximately 2.5 µm thick anodized layer. Figure 2.17(e)

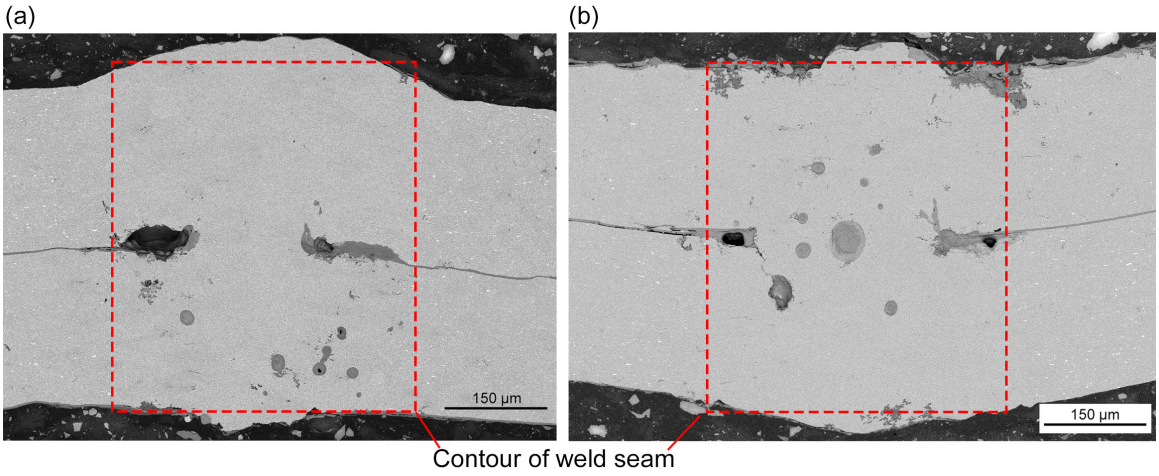

Figure 2.16: The SEM image showcases the weld zone of (a) a bare tab welded to an anodized tab and (b) an anodized tab welded to a bare tab, employing a laser power of 668 W and a speed of 300 mm/s. The red box delineates the contour of the weld seam.

showcases an aluminum EDS map highlighting both the aluminum of the weld and the lighter aluminum on the anodized layer. Notably, the layer within the weld pool is fragmented, with these oxide fragments mixing into the molten metal, thereby providing heterogeneous nucleation sites for hydrogen porosity.

Figure 2.18 presents an SEM image depicting a pore alongside oxide fragments adjacent to it, as observed in Figure 2.18(b) through EDS identification. Figure 2.18(a) provides a comprehensive view of the entire weld resulting from the welding of two anodized tabs, achieved with a laser power of 668 W and laser speed of 300 mm/s. In Figure 2.18(b), a magnified section reveals a pore with a labeled oxide piece. It's widely acknowledged that oxide can chemically bond with hydrogen, thereby introducing more hydrogen into the molten pool. This excess hydrogen can lead to

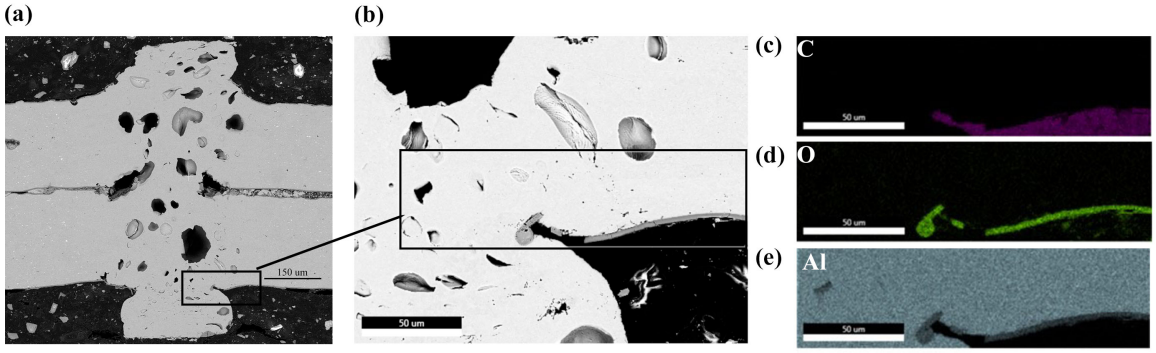

Figure 2.17: (a) The SEM image displays the weld joint of two anodized tabs, welded together using a laser power of 668 W and a speed of 300 mm/s. (b) This segment highlights the anodized layer in proximity to the weld. (c) An EDS map depicts the distribution of carbon at the specified location. (d) The EDS map showcases the distribution of oxygen, emphasizing the presence of the anodized layer. (e) An EDS map illustrates the distribution of aluminum within the examined area.

increased supersaturation within the molten metal, consequently promoting nucleation of porosity. The oxide can also function as heterogeneous nucleation sites for hydrogen pores.

Figure 2.19(a) illustrates the weld zone of two anodized tabs welded together using a laser power of 668 W and a speed of 300 mm/s, while Figure 2.19(b) zooms in on a pore within the weld zone, surrounded by oxide. This pore is linked to the crack tip by a line of oxide. Both Figures 2.18 and 2.19 exhibit irregular and rounded porosity. While the rounded porosity typically denotes hydrogen porosity, the irregular porosity may also result from hydrogen pores merging or being affected by growing grains.

Moving to Figure 2.20, (a) displays the weld between an anodized tab and a bare tab, utilizing a laser power of 668 W and a laser speed of 300 mm/s. In Figure 2.20(b), a pore within the weld zone is encircled by oxide. Notably, Figure 2.20(a) showcases

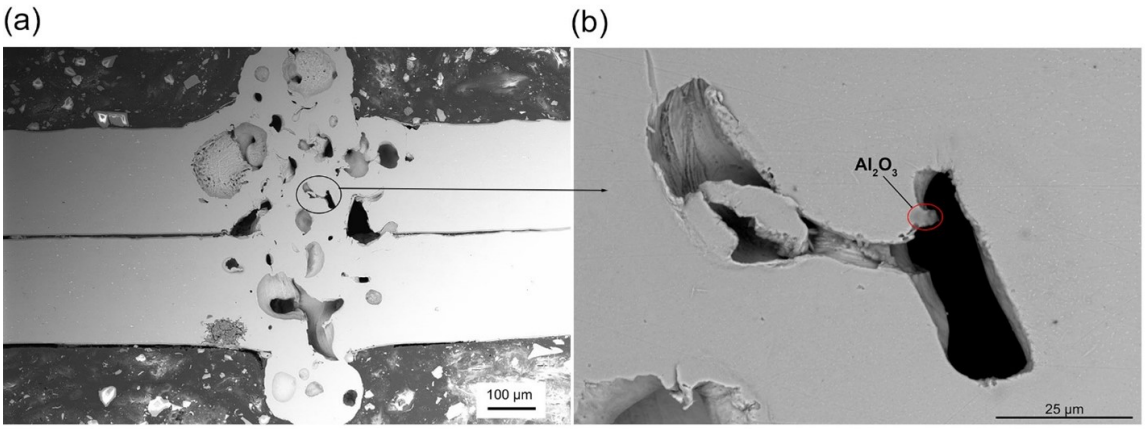

Figure 2.18: (a) The SEM image of a weld zone from two anodized tabs welded together with a laser power of 668 W and a laser speed of 300 mm/s. (b) A pore with oxide attached to the pore.

round porosity, characteristic of hydrogen porosity. In the upper left portion of Figure 2.20(b), a line of oxide descends from the anodized layer, akin to Figure 2.19(b). This line of oxide terminates at the pore, indicating that oxide fragments disrupted during welding can serve as heterogeneous nucleation sites for porosity.

2.5.3 LECO Results

To quantitatively assess the impact of hydrogen on porosity formation, the LECO results are presented in Table 2.6. These results pertain to the the hydrogen content in both bare and anodized materials before welding, revealing a significantly higher concentration of hydrogen in the anodized material.

Table 2.7 displays the LECO results for hydrogen in the welded samples. Notably, the bare welded samples exhibit the lowest hydrogen content, while the anodized samples exhibit the highest. Samples tested after removing the anodized layer show a reduction in hydrogen content, indicating that the anodized layer has absorbed

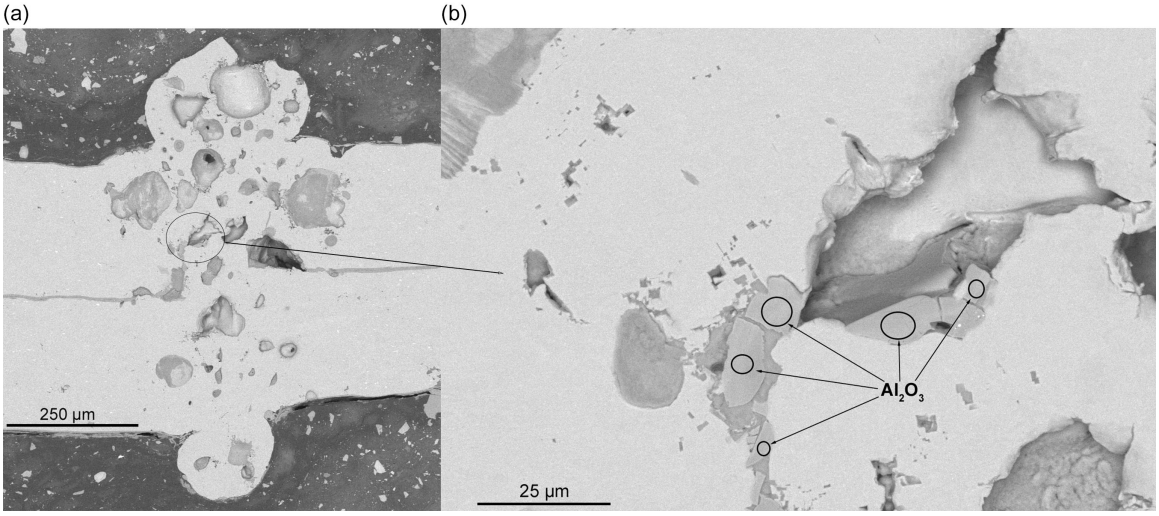

Figure 2.19: (a) This SEM image portrays the weld zone resulting from the welding of two anodized tabs, achieved with a laser power of 668 W and a speed of 300 mm/s. (b) Presented here is a pore extracted from the aforementioned weld zone, encircled by oxide.

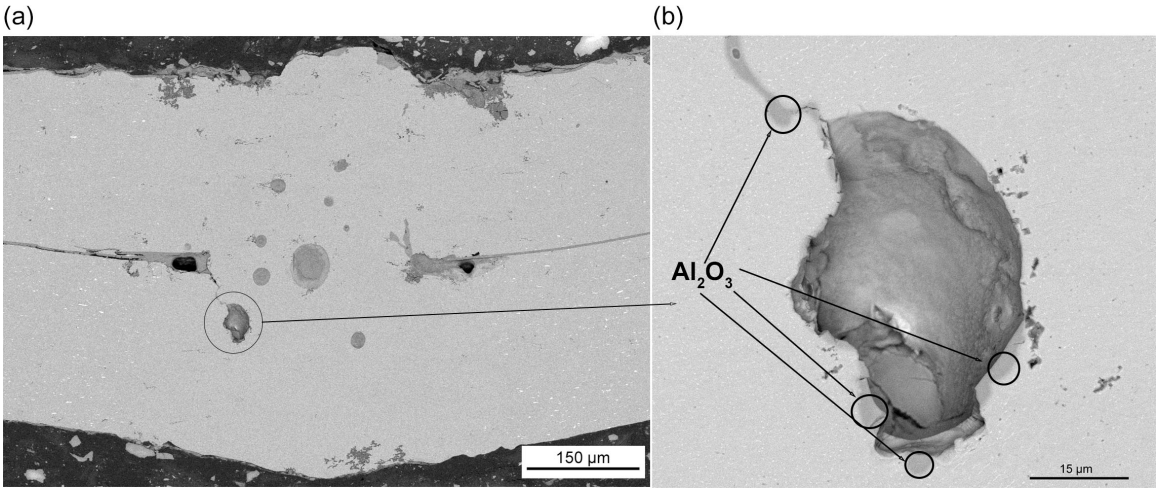

Figure 2.20: (a) This SEM image depicts the weld zone resulting from the welding of an anodized tab with a bare tab, utilizing a laser power of 668 W and a laser speed of 300 mm/s. (b) Depicted here is a pore encircled by oxide within the described weld zone.

Sample	Ground or Not Ground	Hydrogen Concentration (ppm)
Bare	Ground	0.12 0.11
Anodized	Ground	0.39 0.38
Anodized	Not Ground	0.46 0.46

Table 2.6: The LECO results for the as-received base material.

hydrogen. This observation aligns with prior research indicating that the oxide layer can absorb moisture [15], which subsequently heats up during laser welding, releasing hydrogen into the molten aluminum.

During laser welding, upon the laser's impact on the oxide layer, the layer will fracture and fragments will be propelled into the molten aluminum. Moreover, this fracturing of the oxide layer results in the release of entrapped hydrogen into the molten metal, consequently elevating the hydrogen concentration in the melt [12].

2.5.4 Moisture Test

Figure 2.21 depicts optical images of the welds from the preheating and moisture test results. Both samples are two anodized tabs welded together using a 668 W laser power and a speed of 120 mm/s. Both weld zones are full of porosity and there does not seem to be a reduction of porosity in the preheating sample. Preheating the material prior to welding should remove some moisture not bonded with the oxide. However, from this result it does not seem like water on the surface effects the porosity. Similarly, the sample with water added to it does have more porosity than

Sample	Welding Speed (mm/s)	Ground or Not Ground	Hydrogen Concentration (ppm)
Bare	360	Ground	0.038 0.036
Bare	300	Ground	0.038 0.031
Anodized	330	Ground	0.30 0.32
Anodized	330	Not Ground	0.40 0.41
Anodized	300	Ground	0.30 0.36
Anodized	300	Not Ground	0.36 0.39
Anodized on top	300	Ground	0.18 0.20
Anodized on top	300	Not Ground	0.22 0.22
Anodized on top	360	Ground	0.18 0.18
Anodized on top	360	Not Ground	0.22 0.22

Table 2.7: The LECO results for the welded specimens.

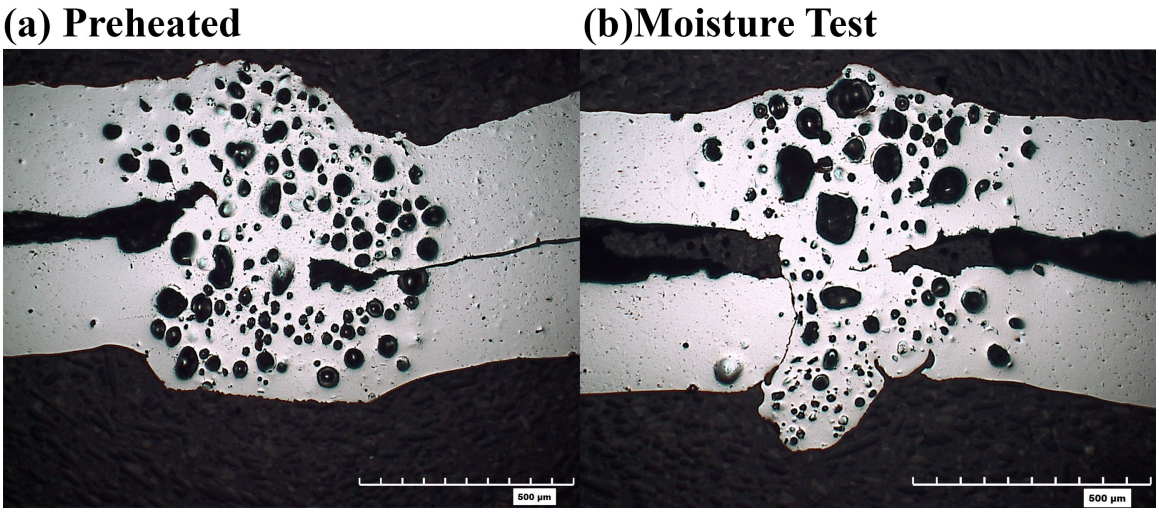

Figure 2.21: The optical images of the welds from the (a) preheating test and (b) the moisture test. Both welds are two anodized tabs joined using a 668 W laser power and a speed of 120 mm/s.

the preheating sample. Allowing the anodized material to absorb more water prior to welding should cause more porosity to form, however this does not seem to occur here. These results were repeated with other samples and they all showed similar results. Therefore, preheating the materials before welding is not an effective method for reducing porosity.

2.5.5 Experimental Tests on Weld Strength

Figure 2.22 presents the lap-shear test results for the four material configurations. The graph depicts the average maximum load against the laser speed. The material configurations tested include anodized material welded together, bare material welded together, anodized material welded to bare material, and bare material welded to anodized material, all welded with a laser power of 668 W.

For laser speeds of 270, 300, and 330 mm/s, the anodized material welded together showed the lowest average maximum loads, 237, 272, and 269 N, respectively. At a speed of 360 mm/s, the bare material welded on top of the anodized tab had the lowest average maximum load of 79 N. This is attributed to under-welding at this speed, causing weld failure at the interface with some material transfer. All other welds also failed at the interface, with the weld bead material transferring to the bottom sheet.

For all assessed laser speeds, welds without anodized material achieved the highest average maximum loads, clearly indicating that welding anodized material reduces the weld's soundness. Comparing these results to Figures 2.13, 2.15, and 2.16, it is likely that porosity in anodized welds causes the decrease in average maximum load. Tables 2.3, and 2.5 further support that higher laser speeds reduce porosity, as evidenced by the increased average maximum load with higher speeds, especially in anodized welds.

2.6 Conclusions

This research developed a cellular automaton model to predict the nucleation and growth of hydrogen porosity during laser welding of commercially pure aluminum tabs, intended for automotive battery applications. Aluminum tabs with a thickness of 0.2 mm, both bare and anodized, were welded under various process parameters. The results indicated that the welds of anodized tabs exhibited significantly more porosity compared to the bare tabs.

(1) The primary cause of weld porosity is hydrogen supersaturation in the aluminum melt pool during welding, which can originate from reactions with water vapor

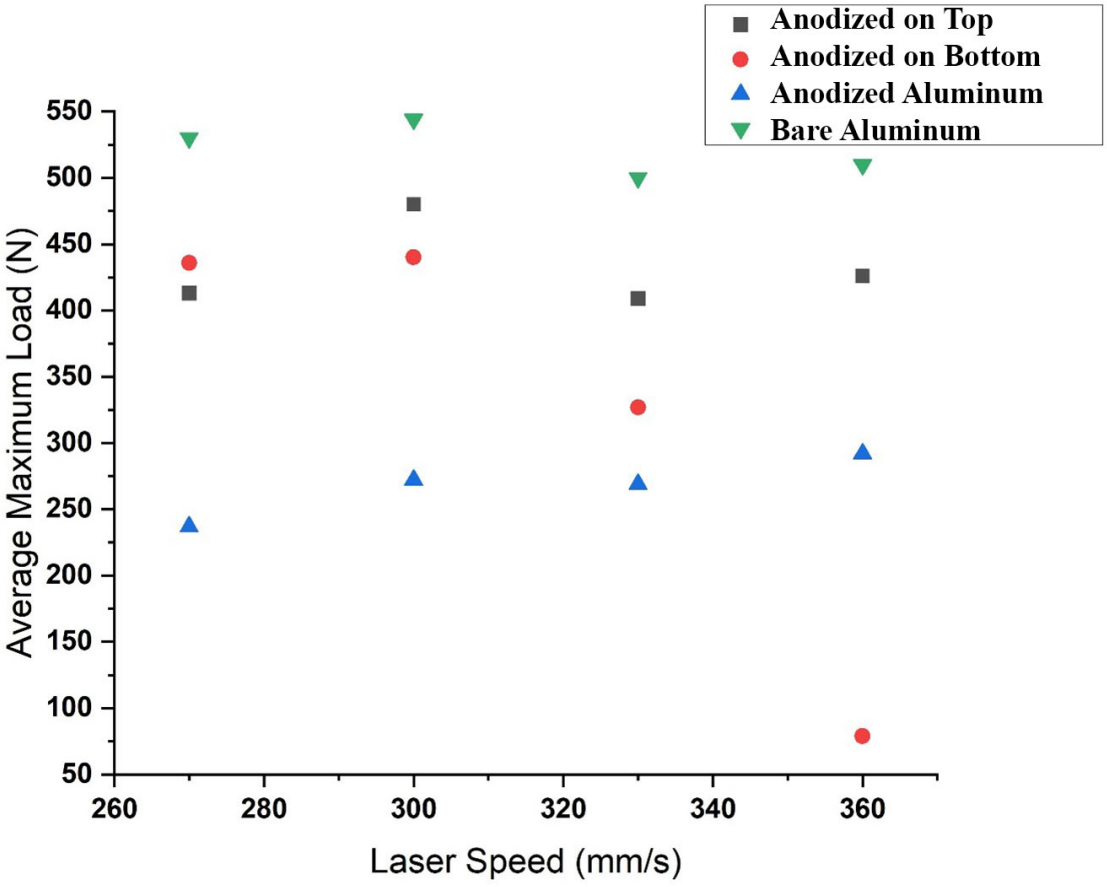

Figure 2.22: The average maximum load at failure for the four configurations, welded with a laser power of 668 W, is plotted against the laser speed.

in the air or from the fragmented oxide layer on anodized aluminum. The hydrogen is rejected during solidification and causes a supersaturation in the liquid.

(2) The presence of anodized aluminum results in heightened porosity in the welds, as the fragmented oxide layer served as heterogeneous nucleation sites for porosity during solidification. The elevated temperature from laser heating caused the breakdown of the oxide layer, and these fragmented pieces were subsequently incorporated into the bulk aluminum within the melt pool.

(3) The outcomes of the CA modeling demonstrate that elevating the initial hydrogen concentration from 0.69 mL/100g Al to 1 mL/100g Al resulted in larger porosity, whereas an augmentation in the maximum pore nucleation density resulted in the formation of more porosity. By increasing the concentration of hydrogen in the liquid, more hydrogen is available to be absorbed into the pores, thus allowing them to grow larger.

(4) The CA model was utilized to examine the impact of laser speed and laser power. A rise in laser speed from 300 mm/s to 600 mm/s resulted in a decrease in porosity, whereas increasing the laser power from 668 W to 1170 W led to an increase in porosity due to the enlarged weld pool size.

(5) The CA model used in this investigation demonstrated a generally satisfactory correspondence with laser welding experiments, particularly concerning the impacts of process parameters on porosity formation. Although the present model does not offer a complete quantitative prediction of all porosity, it serves as a valuable tool for optimizing laser welding process parameters to mitigate or eliminate porosity formation induced by hydrogen in aluminum welding.

Chapter 3: Gas Porosity in Die Casting

This chapter is about gas porosity in die casting parts and how the use of vacuum can reduce and eliminate the porosity. Water analog experiments are compared with MAGMASOFT® and ProCAST flow simulations to validate the location and amount of entrapped air within the die cavity during filling. These results are then compared to aluminum die cast specimens cast under various vacuum conditions.

3.1 Introduction

High-pressure die casting (HPDC) is a manufacturing process that produces thin-walled and near-net shape castings, ideal for automotive and other industrial applications. In the automotive sector, HPDC produces crucial components like shock towers, A or B pillars, subframes, inner door panels, and even large body castings for electric vehicles. These die cast parts boast exceptional mechanical properties, such as yield strength and elongation as noted by [100].

However, defects such as gas porosity have the potential to diminish their mechanical properties [101, 102], weldability, and heat treatability. Gas trapped within the pores can expand when heated, forming blisters that degrade surface quality and renders parts unusable [48]. Gas porosity originates from various sources 1) hydrogen, as discussed Chapter 2; 2) reactions between molten metal and lubricants; and

3) entrapped air due to turbulence during metal filling. While hydrogen porosity can be managed through degassing treatments and reaction byproducts controlled with proper lubricant usage, entrapped air poses a greater challenge due to the high velocities involved in die casting [58, 54, 62].

The integration of vacuum into the die casting process offers a solution to mitigate entrapped air during casting. By evacuating the air in the shot sleeve and die chamber during the metal injection, vacuum minimizes air within the cavity, thereby reducing the likelihood of air entrapment during filling [54, 103]. Numerous studies have explored the impact of varying vacuum levels on entrapped air [54, 104], and gas porosity in castings [51, 105, 106].

Hu et al [52] investigated the influence of vacuum levels on ductility and porosity in AlSi12Fe castings, observing a decrease in the size of larger pores with increasing vacuum strength, measured by decreasing gas pressure. They also noted an increase in sample density with higher vacuum strength, along with improved repeatability of elongation and ultimate tensile strength [52]. Jin and Kang [75] reported fewer blisters formed during heat treatment for aluminum-magnesium samples cast under vacuum.

Furthermore, employing a stronger vacuum termed "super vacuum," with a gas pressure lower than 50 mbar, has shown promise in further reducing gas porosity [58, 57]. Dong et al [57] demonstrated that the use of a super vacuum enhanced the ductility of Al-Si-Mg-Mn die castings. By mitigating entrapped air during casting, vacuum application improves the elongation and strength of casting, making die-cast aluminum suitable for structural components [54, 51, 52, 107, 108].

X-ray computed tomography (CT) serves as a powerful tool for imaging the pores within three-dimensional (3D) domains, offering crucial 3D data for microstructure characterization. Liu et al [109] employed CT to demonstrate that fractures typically occur at locations where pores reach their maximum size, with samples with the smallest pores displaying the highest levels of ductility [109]. Li et al [62] similarly utilized CT to analyze pore characteristics and their correlation with fractures in aluminum die castings. Szalva and Orbulov [110] employed CT to investigate the root causes of failure in fatigue test samples, revealing that the samples cast without vacuum often failed due to gas porosity.

Micro-CT provides even finer resolution for imaging porosity, as exemplified in Chapter 2. Gu et al [38] highlighted the crucial influence of cooling rate on determining secondary dendrite arm spacing and the 3D porosity morphology, including parameters like porosity percentage, pore volume, and pore count. Zhang et al [111] noted a direct correlation between the elongation of the samples and the size of the pores observed on the fracture surfaces.

CT and micro-CT techniques are also instrumental in assessing the sphericity of porosity to differentiate between shrinkage-induced and gas pores [38, 111]. Sphericity, defined as the ratio of the spherical surface area to the measured surface area of the pore [62]. However, while these techniques excel in characterizing porosity in final cast components, they do not offer direct insights into the formation of porosity during cavity fill and the casting process itself.

While HPDC trials can shed light on the impact of vacuum on final casting quality, comprehending how vacuum influences molten metal flow within the die and shot system necessitates other approaches. Simulation tools like MAGMASOFT®

(a casting simulation package by MAGMA Gießereitechnologie GmbH, Aachen, Germany), ProCAST, a finite element based casting simulation, and others have been instrumental in visualizing melt flow during HPDC and identifying optimal process conditions [112]. However, directly validating these simulations poses challenges.

Jin and Kang [75] employed computer simulations to model vacuum die casting processes, finding agreement between their simulations and die casting specimens, paticularly in the reduction of porosity with the application of vacuum. Similarly, Gunasegaram et al [77] utilized computer modeling to investigate the solidification behavior of molten aluminum and the impact of the melt velocity on the mechanical properties of aluminum castings. Their findings align with those of Jin and Kang [75], demonstrating that porosity reduction enhances the mechanical properties of castings [77].

Water analog experiments serve as a valuable tool for modeling liquid flow within a die during the casting process [84]. This method involves using water as the casting fluid, which is injected into a die cavity at speeds akin to those in actual die casting processes. A transparent plastic plate acts as the cover die, facilitating the use of a high-speed camera to capture flow dynamics within the cavity and shot system. Since water shares a similar kinematic viscosity with molten aluminum, water analog experiments allow for meaningful comparison with casting trials [80].

However, previous water analog experiments encountered challenges in controlling shot speed and fill times, leading to difficulty in validating computer simulations [80, 81]. Cleary et al [81] conducted a comparative analysis of water analog experiments and computer simulations, revealing reasonable correlations particularly during the initial filling stages. Notably, vacuum application has not been integrated into prior

water analog experiments to investigate its influence on the flow within the die cavity and shot system.

This study compares water analog experiments with flow simulations to validate the locations and quantity of entrapped air within the cavity during die casting. To emphasize the change in entrapped air with different vacuum levels, a vacuum pump was incorporated into the water analog experimental setup. Furthermore, aluminum specimens cast under varying vacuum levels underwent CT scanning for comparison to water analog experiments and computer simulations.

3.2 Experimental Design

3.2.1 Water Analog Experiments

The experimental setup, depicted in Figure 3.1 was specifically designed and constructed at the Ohio State University for this investigation. To replicate the HPDC process, precise control over the shot speed was achieved using a linear actuator. The linear actuator, powers by a servo driver and motor, was controlled by an Arduino board programmed with GRBL (Motion Control for Makers) code.

The plunger, crafted from a Teflon tube with a diameter of 25.4 mm and the 280.0 mm long shot sleeve, fashioned from plexiglass, were integral components. Additionally, a 3-D printed rectangular die, shown in Figure 3.2, was utilized. Figure 3.2(a) displays the 3-D printed die within its holder and Figure 3.2(b) is an annotated view with the major dimensions labeled. The rectangle die is 100 mm by 100 mm and is 5 mm thick.

Moreover, a scaled-down test specimen die, featured in Figure 3.3, was employed for water analog experiments. The specimen die was scaled down in order to fit into

the water analog experimental setup. Figure 3.3(a) exhibited the 3-D printed scaled down test specimen die within its die holder, with Figure 3.3(b) providing dimensional details. This test specimen die comprises of three flat plates of differing thicknesses (2 mm, 5 mm, and 3 mm) along with a round ASTM tensile bar measuring 6 mm in diameter.

A detailed view of the runner and gate of the scaled test specimen die, with the dimension of the thickest part labeled, is presented in Figure 3.4. The die also has two large overflows as shown in Figure 3.3. Both the rectangle die and the scaled down test specimen die were securely positioned within an aluminum block die holder, as depicted in Figure 3.1, ensuring stability throughout experiments.

Observation of flow within the die was facilitated by a clear polycarbonate plate cover die. High-speed videos capturing the filing process were recorded using a camera with a frame rate of 1000 fps. Sealing of the dies to prevent flashing was accomplished using clamps and an O-ring. Furthermore, a vacuum hose, connected to the top of the die near the overflow, was linked to a vacuum tank and pump, allowing for experimentation under various vacuum levels.

In the water analog experiments, water served as the casting fluid, with added food coloring to enhance visibility during the filling process. To emulate the HPDC process accurately, a two-stage shot profile was employed, featuring slow and fast shot speeds set at 0.4 m/s and 1.75 m/s, respectively.

During the vacuum phase of the experiments, a one-stage shot profile (solely a fast shot of 1.75 m/s) was adopted. This adjustment was necessary as the slow shot risked compromising the seal around the plunger, leading to a loss of the vacuum

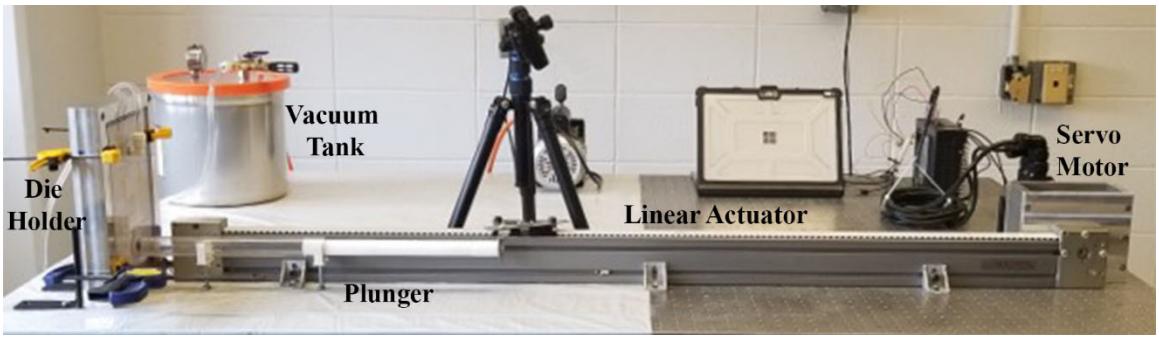

Figure 3.1: The image shows components of the water analog experimental setup, including the servo motor, linear actuator, plunger, die holder, and the vacuum tank.

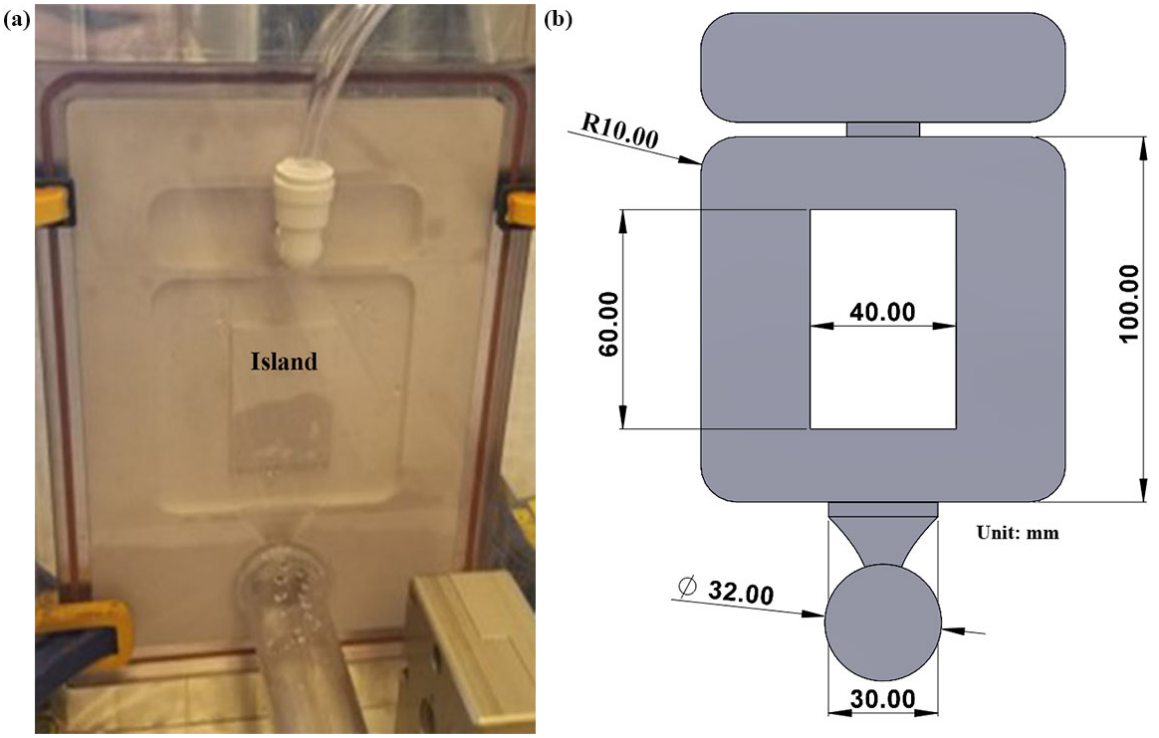

Figure 3.2: The rectangle die is depicted as follows: (a) showcasing the 3-D printed die within its holder, and (b) presenting the die with major dimensions labeled, thickness is 5 mm.

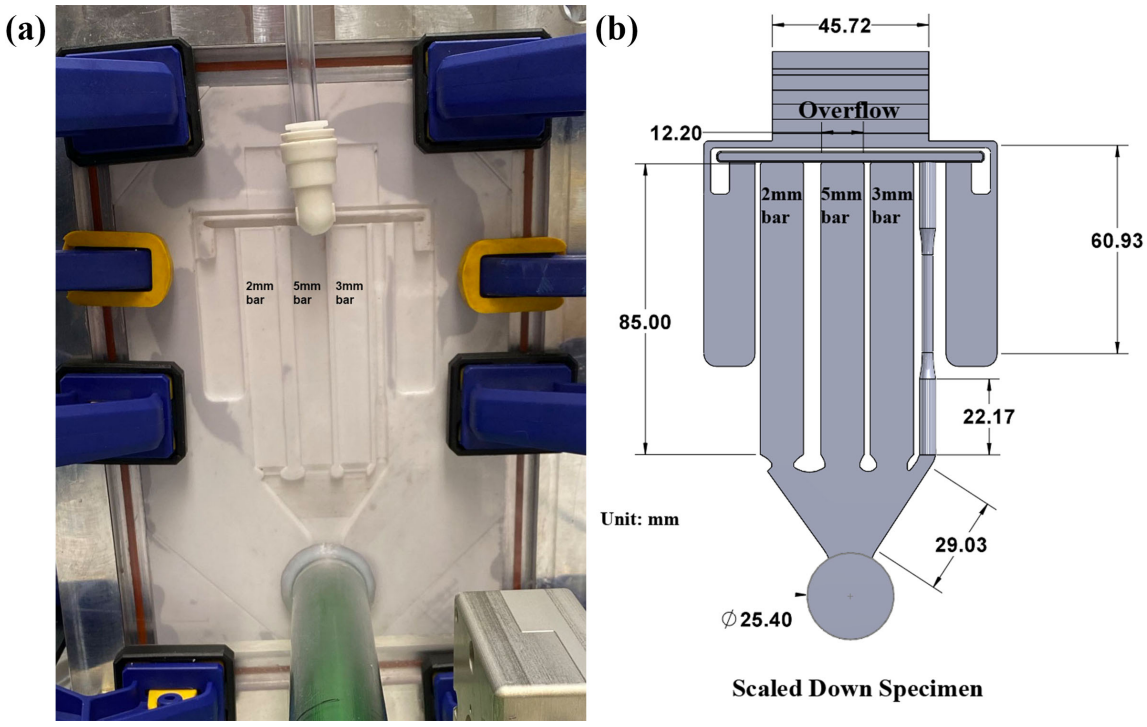

Figure 3.3: The scaled down test specimen die is shown as follows: (a) displaying the 3-D printed die within its holder, and (b) presenting the die with major dimensions labeled.

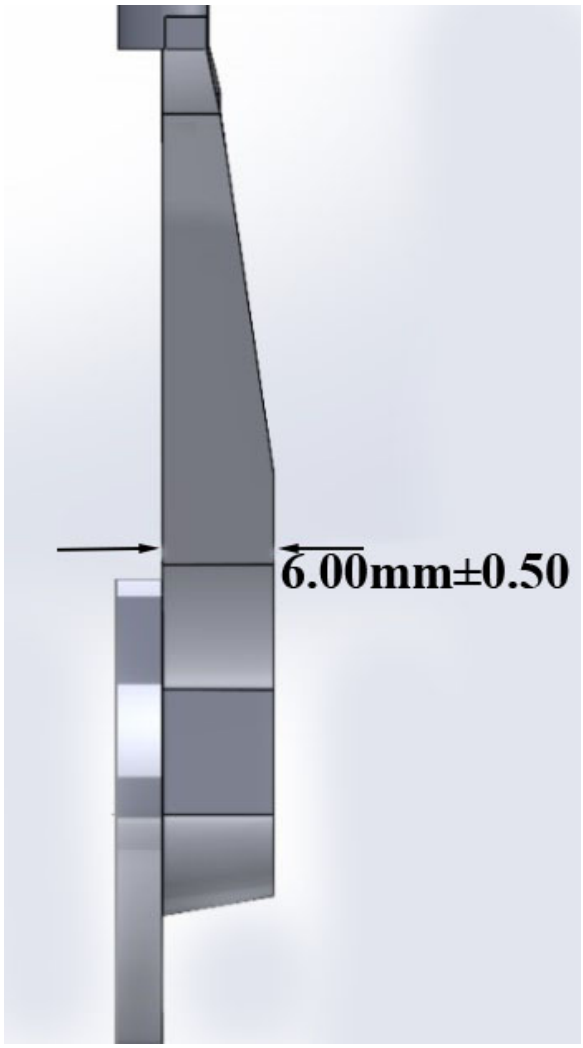

Figure 3.4: The side view of the gate and runner of the scaled down test specimen die is depicted.

Alloy	Si	Mg	Mn	Fe	Sr
AlSi7	6.9	0.16	0.43	0.17	0.009
AlSi9	10.7	0.31	0.49	0.23	-

Table 3.1: The compositions (in weight percentage) of the alloys utilized in the high pressure die casting trials. These composition were determined using Spark-OES (Optical Emission Spectrometry).

sealing. Three distinct vacuum levels were tested, corresponding to gas pressures of 1 bar, 265 mbar, and 100 mbar, as measured using the vacuum pump.

3.2.2 High Pressure Die Casting Trials

The high pressure die casting trials were carried out utilizing a 250-ton Bühler Die Casting machine located at the Center for Design and Manufacturing Excellence (CDME) at The Ohio State University (OSU) with a Fondarex vacuum unit (Highvac Economy 'C-250). Two distinct alloys were employed, as detailed in Table 3.1, these compositions were determined using Spark-OES (Optical Emission Spectrometry). One alloy, denoted as AlSi9, contained 9% silicon, while the other, termed AlSi7 contained 7% silicon.

Each alloy underwent casting trails under three vacuum levels. For AlSi7, the conditions included no vacuum, 120-mbar pressure, and 80-mbar pressure. On the other hand, AlSi9 was cast with no vacuum, 250-mbar pressure, and 75-mbar pressure.

Prior to casting, the melt underwent degassing at 1 bar for 20 minutes with nitrogen, followed by an addition of a sodium-free cleaning and degassing flux WFSF 71 (HA International, Westmont, IL). Subsequently, the melt was subjected to an additional 10 minutes of degassing with nitrogen after flux addition. The furnace

maintained a consistent melt temperature of 720 °C. The ejector die and shot sleeve temperatures were 147 °C and 184 °C, respectively, as determined by a thermal camera during steady-state conditions in the middle of a casting trial. Figure 3.5(a) depicts the full-size cast sample, while Figure 3.5(b) illustrated the full-size specimen die, annotated with majors dimensions. The density of the round bars were determined using the hydrostatic weighing method, with each round bar weighed three times in both water and air. At least three samples per vacuum level were measured. The 3 mm plates were machined into tensile bars, Figure 3.6 shows the dimensions of the tensile bar. Subsequently, scanned using a CT machine with a voxel size of 50µm. Two samples per condition were scanned. The machined tensile bars and round bars were tested using an MTC Criterion^{TM} Model 43 tensile tester at room temperature, with a cross head speed of 0.005 m/s. For microstructure analysis, the samples were prepared following standard metallographic procedures and imaged with an OLYMPUS BX3M-LEDR optical microscope.

3.3 Computer Simulations

3.3.1 MAGMASOFT® Simulations

MAGMASOFT® version 5.5, a finite volume-based casting software, was employed for computer simulations of water analog experiments and HPDC trials. Water served as the casting fluid, maintained at a constant temperature of 25°C. Refer to Table 3.2 for the water properties utilized in the simulation [113]. The same rectangle die and scaled-down test specimen die utilized in the water analog experiments were employed in the computer simulations. A one-stage shot profile with a shot speed

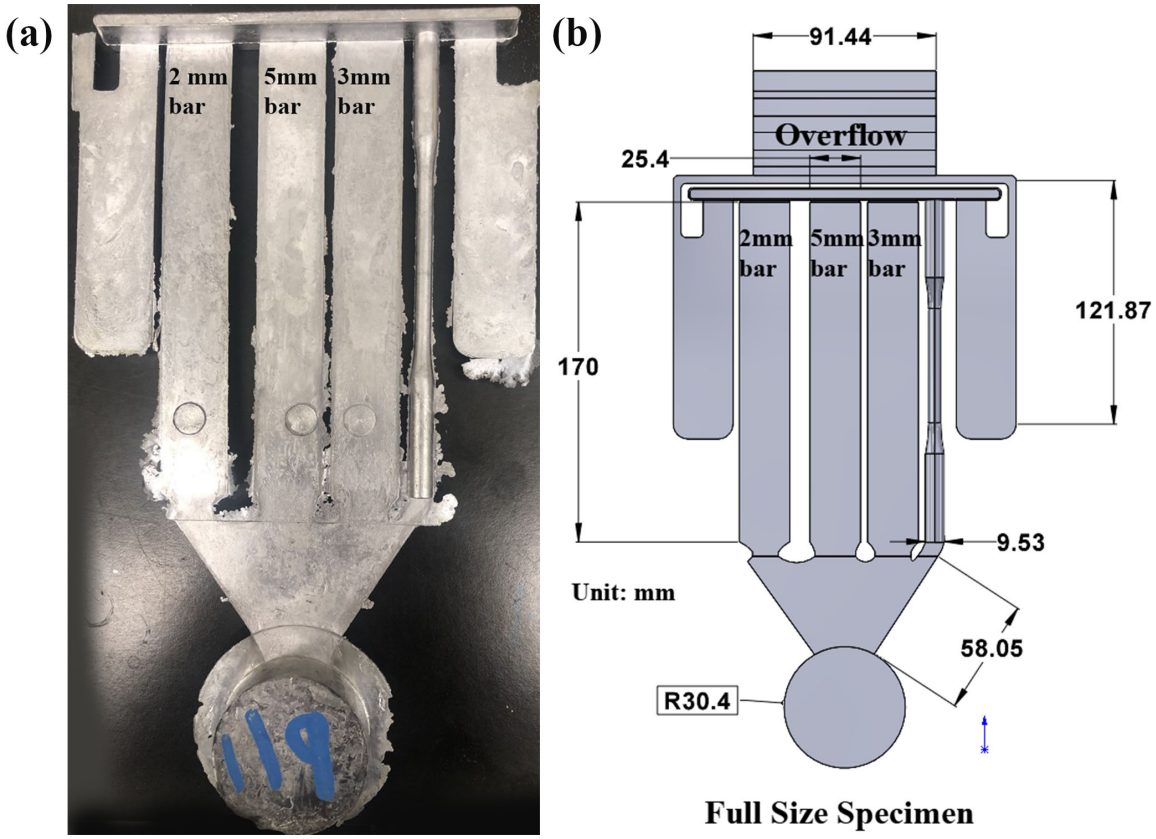

Figure 3.5: The full-size test specimen: (a) showcases the cast sample, while (b) displays the die with its major dimensions labeled.

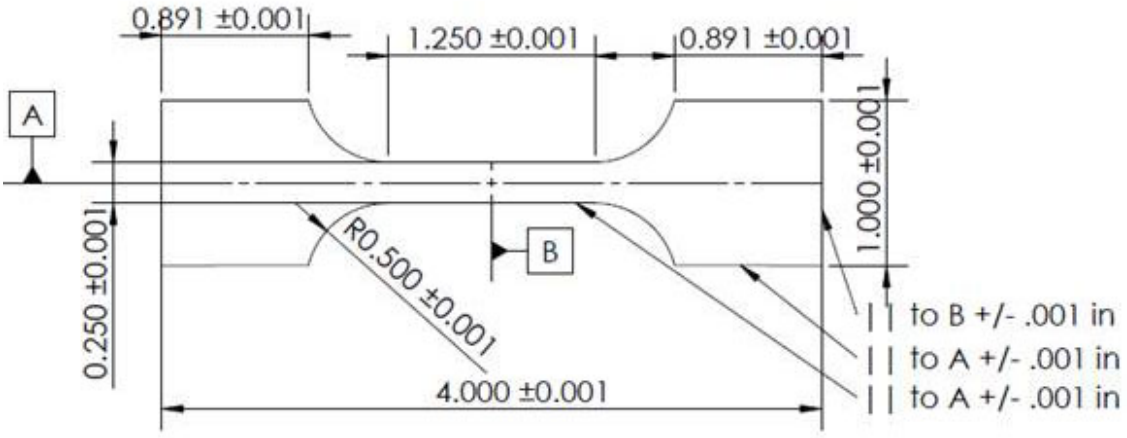

Figure 3.6: The dimensions of the tensile bar that was machined from the 3 mm plate.

of 1.75 m/s was used, and the shot chamber was included and simulated within the software.

For the rectangle die, three vacuum strengths were examined: 1 bar, 250 mbar added vacuum, and 100 mbar added vacuum. Similarly, for the scaled-down test specimen die, vacuum strengths of 1 bar, 200 mbar added vacuum, and 100 mbar added vacuum were utilized. The mesh comprised 1,130,000 cells in the cavity, with at least three cells across the thinnest sections.

Additionally, simulations were conducted for the full-size test specimen die used in the high pressure die casting trials. This simulation employed a two-stage shot profile with a slow-shot speed of 0.4 m/s followed by a fast shot speed of 1.75 m/s after a 7 second dwell time. The gate speed was 18 m/s. The mesh consisted of 1,016,000 cells in the die cavity, with a minimum of three cells across the thinnest sections. An alloy akin to AlSi9 served as the casting fluid. The simulations for the

Temperature, °C	Density, kg/m^3	Specific heat, $J/kg \cdot K$	Thermal conductivity, $W/m \cdot K$	Kinematic viscosity, m^2/s
25.0	997.0	4180	0.607	8.9370e-7

Table 3.2: The properties of water at 25° utilized in the simulations.

full-size specimen die used vacuum strengths of 1 bar, 250 mbar added vacuum, and 100 mbar added vacuum. Notably, 100 mbar was chosen as the strongest vacuum because MAGMASOFT® is unable to simulate vacuums below this threshold.

3.3.2 ProCAST Simulations

ProCAST is a finite element based casting software utilized for flow simulations. The simulations used the full size specimen die and used Al-9% Si as the casting fluid. A two-stage shot profile was employed, comprising a slow shot speed of 0.4 m/s followed by a fast shot speed of 1.75 m/s. Three different vacuum levels were simulated: no added vacuum, 261 mbar of added vacuum, and 79 mbar of added vacuum. Consistent with prior simulations, the shot chamber was included and modeled within the software.

3.4 Results

3.4.1 Repeatability of Water Analog Experiments

To assess the consistency of the water analog experiments, multiple trials with identical shot profiles and vacuum levels were conducted, each repeated at least three times. Repeatability of the experiments was evaluated by comparing results from three distinct locations during the filling process.

Repeatability of the Rectangular Die

Figure 3.7 illustrates the flow patterns within the rectangle die at the start, middle and end stages of filling in three repeatability water analog experiments, conducted under a vacuum pressure of 200 mbar. Figures 3.7(a)-(c) depict the initial filling phase, when water first enters the die cavity and comes into contact with the island. Subsequently, the water diagonally at a 45° angle to enter both sides of the cavity. Consistent flow patterns are observed across all three experiments during this initial phase. Figures 3.7(d)-(f) correspond to the near completion of filling, with water reaching the top of the cavity and then reversing the direction by 180° along the sides of the island. Air pockets are noticeable along the side of the island in all three scenarios, along with smaller air pockets near the bottom of the island. Figures 3.7(g)-(i) represent the end of filling process, characterized by minimal air pockets near the top corners of the island. Although the air pocket to the right of the island is consistently present, the size of the air pocket to the left of the island varies among the experiments. Nonetheless, all three experiments exhibit air pockets towards the end of filling.

Repeatability of the Scaled Down Test Specimen Die

Figure 3.8 presents a summary of repeatability experiment findings for the scaled-down test specimen die, conducted with the addition of vacuum. Figures 3.8(a)-(c) depict the experiments at the initial filling stage, where water begins to enter the flat plates. All three experiments exhibit similar filling progress; with the 5 mm plate just beginning to fill, while the 3 mm and 2 mm plates remained unfilled. As the 5 mm plate is centrally located, it is anticipated to be the first to fill.

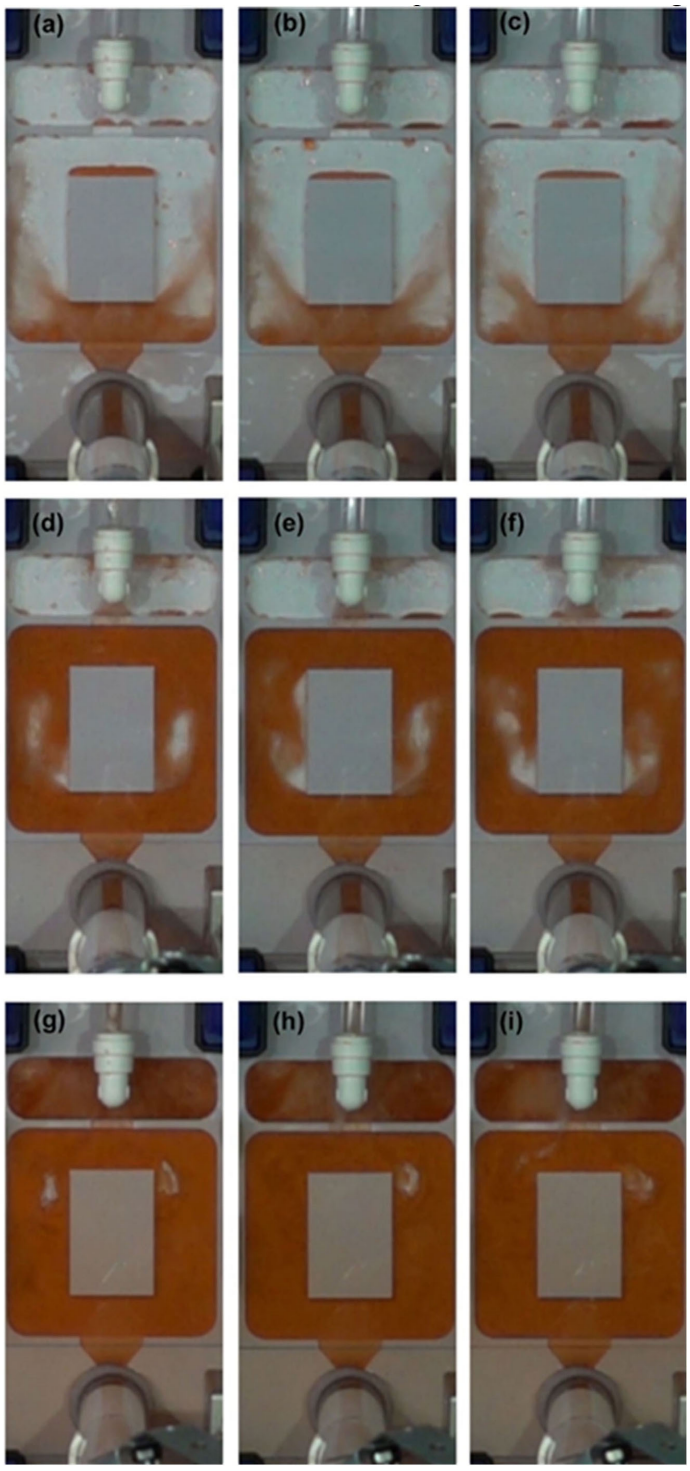

Figure 3.7: Water analog repeatability experiments for the rectangle die conducted with an added vacuum level of 200 mbar: (a-c) at the beginning, (d-f) in the middle, and (g-f) at the end of three repeated experiments.

Figures 3.8(d)-(f) illustrate the filling process when the plates are approximately 50% filled. Despite the 5 mm plate consistently filling to a higher level than the 2 mm and 3 mm plates, minor variations are observed among the three experiments. Notably, Figure 3.8(d) shows the 5 mm plate filled higher compared to Figures 3.8(e) and (f). Additionally, the fill front in the 5 mm plate appears flatter in Figure 3.8(e) compared to Figure 3.8(d) and (f), where it is more angled. While Figures 3.8(e) and (f) exhibit reasonable agreement, Figure 3.8(d) displays slightly higher plate filling. These discrepancies, although minor underscore the challengers in maintaining precise alignment and control across manual experiments, highlighting the limitations of the water analog method.

Figures 3.8(g)-(i) depict the final stages of filling, with the 5 mm plate filled and the 3 mm and 2 mm plates nearly filled. Overall, there is satisfactory agreement among the three filling profiles. However, in Figure 3.8(g), filling in the 2 mm and the 3 mm plates lags slightly compared to the other two experiments. Entrapped air is visible in the gate region across all three experiments, depicted by white areas mixed with the green water.

3.4.2 Effect of Vacuum in Water Analog Experiments

Effect of Vacuum on Rectangular Die Cavity Fill

Figure 3.9(a, d, and g) presents the results of water analog experiments conducted using the rectangle die without vacuum (1 bar gas pressure), while Figures 3.9(b, e, and h) and Figures 3.9(c, f, and i) depict the cavity fill with vacuum levels of 200 mbar and 100 mbar gas pressure, respectively. The initial filling stage for the three experiments is illustrated in Figures 3.9(a)-(c), where water has just entered the

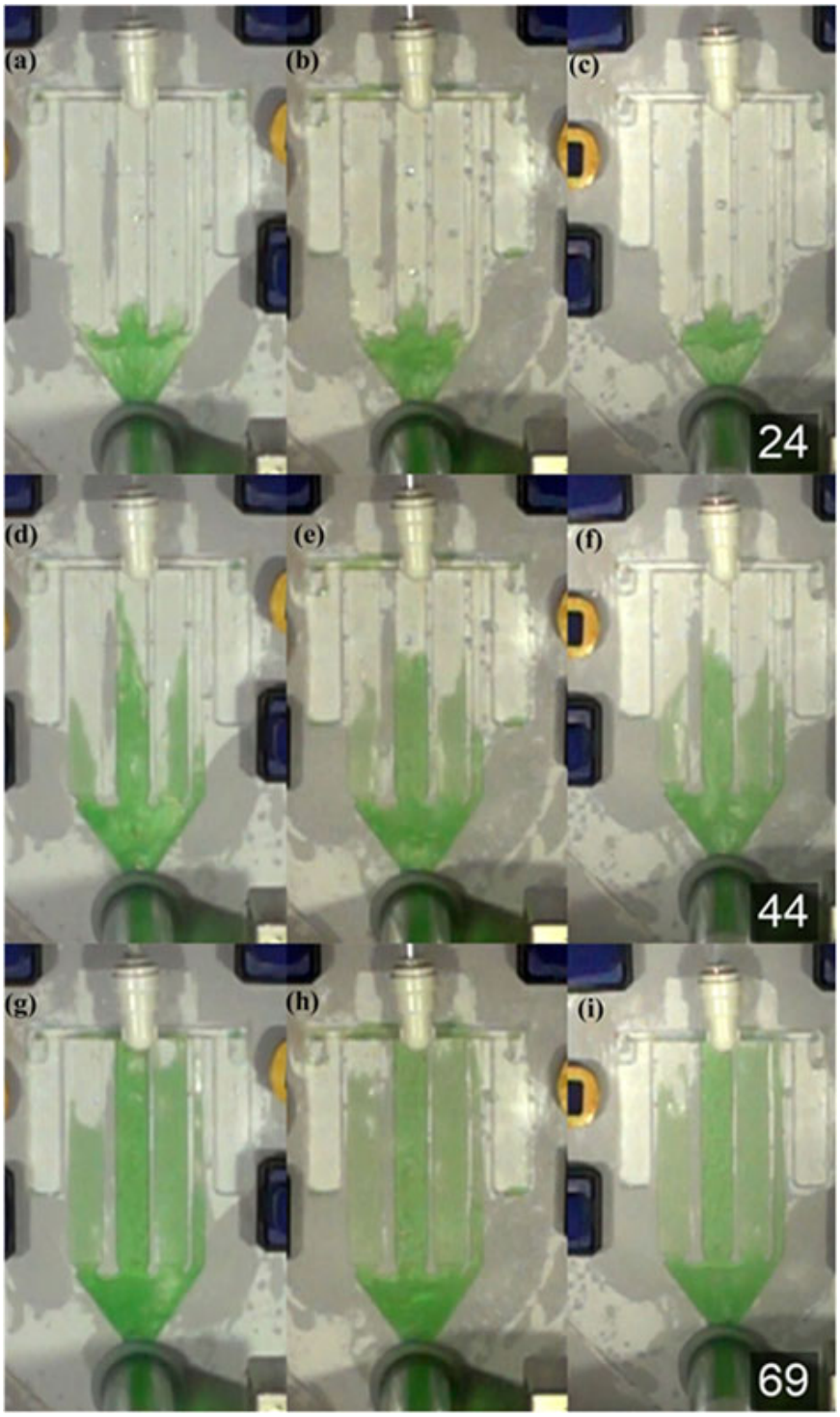

Figure 3.8: The water analog repeatability experiments conducted on the scaled-down test specimen die: (a-c) at the beginning, (d-f) in the middle, and (g-i) near the end of filling, when the 5mm plate is filled, across three repeated experiments.

cavity and comes into contact with the island. These images precede Figures 3.7(a)-(c), capturing the moment when the water first hits the island and begins to move towards the wall. Figures 3.9(d)-(f) depict the phase where water travels along the top of the cavity and then curls back down along the sides of the island, resulting entrapping air. The largest remaining air pocket is observed in Figure 3.9(d) at a pressure of 1 bar. As a vacuum is applied, the size of the air pocket diminishes. Near the base of the island, light spots indicate the presence of air mixed with the water. Figures 3.9(g)-(i) depict stages closer to completion, where the water wave has encircled air on either sides of the island and is rising towards the overflow. Across all three figures, air pockets persist within the cavity. These air pockets diminish in size with the application of vacuum, particularly with stronger vacuum levels. Notably, in Figure 3.9(i), characterized by the strongest vacuum (100 mbar gas pressure), the remaining air pockets are the smallest among the depicted experiments. Consequently, a discernible trend emerges, indicating a reduction in air pocket size with increasing vacuum strength.

Effect of Vacuum using Scaled Down Test Specimen Die Cavity Fill

Figures 3.10 present the results of water analog experiments utilizing the scaled-down test specimen die during the initial stage of filling, when the 5 mm plate is approximately halfway filled. Entrapped air is visible in the gate region across all three figures; however, the introduction of vacuum diminished the amount of entrapped air. Additionally, turbulent flow results in entrapped air within all three 5 mm plates. In Figure 3.10(d) the plates are predominately filled, whereas the 2 mm plate exhibits incomplete filling in Figures 3.10(e) and (f). Entrapped air is observed in the 2 mm plate across all three images, yet it is absent in the gate region. Figures 3.10(g)-(i)

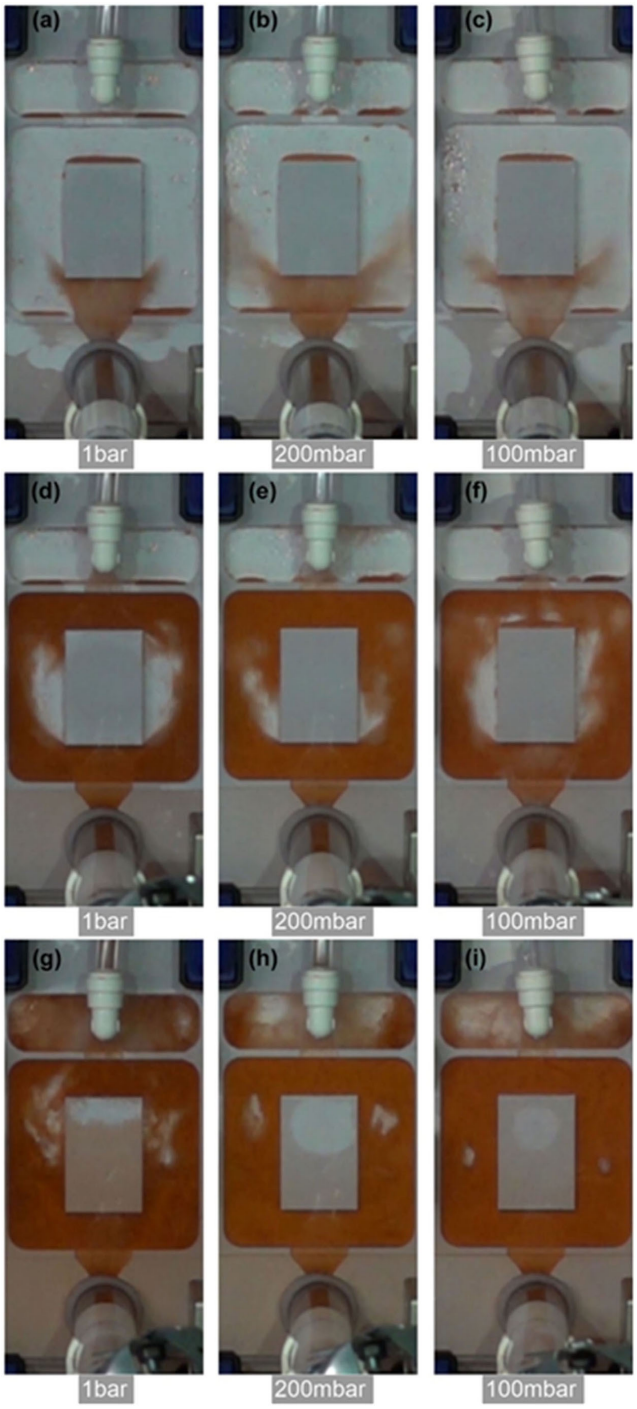

Figure 3.9: The water analog experimental results for the rectangle die using varying vacuum levels. (a), (d), and (g) represent experiments with no added vacuum, (b), (e), and (h) show results with 200 mbar of added vacuum, and (c), (f), and (i) depict experiments with 100 mbar of added vacuum.

correspond to the stage when the specimen die is fully filled. In all three experiments, entrapped air in the gate region is absent, though some remains visible in the 2 mm plate in Figures 3.10(g) and (h). Notably, the experiment utilizing the strongest vacuum (100 mbar gas pressure) exhibits significantly less entrapped air in the 2 mm plate, indicating that the stronger vacuum effectively removes more air from the cavity compared to weaker vacuums. Some entrapped air is visible near the top of the 3 mm plate in Figure 3.10(g), yet it is notably reduced in Figures 3.10(h) and (i). These water analog experiments clearly illustrate the reduction in entrapped air when vacuum is applied to evacuate air from the cavity before filling.

3.4.3 Effect of Vacuum in Simulations

Effect of Vacuum Using Rectangle Die

Figures 3.11(a) and (d) depict the MAGMASOFT® air results for the rectangle die simulation without added vacuum, while Figures 3.11(b) and (e) represent simulations with a 200 mbar added vacuum, and Figures 3.11(c) and (f) show simulations with a 100 mbar added vacuum. Figures 3.11(a)-(c) provide insight into the air distribution within the die cavity when it is 80% filled. Residual air is observed throughout the die cavity, notably in a sizeable pocket on the left side of the island. The introduction of vacuum leads to a reduction in the size of this pocket, mirroring the trend observed in Figures 3.9(d)-(f) of the water analog experiments, where substantial air pockets flank the island. It is important to note that while both water and air escape through the vacuum vent in water analog experiments, the simulation only accounts for air escaping through the vent. This discrepancy could yield slightly different results, but overall, there is reasonable alignment between the experimental and simulation results. Additionally, residual air beneath the island decreases with

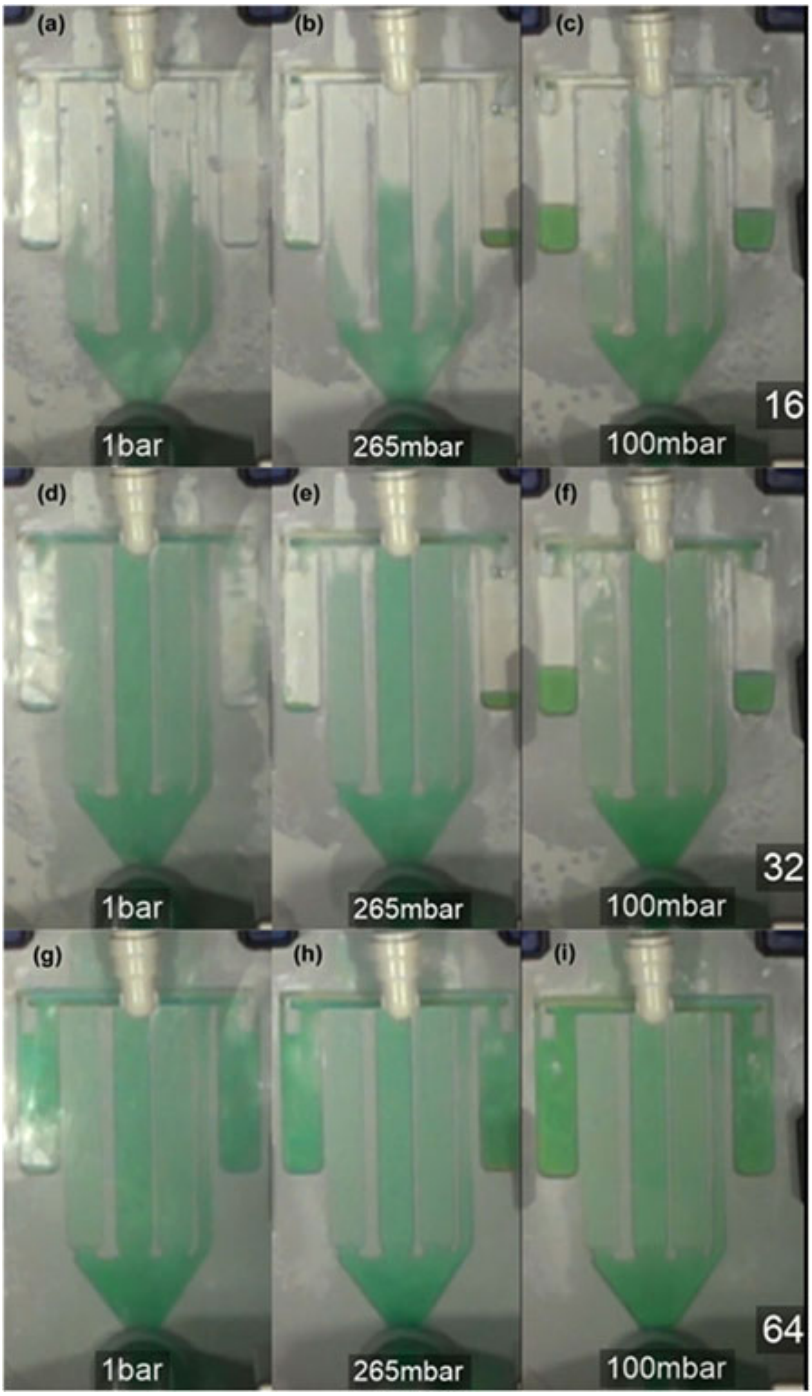

Figure 3.10: The water analog results for the scaled down test specimen die show different vacuum conditions: (a), (d), and (g) are experiments without added vacuum, (b), (e), and (h) are experiments with 265 mbar of added vacuum, and (c), (f), and (i) are experiments with 100 mbar of added vacuum. (a), (b), and (c) correspond to the stage when the 5 mm plate is halfway filled, (g), (h), and (i) depict when the plates are mostly filled, and (g), (h), and (i) correspond to the completion of filling.

the vacuum application. Figures 3.11(d)-(f) correspond to the scenario where the die cavity is 100% filled, yet air remains below the island, albeit diminishing in size vacuum application. The air pocket on the right side of the island has migrated to the top of the island. Notably, simulations without vacuum exhibit a larger air pocket above the gate compared to the simulations with added vacuum. Although differences between Figures 3.11(e) and (f) are minor and do not indicate substantial changes in remaining air when vacuum strength changes from 200 mbar to 100 mbar, water analog results exhibit more pronounced changes, particularly in Figures 3.9(g)-(i).

Effect of Vacuum using the Scaled Down Test Specimen Die

Figure 3.12(a), (d), and (g) depict the temperature results from the simulations run without added vacuum. These figures show flow behavior of the fluid through the die during casting. Figure 3.12(b), (e), and (h) show the temperature results from the simulation with an added vacuum of 200 mbar, while Figure 3.12(c), (f), and (g) present results with an added vacuum of 100 mbar gas pressure. Figure 3.12(a)-(c) correspond to when the die is 47% filled. Analogously to Figure 3.10(a)-(c), these results indicate the flow of fluid along the edges of the plates. Notably, in Figure 3.12(a)-(c), the 5 mm plate appears more filled than the 2 mm and 3 mm plates, despite the simulation suggesting uniform filling of all three plates. This disparity could be attributed to differences in die materials: the simulation employs H13 die steel, while the water analog model uses a polymer die.

Figure 3.12(d)-(f) represent the temperature results when the die is 71% filled. These results show mostly filled plates with some remaining air pockets. Similar to the water analog results in Figure 3.10(d)-(f), the 2 mm plate retains the most air

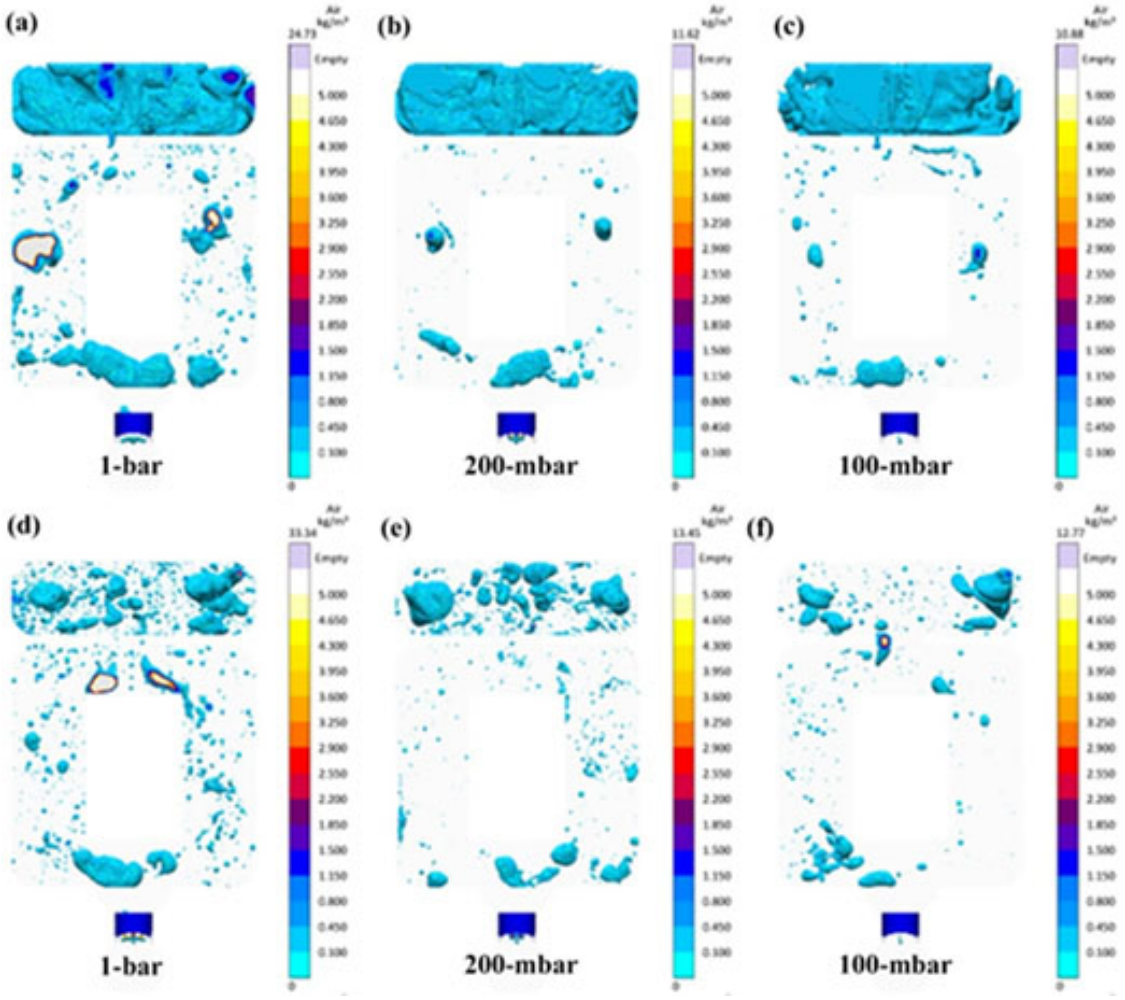

Figure 3.11: The simulation air results for the rectangle die are as follows: (a) and (d) are simulations without added vacuum, (b) and (e) represent conditions with 200 mbar of added vacuum and (c) and (f) are simulations with 100 mbar of added vacuum. (a), (b) and (c) correspond to the die being filled to 80%, whereas (d), (e), and (f) depict the die being completely filled.

near the end of filling. Both the simulation and water analog results agree that air pockets will likely remain near the top of the 2 mm plate at the conclusion of filling.

Figure 3.12(g)-(i) display the temperature results from when the die is 80% filled. Notably, there is still an air pocket visible in Figure 3.12(h) and (i) at the top of the 2 mm plate. However, based on the results, this pockets is distinct from the one seen in Figure 3.12(e) and (f), as it appears to be pushed upward from lower with the plate.

Figure 3.13(a)-(c) depict the air simulation results for the scaled-down test specimen die at the onset of filling. Figure 3.13(a) depicts simulation without added vacuum, while Figure 3.13(b) and (c) are the simulations with 200 mbar and 100 mbar of gas pressure, respectively. All three simulations reveal the presence of air within the cavity after the plates started to fill, with Figure 3.13(b) and (c) displaying a similar amount of air remaining in the gate. This observation aligns with findings from the water analog experiments, where entrapped air is also observed in the gate region. Figures 3.13(d)-(f) represent the mid-filling stage when the plates are mostly filled. A reduction in the volume of remaining air within the gate is evident with vacuum application. Notably, Figures 3.13(e) and (f) display closely matched results, suggesting that a 100 mbar difference in vacuum pressure does not significantly reduce air content based on simulations. Figures 3.13(g)-(i) correspond to the end of the filling simulation, showcasing residual air in the runner across all scenarios, albeit with decreased volume under vacuum-assisted filling. Discrepancies between the simulation and water analog experiments may arise from entrapped air in the gate region, that is undetectable by current methods. It's important to acknowledge that in the water analog experiments, the colored water might obscure the presence of air pockets, potentially leading to residual air remaining undetected in the runner. In

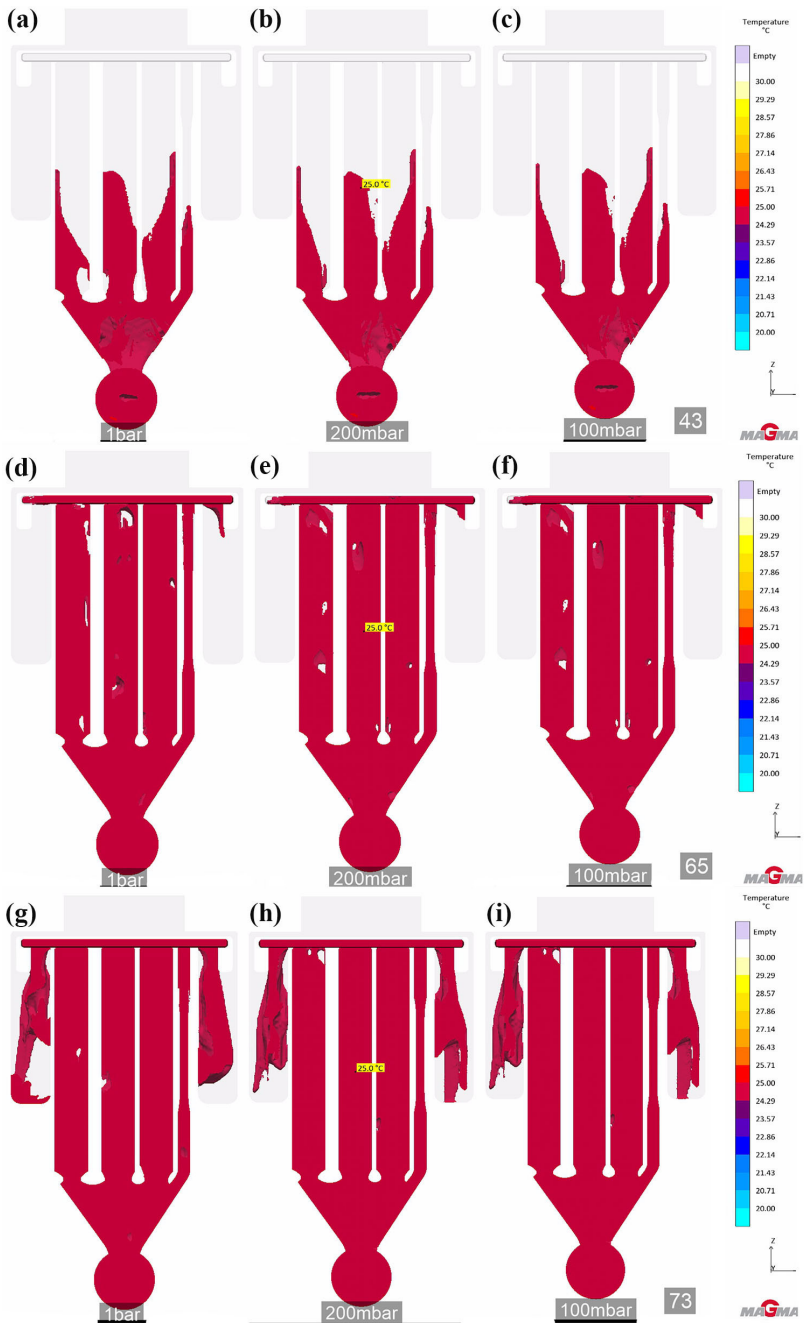

Figure 3.12: The simulation temperature results for the scaled-down test specimen die. (a), (d), and (g) correspond to simulations without added vacuum, while (b), (e), and (h) represent simulations with 200 mbar of added vacuum, and (c), (f), and (i) depict simulations with 100 mbar of added vacuum. (a), (b), and (c) show the temperature result when the die is 47% filled, (d), (e), and (f) show the results at 71% filled, and (g), (h), and (i) display the results at 80% filled.

contrast, the simulation results utilize an x-ray view, providing comprehensive visibility of all the remaining air within the die cavity. This disparity in observation methods accounts for differences in results.

In Figure 3.13(g), a notable air pocket near the top of the round bar is observed, significantly diminished vacuum application. Furthermore, the simulation also predicts that vacuum application would eliminate any remaining air in the 2 mm plate, contrasting with the prediction of a small pocket of air predicted in the 2 mm plate without an applied vacuum. Thus, the employment of vacuum demonstrates efficacy in reducing entrapped air within the cavity post-filling.

In Figures 3.14(a)-(c), the simulation air results for the cross-section of the scaled-down test specimen die are depicted, representing the early stage of filling. The cross-section, located at the midpoint of the 5 mm plate and the runner, offers insight into the airflow dynamics. Specifically, Figure 3.14(a) is without added vacuum, while Figures 3.14(b) and (c) demonstrate the effects of applying vacuum pressures of 200 mbar and 100 mbar gas pressure, respectively.

Effect of Vacuum using Full-Size Die

Figure 3.15 depicts the air results obtained from simulations conducted on the full-size test specimen die, showcasing three distinct vacuum strengths. Figures 3.15(a), (d), and (g) represent the simulation without added vacuum. Figures 3.15(b), (e), and (h) depict results with a vacuum level of 250 mbar, while Figures 3.15(c), (f), and (i) showcase the simulation a vacuum pressure of 100 mbar.

Examining Figures 3.15(a)-(c), which depict the initial stage of filling, it's evident that air remains in the gate region across all simulations, consistent with observations

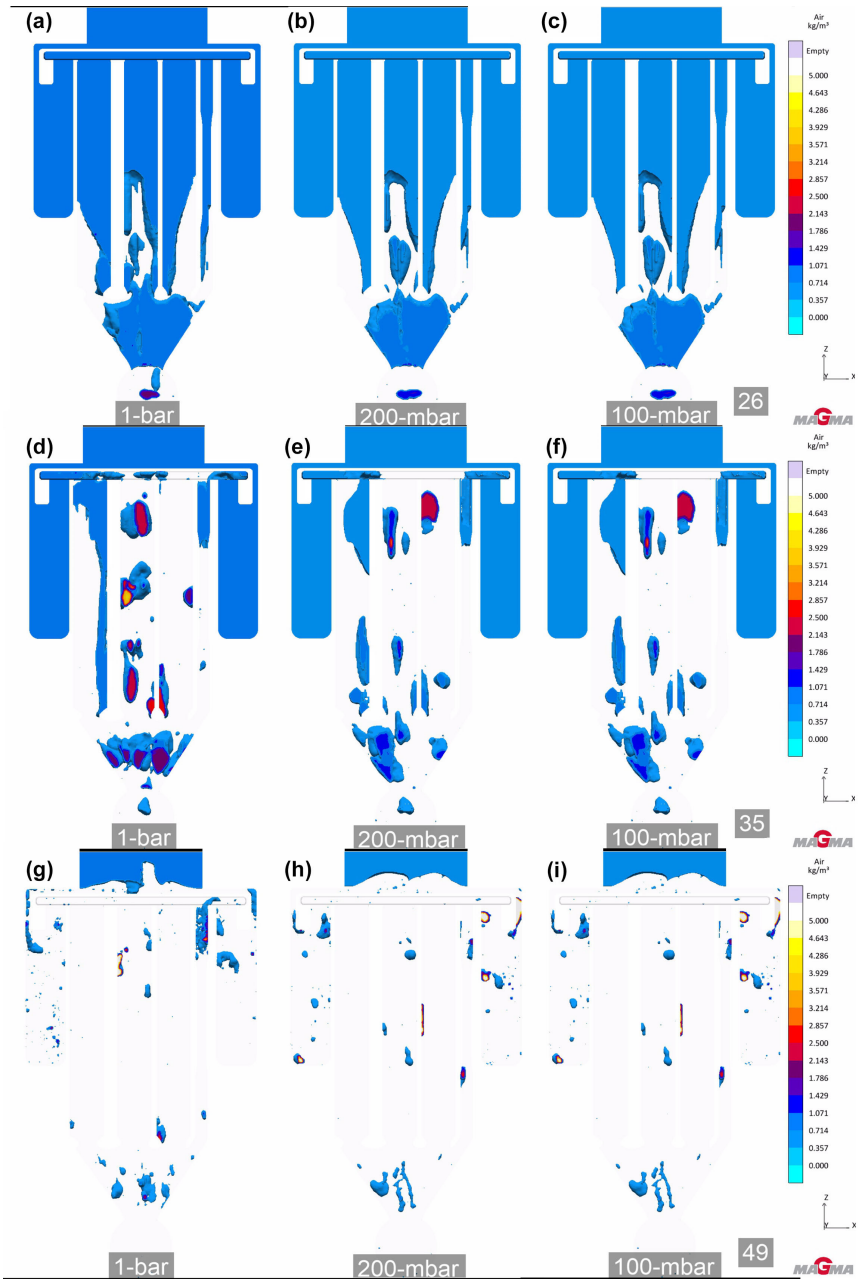

Figure 3.13: The simulation air results for the scaled-down test specimen die are presented. (a), (d), and (g) depict simulations without added vacuum, while (b), (e), and (f) are simulations with 200 mbar of added vacuum. Additionally, (c), (f), and (i) showcase simulations with 100 mbar added vacuum. (a), (b), and (c) represent data from the beginning of filling, (d), (e), and (f) capture the mid-filling stage when the plates are mostly filled, and (g), (h), and (i) are from the end of filling when the die is completely filled.

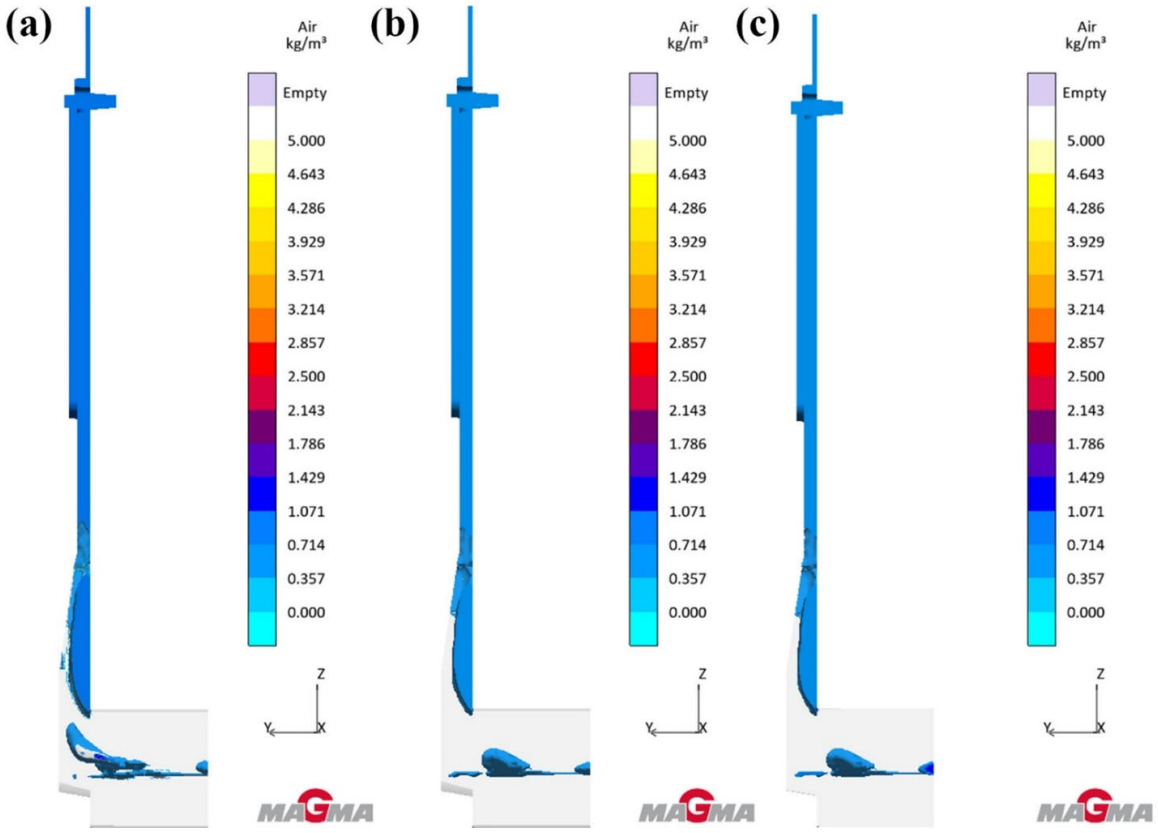

Figure 3.14: The simulation air results for the cross-section of the scaled down test specimen die. In (a), no vacuum is applied, while (b) depicts the simulation with a 200 mbar added vacuum, and (c) shows the result with a 100 mbar added vacuum. There images were captured during the initial stage of filling when water had just entered the die cavity.

from the scaled-down specimen die. Notably, a consistent air bubble is observed in the 3 mm plate, with its size decreasing with higher vacuum strength.

As the filling progresses towards completion, represented by Figures 3.15(d), (e), and (f), air retention in the plates and round bars in noticeable. Particularly, Figure 3.15(d) reveals a significant amount of air remaining in the 3 mm plate, which is reduced with the introduction of a 250 mbar vacuum, as seen in Figure 3.15(e). This reduction corresponds well with findings from the scaled-down specimen die simulations. Additionally, the presence of air in the 5 mm plate diminishes with the increasing vacuum strength.

Figures 3.15(g) - (i) depict the end of filling stages. The residual air in all die cavities decreases with the application of vacuum. In Figure 3.15(g), a considerable amount of air persists within the 3 mm plate. Examination of Figures 3.15(h) and (i) reveals a reduction in both the quantity and size of remaining air pockets within the 3 mm plate, particularly notable in Figure 3.15(i). Contrasting these findings with the water analog results presenting in Figures 3.10, it's evident that there is significantly less residual air within the 2 mm plate in the simulation data. Notably, the water analog results displayed entrapped air in the 2 mm plate, predominantly observable in Figures 3.10(g) and (h). Despite this slight variance, there exists a fair overall agreement between the water analog results and the simulation results. Notably, the simulation results depicted in Figure 3.15 underscores the efficacy of vacuum application in reducing air entrapment within the die cavities.

Figure 3.16(a)-(c) show the air distribution within the cross-section of the full-size specimen die. These images were sectioned through the middle of the 5 mm plate, extending through the runner and gate. Figure 3.16(a) corresponds to simulations

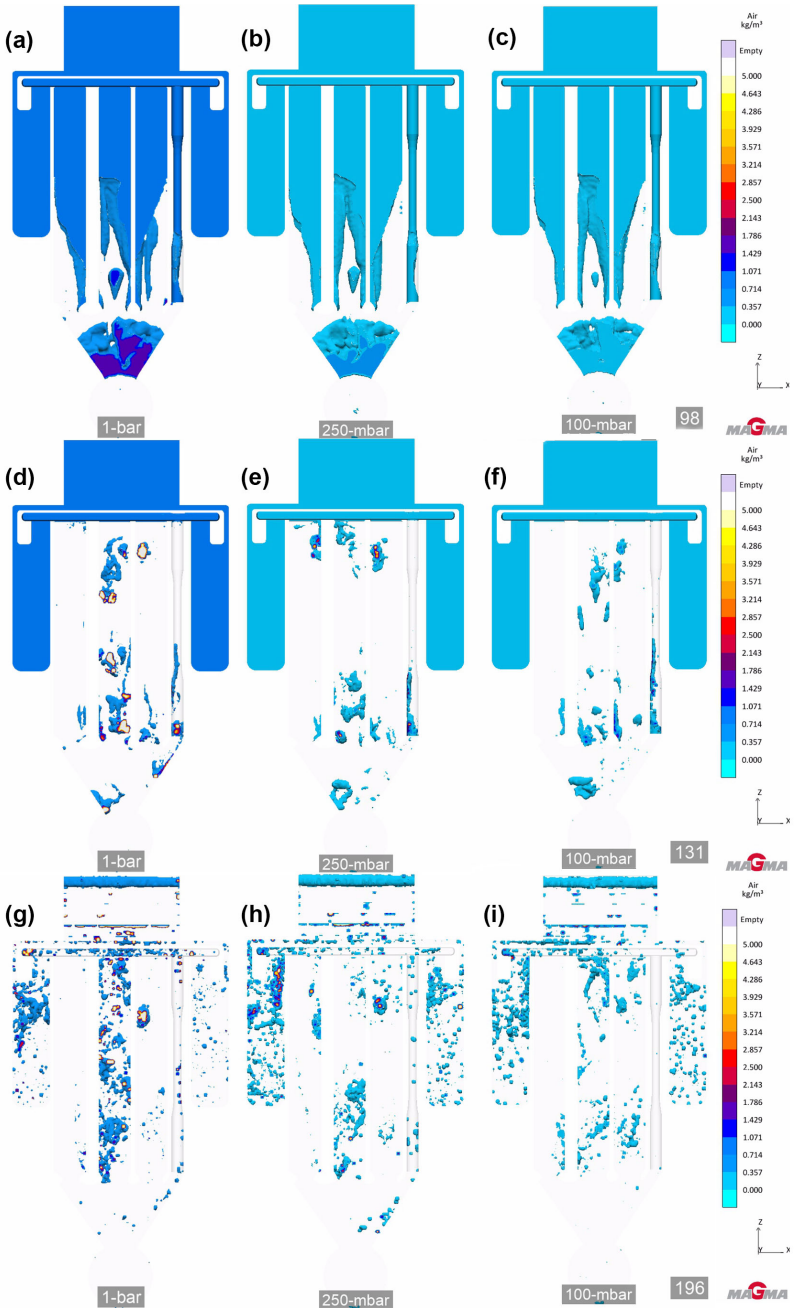

Figure 3.15: The air results obtained from simulation conducted on the full-size specimen die. (a), (d), and (g) correspond to simulations conducted without added vacuum. (b), (e), and (h) represent results obtained with a vacuum level of 250 mbar, and (c), (f), and (i) are with a vacuum pressure of 100 mbar. (a), (b), and (c) capture the initial stage of filling, while (d), (e), and (f) depict the middle of the filling process, when the plates and round bar are filled. (g), (h), and (i) are from the end of the filling process, when the die is finished filling.

conducted without an added vacuum, while Figure 3.16(b) and (c) represent simulations with vacuum levels of 250 mbar and 100 mbar, respectively. These images capture the initial stage of filling, shortly after the frame represented in Figure 3.14. In all three images, air is observed within the runner and the fluid behind is the air, similar to the observations in Figure 3.14. Notably, Figure 3.16(a) exhibits more air within the runner compared to Figures 3.16(b) and (c). The application of vacuum proves effective in reducing the amount of air within the cavity during the filling process.

Figure 3.17(a) depicts the total air remaining in the cavity over time for three vacuum levels, while Figure 3.17(b) provides a closer view toward the end of the filling. These plots commence at the onset of filling, following a 7-second dwell time. The black line represents the simulation without added vacuum, the red line denotes the simulation with a 250 mbar added vacuum, and the blue line corresponds to the simulation with a 100 mbar added vacuum. Notably, the simulation without added vacuum exhibits a higher remaining air mass in the cavity upon the completion of filling. Conversely, the simulations with added vacuum yield similar remaining air mass values. Table 3.3 presents the numerical data regarding the remaining air mass total in the cavity post-filling for the three vacuum levels. Specifically, the simulation without added vacuum retains more than double the amount of air mass compared to the 100 mbar vacuum simulation, 47,900µg versus 20,900µg, respectively. Moreover, the difference between the two simulations with added vacuum is more pronounces, registering 24,700µg for the 250 mbar added vacuum simulation and 20,900µg for the 100 mbar vacuum simulation. This analysis underscores how the application of

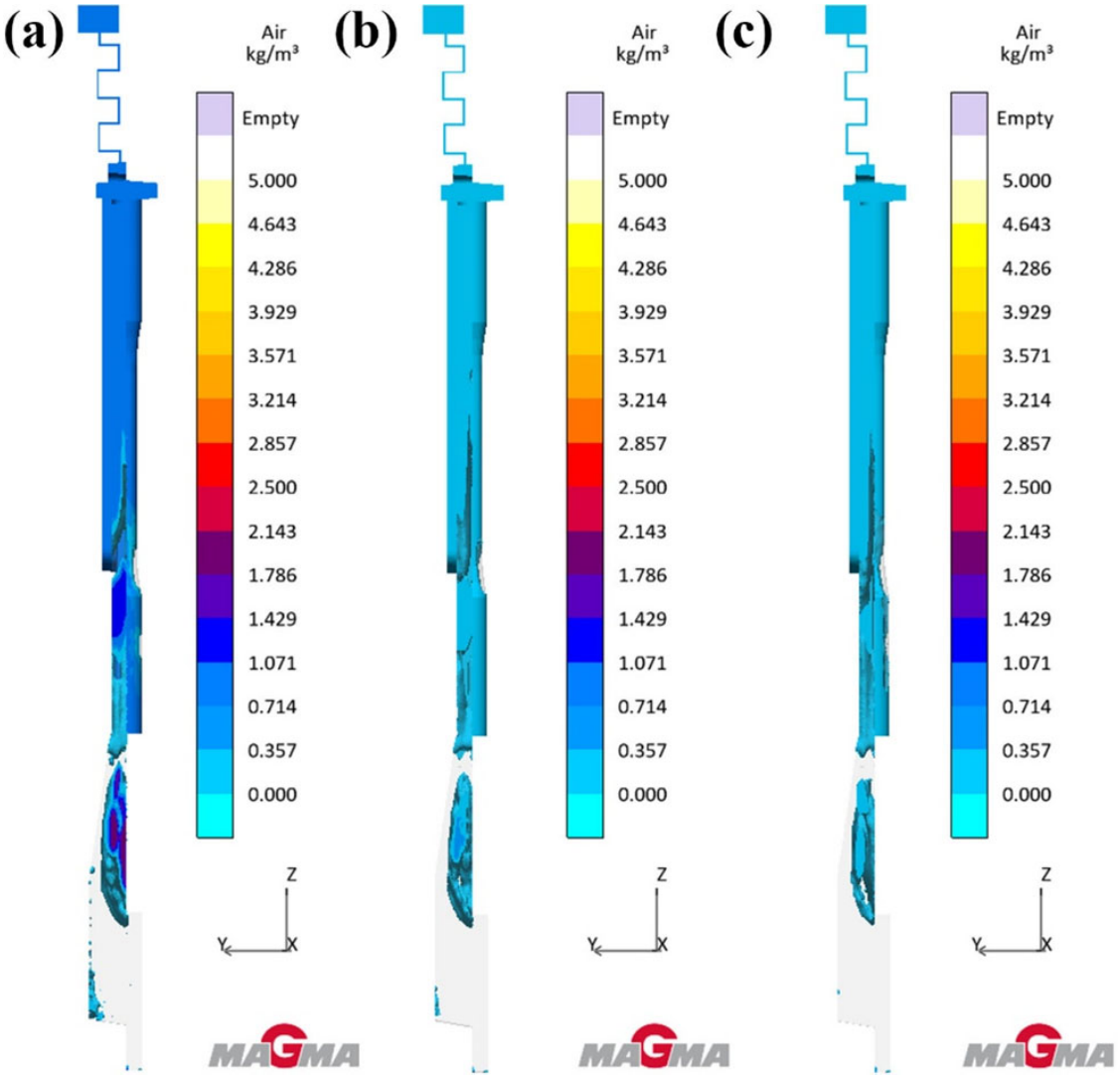

Figure 3.16: The images depict simulation air results for the cross-section of the full-size specimen die. In (a) no vacuum is applied, while (b) represents the scenario with 250 mbar of added vacuum and (c) depicts a simulation with 100 mbar of added vacuum. These images capture the early stage of filling.

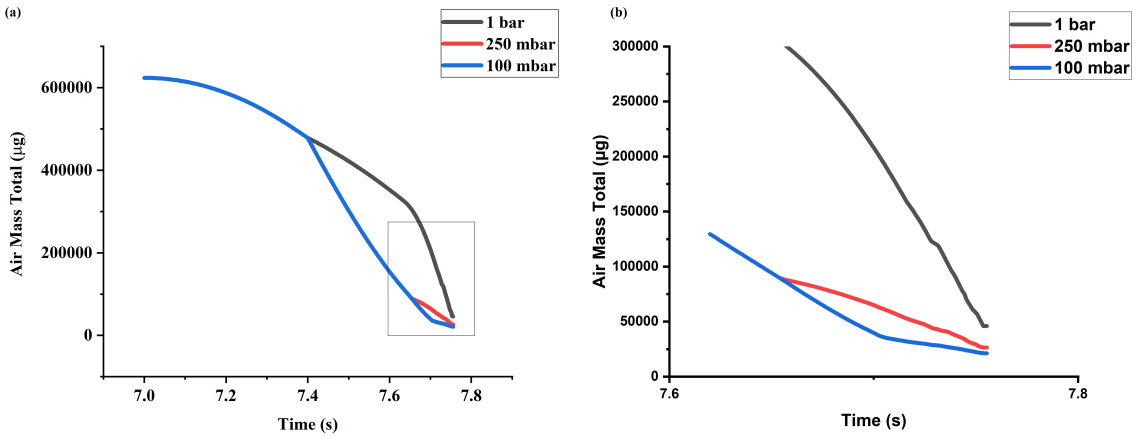

Figure 3.17: The air mass total plotted against time for the full-size specimen die. Three simulations are depicted, corresponding to vacuum level of 1 bar, 250 mbar and 100 mbar. (a) presents the complete time span, while (b) is a magnified view focusing on the latter stages the filling process.

vacuum can reduce the residual air content post-filling, with higher vacuum levels leading to further reductions in air mass.

Effect of Vacuum in ProCAST

Figure 3.18 depicts the gas pressure results obtained from the simulation. The top row corresponds to the initial stage of filling, while the middle row represents the midway point. The bottom row depicts the scenario when the cavity achieves full filling. Notably, even in simulations lacking added vacuum, residual gas persists within the gate. In contrast to MAGMASOFT® air result, the gas pressure results do not indicate the presence of air remaining in the cavity after the filling process is concluded.

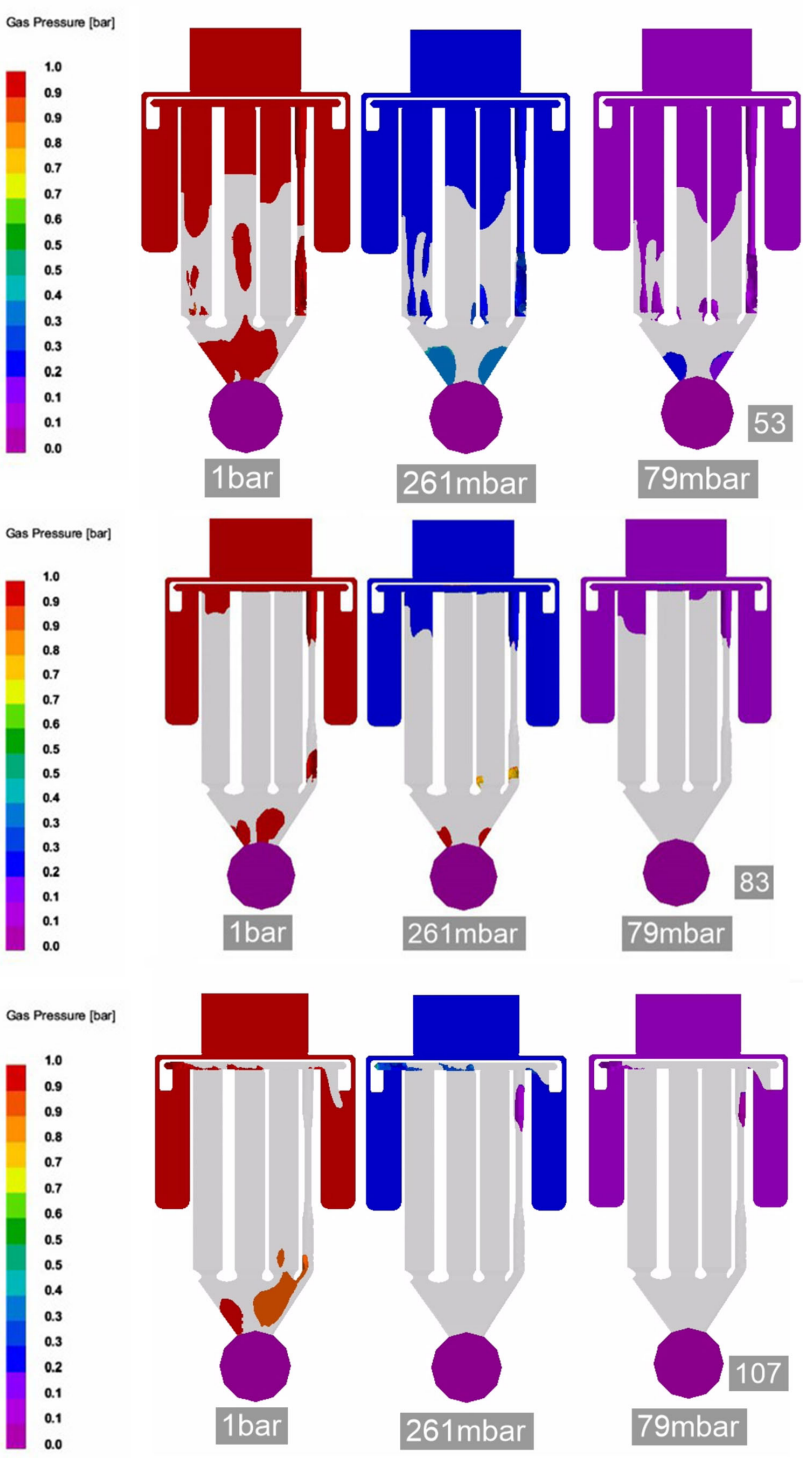

Figure 3.18: The simulation results for gas pressure encompass scenarios with 1 bar, 261 mbar, and 79 mbar of added vacuum.

Vacuum Level (mbar)	Air Mass Total (μg)
1000	45900
250	24700
100	20900

Table 3.3: The total air mass air mass remaining in the cavity upon completion of filling for the full-size specimen die. The simulations were conducted with added vacuum levels of 1 bar, 250 mbar, and 100 mbar.

3.4.4 Effect of Vacuum in High Pressure Die Casting Samples

Effect of Vacuum on Microstructure

Figure 3.19 displays the microsctructure of the AlSi7 alloy in its as-cast state under varying vacuum levels: 1 bar, 120 mbar, and 75 mbar. These images reveal a reduction in porosity as the vacuum strength increases. Figure 3.19(a) and (d) depict samples cast without additional vacuum, while Figure 3.19(b) and (e) show samples cast with 120 mbar vacuum, and Figure 3.19(c) and (f) illustrate samples cast with 75 mbar vacuum. These specimens were cut from the bottom of the 3 mm plate, near the gate. Figure 3.19(a) and (d) both exhibit gas porosity, whereas samples cast with vacuum exhibit significantly reduced gas porosity.

Effect of Vacuum on Density

Table 3.4 presents the density measurements of the round bars under varying vacuum levels, assessed via the hydrostatic weighing method. Samples cast without added vacuum exhibit the lowest density, indicative of porosity within the samples.

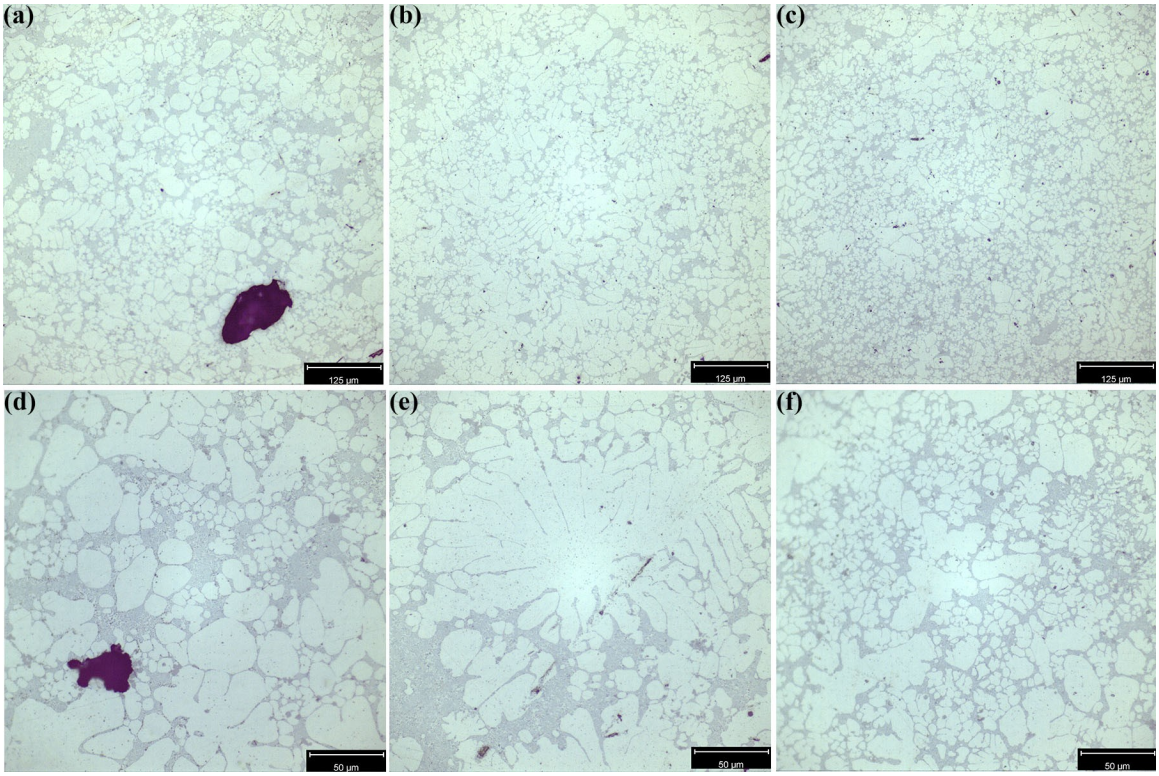

Figure 3.19: The optical microscope captures the 3 mm plate of the AlSi7 alloy under different vacuum conditions. In (a) and (d), the pressure is at 1 bar, while (b) and (e) represent 120 mbar, and (c) and (f) depict 75 mbar of additional vacuum.

Vacuum Level ($mbar$)	Density (g/ml)	Standard Deviation
1000	2.65	0.11
250	2.66	0.07
125	2.66	0.03
75	2.68	0.07

Table 3.4: Density measurements of the round bars obtained via the hydrostatic weighing method.

A marginal density increase is observed in samples cast with 250 mbar added vacuum. However, the incremental rise in vacuum strength to 125 mbar yields minimal improvement. Notably, samples cast with 75 mbar added vacuum demonstrate the highest density of 2.68 g/ml. This heightened density underscores that stronger vacuum conditions result in reduced porosity, as the vacuum facilitates the removal of air from the cavity during filling, thereby minimizing air entrapment. The theoretical density of aluminum is 2.699 g/ml. Even the sample cast under the strongest vacuum shows a density lower than this theoretical value. This difference could be attributed to other types porosity in the sample, such as shrinkage porosity or residual gas porosity. Increasing the intensification pressure or employing a super-vacuum might help achieve a density closer to the theoretical value of 2.7 g/ml. Additionally, due to the error in these results the difference between the values is not that significant. This is also due to the other defects present, like shrinkage porosity, that lowers the density and is not impacted by vacuum.

Effect of Vacuum on Mechanical Properties

The machined tensile bars extracted from the 3 mm thick plates were subjected to tension testing to determine the impact of vacuum on their mechanical properties.

Vacuum Level ($mbar$)	Yield Strength (MPa)	Ultimate Tensile Strength (MPa)	Elongation (%)
1000	78	129	2.0
120	89	179	3.5
75	95	169	2.5

Table 3.5: The mechanical properties of the AlSi7 alloy in the as-cast condition are presented for the three studied vacuum levels.

Each condition was tested with at least three samples to establish average values for these properties. Table 3.5 presents the as-cast mechanical properties for the AlSi7 alloy. The results demonstrate increases in elongation and ultimate tensile strength (UTS) with stronger vacuum levels, with the 75 mbar samples exhibiting the highest elongation and strength. Yield strength (YS) also shows improvement with increased vacuum, consisted with reduced porosity and higher density.

However, both yield strength and elongation remain lower than typical expectations for this alloy, which normally achieves a YS of 130 MPa and 8% elongation in the as-cast state [114]. This suggests the presence of additional defects causing complications. These samples notably exhibit significant shrinkage porosity due to inadequate intensification pressure during solidification. Additionally, there were many Type II Externally Solidified Crystals present in the samples that caused the mechanical properties to decrease.

Effect of Vacuum using CT Scans

Figure 3.20 depicts the result obtained from the CT scan analysis of 3 mm plates machined from cast AlSi9 specimens. A comparison is made between plates from the specimen cast without added vacuum and the specimen cast with 80 mbar added

vacuum. Noticeably, the presence and size of porosity diminishes with the addition of vacuum. Specifically, porosity in the grip of the tensile bar experiences a significant reduction, while porosity in the gauge region remains relatively consistent. However, even in the absence of added vacuum, there is minimal porosity observed in the gauge region, possible attributable to typical casting variations. Furthermore, simulations of the full-size die also reveal residual air within the 3 mm plate. In contrast, simulations of the scaled-down specimen die have less residual air in the 3 mm plate, aligning more closely with findings from the water analog experiments. Discrepancies in porosity predictions may arise from differences in viscosity and surface tension between water and molten aluminum.

The CT scan results for the machined 3 mm plates of cast AlSi7 are depicted in Figure 3.21. Figure 3.21(a) displays the machined 3 mm plate from the casting trial conducted without added vacuum, while Figure 3.21(b) showcases the plate cast with 124 mbar added vacuum. In Figure 3.21(a) extensive porosity is evident throughout the sample, particularly in the grip regions. However, the addition of a 124 mbar vacuum notable reduces porosity in the grip regions. Consequently, there is diminished visible porosity in these areas. Meanwhile, porosity in the gauge region remains relatively consistent. This reduction in porosity within the grip regions aligns with observations from the water analog experiments and simulations.

Table 3.6 displays the average largest pore volumes extracted from the CT scans of the 3mm plates. Pore volumes for three distinct vacuum levels are provided. In castings produced without a vacuum, the largest pore volume measured 108 mm^3, significantly exceeding the largest pore volume observed in samples cast with a 124 mbar vacuum. Specifically, the largest pore volumes for samples cast with 124 mbar

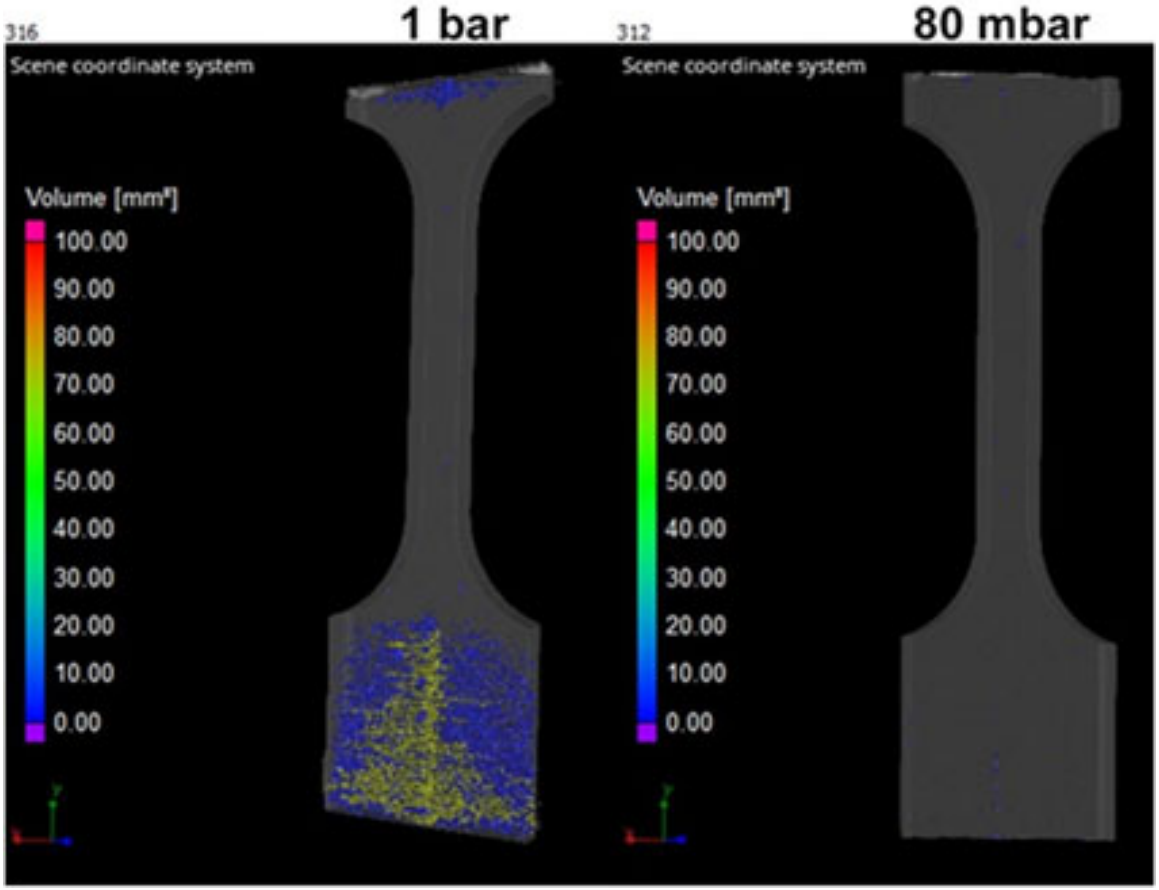

Figure 3.20: The CT scans results depicting the machined 3 mm plate from the AlSi9 casting trial conducted without added vacuum and with an 80 mbar added vacuum.

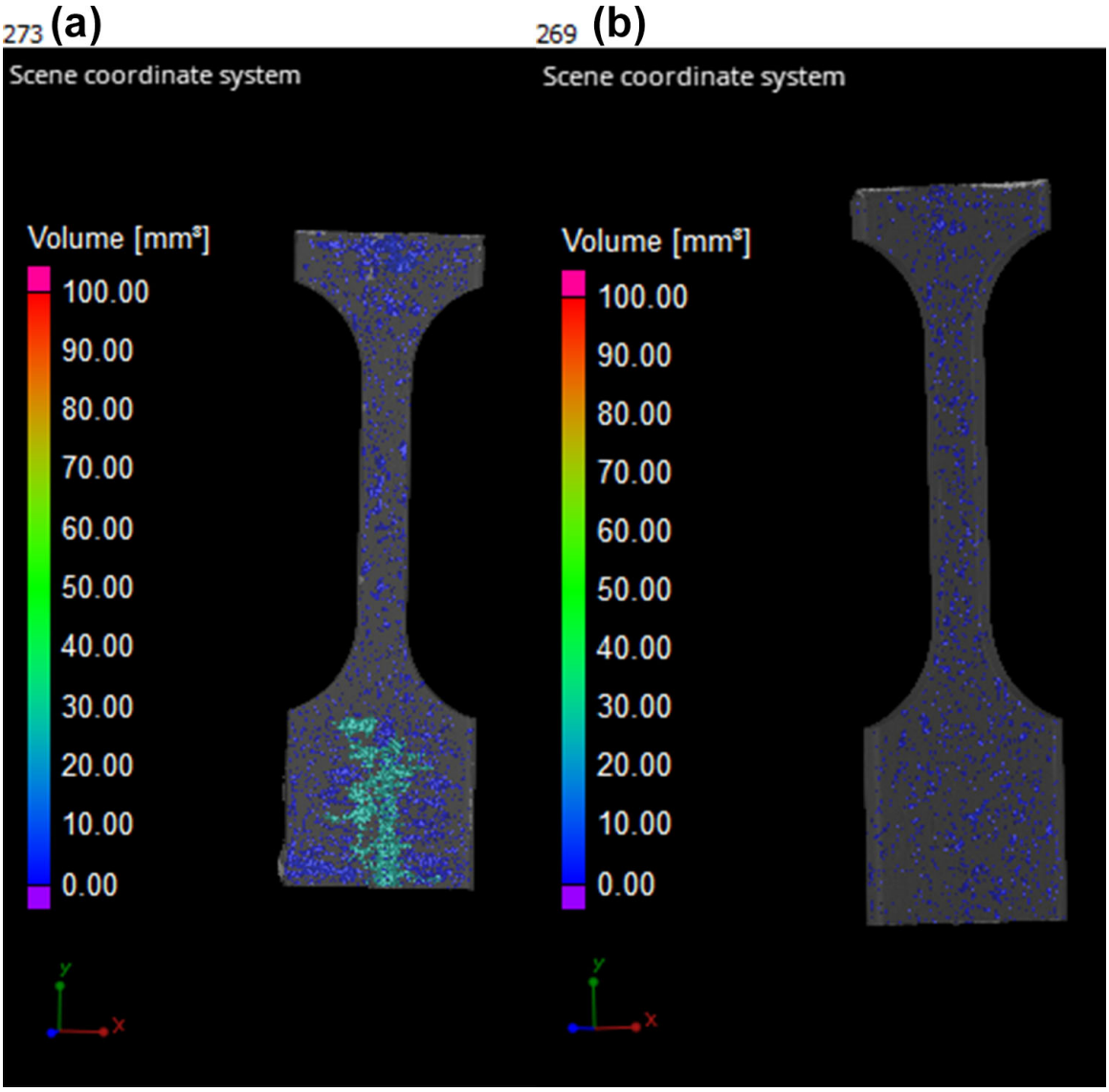

Figure 3.21: The CT scans feature the machined 3 mm plates from the AlSi7 casting trials. (a) corresponds to the plate cast without added vacuum, while (b) corresponds to the plate cast with a 124 mbar added vacuum.

Vacuum Level (mbar)	Largest Pore Volume (mm^3)
1000	108
124	6
80	14

Table 3.6: Average volume of the largest pore identified in the CT-scanned 3mm plates.

added vacuum and with 80 mbar added vacuum were 6 mm^3 and 14 mm^3, respectively. The application of a vacuum reduces the size of the largest pore present in the 3 mm plate, by reducing the amount of air that can be trapped during cavity filling.

3.5 Conclusions

In this study, water analog experiments, computer simulations, and high pressure die casting trials were compared to assess the impact of vacuum on the entrapment of air and gas porosity in die-cast aluminum alloy samples.

Water analog experiments provide a valuable technique for visualizing fluid flow during high pressure die casting, offering insights that are otherwise challenging to observe directly in metal dies during the actual process. Despite slight differences in viscosity and surface tension between water and molten aluminum, these experiments yield valuable data. They demonstrate good repeatability and are relatively straightforward to conduct. Moreover, there is notable agreement between the water analog experiments and computer simulations, particularly regarding the general flow patterns and the impact of vacuum on entrapped air during the injection phase of

HPDC. This convergence suggests that numerical simulation of cavity filling serves as a valuable tool in the development and optimization of the HPDC process.

The employment of vacuum proves effective in diminishing the presence of entrapped air and porosity in die castings, a phenomenon evident in both water analog experiments and simulation air results. Moreover, elevating the vacuum level demonstrates a quantifiable reduction in gas porosity within the castings. This assertion finds support in the CT scan findings of the die cast specimens, where a corresponding decrease in porosity within the 3 mm plate is observed with vacuum levels.

Adding substance such as glycerin to water can alter its viscosity, potentially improving the accuracy of water analog results. Furthermore, conducting additional die casting trials using an upgraded machine with improved control over parameters like shot sleeve temperature, die temperature and intensification pressure could provide deeper insights into the effects of vacuum on casting samples.

Chapter 4: Externally Solidified Crystals in HPDC

This chapter discussed the formation mechanism of externally solidified crystals (ESCs) and methods to reduce their presence in die cast parts. Computer simulations using MAGMASOFT®, ProCAST and FLOW-3D were compared with water analog experiments and die casting trials to investigate shot sleeve solidification and turbulence during filling.

4.1 Introduction

Externally solidified crystals (ESCs) are microstructural heterogeneities that can reduce mechanical properties, particularly elongation. Two types of ESCs are present in the cast microstructures, as depicted in Figure 4.1. Type I ESCs are alpha-Al grains that are larger and coarser than other grains, typically exceeding 15 microns in size [69]. Type II ESCs are significantly larger than Type I ESCs and exhibit a finer structure with a distinct boundary with the matrix. This boundary is a weak point in the microstructure and can serve as a crack initiation site. Type II ESCs begin to solidify next to the boundary, resulting in the finest microstructure near the boundary, which becomes coarser as the distance from the boundary increases [115]. These Type II ESCs are also commonly referred to as cold flakes in the literature [71].

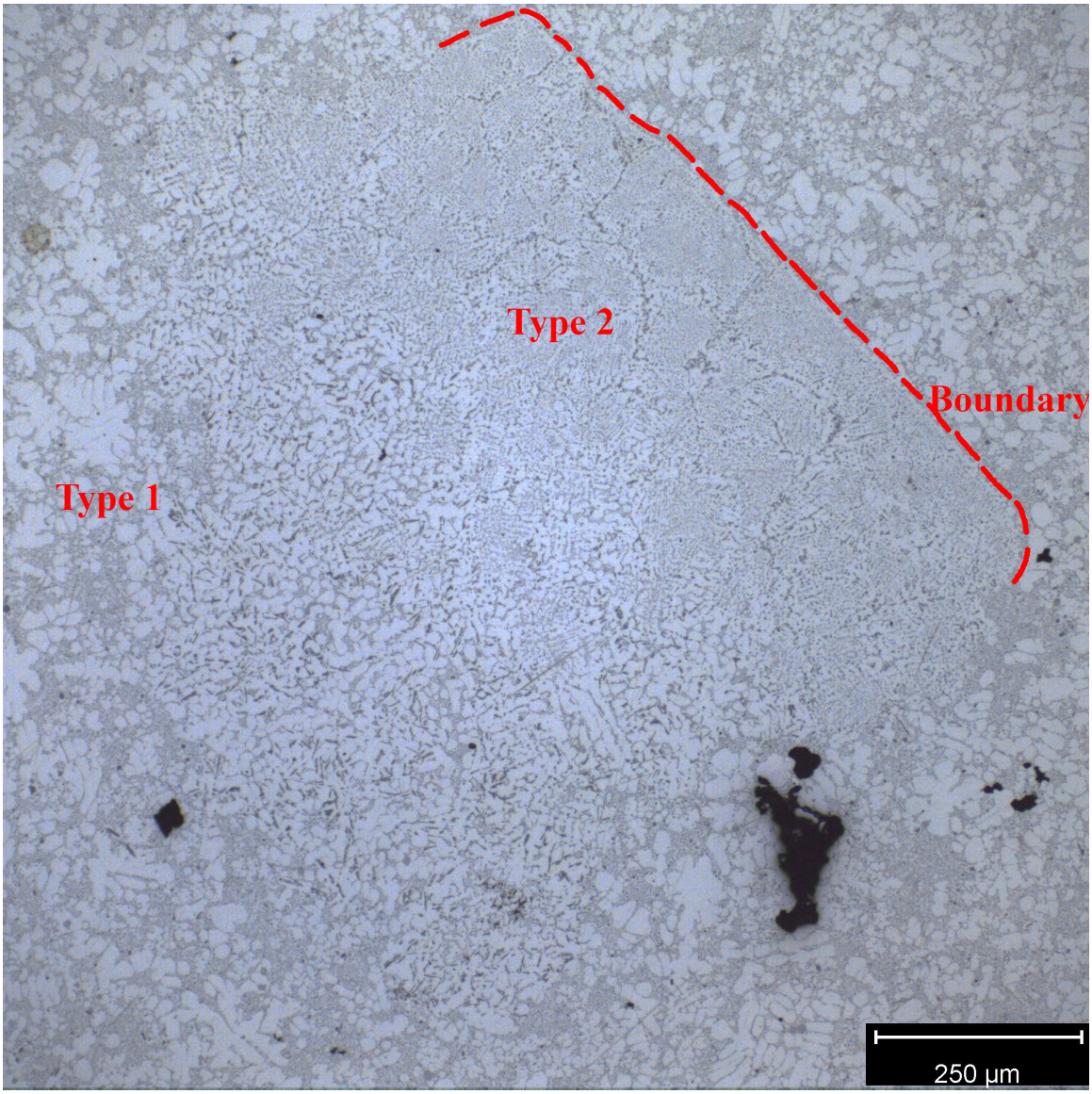

Figure 4.1: An optical image showing the two types of ESCs, with the boundary marked by a red line.

The formation mechanisms of both types of ESCs are poorly understood. It is believed that both types originate in the shot sleeve, but their distinct structures dictate vastly different cooling rates during formation. Type I ESCs, characterized by their coarse structure, necessitate a slower cooling rate, whereas Type II ESCs, with their finer structure, require a much faster cooling rate [116].

Type I ESCs have been investigated across various alloys, such as magnesium alloy AM60B [117], hypereutectic Al-Si alloys [65], and an AlMgSi alloy [118]. Type I ESCs are formed in the shot sleeve prior to injection [118, 116, 70]. Otarawanna et al [70] notes that these ESCs tend to nucleate on the shot sleeve walls or near the plunger tip due to the lower temperatures. However, the cooling rates away from the shot sleeve walls promote the formation of large grains, specifically Type I ESCs [118, 116]. In hypereutectic Al-Si alloys, Type I ESCs are also formed in the shot sleeve and are referred to as "primary silicon particles" [65].

Jiao et al [64] investigated how varying casting parameters affect the size of Type I ESCs, finding that a decrease in the fast shot speed results in an increase in ESC size. They also determined that the speed of the slow shot impacts the quantity of ESCs present [64]. Similarly, Wang and Xiong [119] observed that the size of Type I ESCs increases with longer retention time in the shot sleeve. Additionally, they found that a slower slow shot speeds leads to more ESCs in the casting [56], as the ESCs have more time to grow in the shot sleeve. This finding aligns with the results from the model Bi et al developed [67], which simulates Type I ESC flow during filling, and shows that a faster slow shot speed results in smaller ESCs due to reduced growth time in the shot sleeve.

Dou et al [72] also found that a faster slow shot reduces the number of Type I ESCs in the microstructure. Researchers discovered that delaying the transition to a fast shot significantly increases the number of Type I ESCs compared to an earlier transition point [56]. Wang and Xiong [56] concluded that slow shot speed has a greater effect on ESC formation than fast shot speed. Additionally, they found that a decrease in biscuit thickness leads to larger ESCs due to an increase in the amount of metal in the shot sleeve, which loses heat more slowly and thus experiences less solidification on the walls [119].

Another method to reduce Type I ESCs is increasing the temperature of the molten metal, although this can shorten die life. However, Dou et al [72] found that optimizing the slow shot speed can achieve comparable results.

Die design plays a significant role in influencing the presence of Type I ESCs. Zhou et al [104] implemented an ESC collector positioned in the runner to collect Type I ESCs before their entry into the die cavity. The implementation of the ESC collector resulted in a reduction of ESCs in the casting and improved the mechanical properties of the castings [104]. This highlights that since the ESCs were collected in the runner before entering the cavity, their formation likely occurred in the shot sleeve.

Simulations have been employed to investigate the formation of Type I ESCs. Dou et al [120] utilized the fraction solid ProCAST result to analyze the extent of solidification within the shot sleeve. Their findings indicate that solidification typically occurs near the two ends of the shot sleeve [120]. Meanwhile, Hao et al [121] utilized CA modeling to simulate grain structure with and without Type I ESCs. The investigators discovered that in certain alloys characterized by a narrower solidification

range, ESCs exerted a significant impact on grain size [121]. The solidification range refers to the temperature difference between the solidus and liquidus temperatures.

4.1.1 Type II ESCs

Type II ESCs have received less comprehensive examination compared to Type I. It is believed that they originate on the wall of the shot sleeve [122, 123, 71]. The shot sleeve typically operates at a lower temperature than the molten metal, approximately 300 °C compared to the melt's temperature of around 700 °C. Consequently, when the metal comes into contact with the shot sleeve, it rapidly cools and solidifies. During solidification on the shot sleeve wall, an oxide skin layer forms. This skin layer is partially fragmented and pushed into the casting by turbulence caused by the movement of the plunger [109, 66]. Once injected into the die casting cavity, this oxide layer fails to bond with the matrix, creating a vulnerable point from which cracks may initiate [122]. Due to the rapid cooling rates along the shot sleeve wall, the resulting cold flakes possess a finer microstructure compared to the matrix [115].

Similar to Type I ESCs, casting parameters significantly influence the size and quantity of Type II ESCs in the casting. Wang et al [79] determined that while the ladle did not significantly affect Type II ESCs, the duration of metal settling in the shot sleeve had a substantial impact on their size and number. Other researchers identified that melt temperature had the greatest influence on ESC quantity in the final casting [71]. This is because the metal's superheat affects the solidification process: higher superheat means more heat must be removed before the metal solidifies. Heat can be dissipated through the shot sleeve, causing the metal to solidify within

it and form Type II ESCs. Moreover, the speed of both slow and fast shots can affect Type II ESCs, by inducing turbulence that breaks them into smaller fragments.

This study compared computer simulations, water analog experiments and die casting trials to determine the formation mechanisms of Type I and Type II ESCs. The computer simulations analyzed cooling and turbulence in the shot sleeve during filling. Water analog experiments, with added beads, modeled the flow of Type II ESCs during filling. Die casting trials with various alloys assessed the impact of different casting parameters. Tensile testing of round bars and plates evaluated the effect of Type II ESCs on the mechanical properties. Figure 4.2 shows the hypothesis for how Type I ESCs form in the molten metal in the shot sleeve and Type II ESCs form along the shot sleeve wall.

4.2 Experimental Design

4.2.1 Water Analog Experiments

The experimental setup described in Section 3.2.1 was replicated to investigate the influence of particles on flow dynamics during casting. Acrylic beads were introduced into the shot sleeve to observe the movement of particles during filling. The beads were added to the shot sleeve at two locations. They were poured through the pour hole near the plunger and also placed at the biscuit location near the die cavity. These beads were selected for their density similarity to water. Previous studies modeled ESCs using particles that had the same density as the liquid used during filling [67]. Vacuum was no applied, as both slow and fast filling speeds were tested.

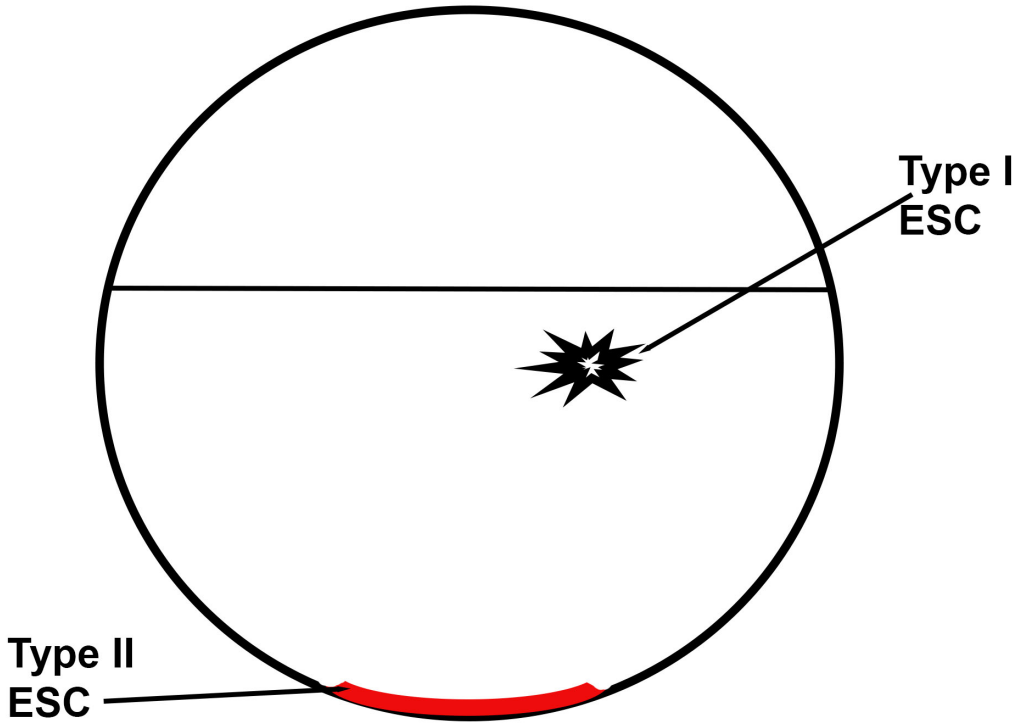

Figure 4.2: An image depicting the formation of Type I and Type II ESCs in the shot sleeve.

4.2.2 HPDC Trials

High pressure die casting trials were conducted at the Center for Design and Manufacturing Excellence (CDME) at OSU using a LK 280-ton Die Casting Machine equipped with a Fondarex vacuum unit (Highvac Economy ‘C-250). Several alloys were cast with variations in melt temperature, shot sleeve temperature, die temperature, fast shot speed, slow shot speed, and alloy liquidus temperature. The average parameters used in these trials are detailed in Table 4.1. Shot speeds typically varied by approximately 3-4 in/s per shot. The intensification pressure during die casting was recorded and typically ranged between 12,000 and 14,000 psi (82 - 96 MPa). The melt underwent degassing using a rotary degassing unit before casting. A total of approximately 1,280 samples were produced during the die casting trials conducted for this investigation.

Temperature measurements of both the shot sleeve and die were performed using a thermal camera capable of reading temperature up to 270 °C. While the plate regions in the die rarely reached this temperature during the trials, the shot sleeve frequently reached and possibly exceeded this temperature. All casting samples were produced under an added vacuum of approximately 40 mbar. Table 4.2 provides the names of the alloys used and their respective liquidus temperatures, determined using Pandat.

The sample cast is the same as depicted in Figure 3.5 in Section 3.2.2, featuring a die with three plates of varying thickness (2 mm, 3 mm, and 5 mm) and a 6 mm diameter round ASTM tensile bar. Some samples were allowed to solidify in the shot sleeve without being injected into the die cavity; these samples are referred to as ”logs”. Additionally, partial shots were made where the plunger was manually moved partway after pouring the metal into the shot sleeve. The logs, biscuit, gate, and the

Alloy	Melt Temperature (°C)	Shot Sleeve Temperature (°C)	Slow Shot Speed (in/s)	Fast Shot Speed (in/s)
NS-2	728	270	12	69
Phase 1	737	270	12	53
A380	692	270	12	65
RS-3	737	270	12	52

Table 4.1: The casting parameters typically employed in the die casting trials.

Alloy	Liquidus Temperature (°C)
NS-2	602
A380	588
Phase 1	601
RS-3	611

Table 4.2: The liquidus temperatures of the alloys utilized in the die casting trials.

sample itself were sectioned and prepared using standard metallographic preparation techniques.

Both the round tensile bars and machined 3 mm and 5 mm plates were tested using an MTS Criterion ™ Model 43 tensile tester. The samples were pulled at a speed of 0.005 mm/s at room temperature. Around 194 samples were tensile tested. For microstructural analysis, the samples were prepared using the standard metallographic preparation and were examined using an OLYMPUS BX3M-LEDR optical microscope. Additionally, selected samples underwent electron microscopy using a Thermo Scientific Apreo SEM equipped with energy dispersive spectroscopy (EDS).

4.3 Simulation Methods

All simulations were performed using the identical full-size die shown in Figure 3.5 of Section 3.2.2.

4.3.1 MAGMASOFT® Simulations

MAGMASOFT® version 5.5.1. was employed to analyze the solidification process in the shot sleeve and the flow dynamics during casting. The simulations utilized the alloys AlSi9MgMn, and AlSi9Cu3 (A380). Melt temperatures were varied to align with the die casting trials, specifically 708 °C, 703 °C, and 729 °C. Various shot speeds were investigated, including slow speeds of 0.3 m/s and fast speeds of 1.78 m/s and 1.3 m/s. A five-second dosing and dwell time were used, with a die temperature of 200 °C. The shot sleeve temperature was varied: 200 °C, 270 °C, and 300 °C were utilized. Additionally, a 100 mbar vacuum was applied. The cavity mesh consisted of 1,314,302 cells, ensuring at least 3 elements in the thinnest regions.

4.3.2 FlOW-3D Simulations

FLOW-3D Cast 2023 R1, a CFD software, was also employed to analyze the casting flow dynamics and the solidification in the shot sleeve. These simulations focused exclusively on the alloy A380. Various parameters such as melt temperatures (728 °C, and 708 °C), shot sleeve temperatures (300 °C, and 200 °C), slow shot speed (0.3 m/s), and fast shot speeds (1.75 m/s, 1.78 m/s, and 2.5 m/s) were investigated in the study. The mesh in the cavity consisted of 6,030,720 cells. A constant die temperature of 200 °C was used.

4.3.3 ProCAST Simulations

ProCAST 18.0 was also used in the comparative analysis with the previous simulations. A consistent slow shot speed of 0.45 m/s was applied across all scenarios. Fast shot speeds of 1 and 3 m/s were tested to assess their impact. Melt temperatures of 650 and 700 °C were simulated, along with a die temperature of 100 °C. The alloy utilized for casting AlSi9. The simulation employed 4,642,551 3D elements, ensuring at least three elements in the thinnest regions of the model.

4.4 Simulation Results

4.4.1 MAGMASOFT® Results

As metal is poured into the shot sleeve, cooling occurs along its walls, intensifying as the filling progresses. Figure 4.3 illustrates the cooling pattern along the shot sleeve wall at a temperature of 200 °C. The initial melt temperature for this simulation was 708 °C, using AlSi9MgMn alloy as the casting fluid, with a slow shot speed of 0.3 m/s and a fast shot speed of 1.78 m/s. The initial melt temperature used was 708 °C. In Figure 4.3, (a) depicts the start of filling, (b) shows 1.29 seconds after the beginning of filling, and (c) displays the end of filling, occurring 1.41 seconds after the start. As the filling progresses, the dark blue region, representing temperatures below the liquidus of the alloy, expands along the shot sleeve wall. Notably, cooling initiates from the bottom of the shot sleeve. By the end of filling process, the majority of the metal in the shot sleeve had cooled below the liquidus temperature. These observations highlight the formation process of Type II ESCs within the shot sleeve.

Figure 4.4 illustrates the cooling pattern along the shot sleeve wall when the shot sleeve temperature 300 °C. The simulation utilized the alloy AlSi9MgMn with an

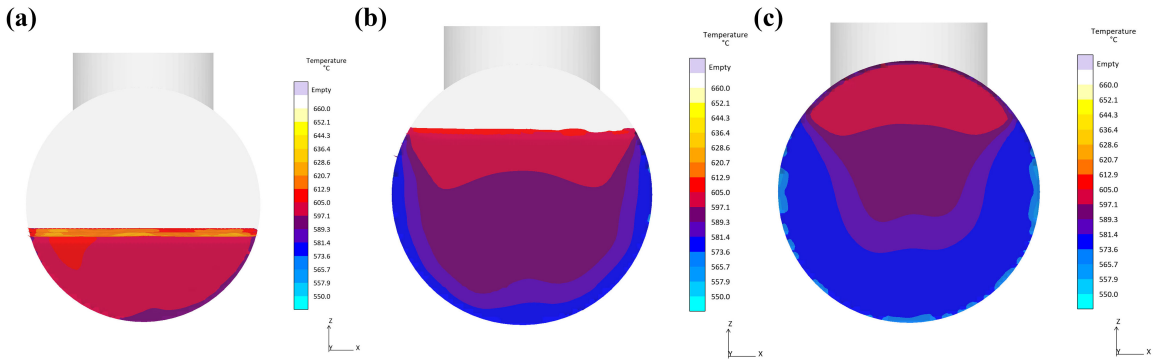

Figure 4.3: The temperature result of the shot sleeve at 200 °C. (a) depicts the initial stage of filling, while (b) represents 1.29 seconds after the start of filling, and (c) shows the end of filling. The initial melt temperature was 708 °C and the alloy used was AlSi9MgMn.

initial melt temperature of 708 °C. A slow shot speed of 0.3 m/s and a fast shot speed of 1.78 m/s were employed in this study. In Figure 4.4(a) shows the beginning of filling, (b) displays 1.29 seconds after the start of filling, and (c) shows the end of filling, occurring 1.41 seconds after the start.

Increasing the shot sleeve temperature results in reduced cooling along its walls. Comparatively, the images exhibit less dark blue coloration, indicating slower cooling with a hotter shot sleeve. The cooling still begins on the bottom of the shot sleeve, but with the hotter shot sleeve, less cooling occurs and there is less metal less than the liquidus temperature at the end of filling. The solidification process within the shot sleeve due to cooling contributed to the formation of Type II ESCs.

The pour temperature of the molten metal significantly influences the extent of solidification within the shot sleeve. Figure 4.5 presents the simulation results from two simulations conducted at different melt temperatures, depicting the cooling pattern along the shot sleeve wall. Both simulations utilized the alloy A380, maintained

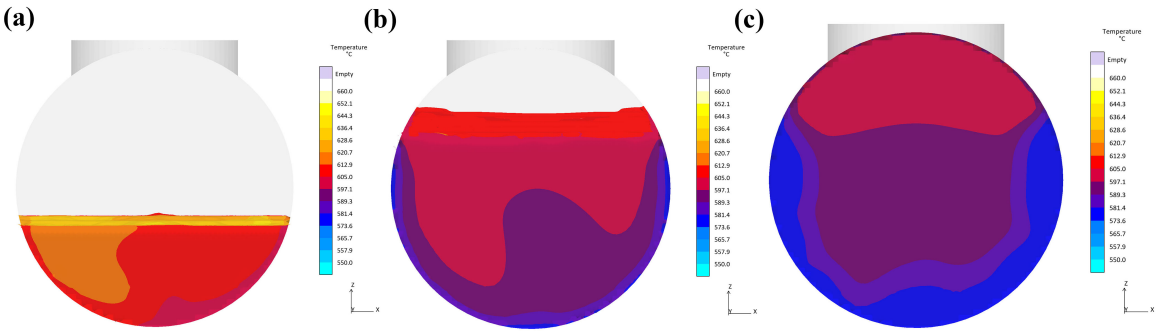

Figure 4.4: The temperature profile of the shot sleeve at 300 °C. (a) depicts the start of filling, (b) shows 1.29 seconds after the start of filling, and (c) displays the end of filling. The initial melt temperature was 708 °C and the alloy used was AlSi9MgMn.

a shot sleeve temperature of 270 °C, and employed identical shot profiles. The slow shot speed was set at 0.3 m/s, and the fast shot speed was 1.3 m/s.

In Figure 4.5(a) and (d) show the beginning of filling, (b) and (e) represent 1.29 seconds after the start of filling, and (c) and (f) display the end of filling. Figure 4.5(a) to (c) correspond to the simulation with a melt temperature of 703 °C, while Figure 4.5(d) to (f) correspond to the simulation with a melt temperature of 729 °C.

The simulation conducted at the lower melt temperature (703 °C) exhibits more pronounced solidification on the shot sleeve wall. As filling progresses, the temperature of the metal decreases along the shot sleeve wall. Towards the end of filling, temperatures as low as 520 °C are observed along the wall in the lower melt temperature simulation, well below the liquidus temperature of A380. In the simulation with a higher melt temperature (729 °C), less cooling is observed in the shot sleeve. Some metal remains above 600 °C at the end of filling. However, both simulations show areas of dark purple color just below the liquidus temperature, indicating that

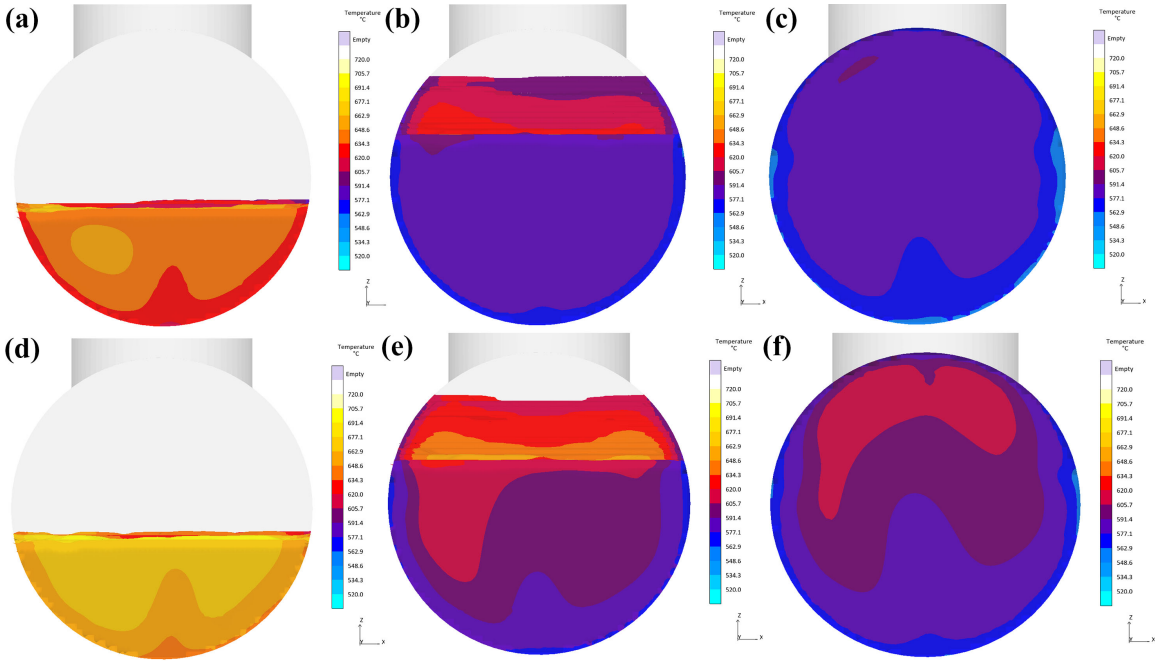

Figure 4.5: The temperature result for the simulations conducted at two different melt temperatures. (a), (b), and (c) depict results from the simulation with a melt temperature of 703 °C. (d), (e), and (f) show results from the simulation with a melt temperature of 729 °C. Both simulations were conducted with a shot sleeve temperature of 270 °C.

some solidification still occurs even with a higher melt temperature. Using a higher melt temperature has drawbacks; at elevated temperatures aluminum can absorb more hydrogen from the atmosphere, potentially leading to hydrogen porosity in the samples.

A lower melt temperature results in increased solidification within the shot sleeve, leading to more ESCs being formed and pushed into the die cavity compared simulations with a higher melt temperature.

The side view of the shot sleeve illustrates where along its length solidification is more likely to occur. However, it should be noted that the side view does not

depict solidification along the bottom of the shot sleeve. Figure 4.6 displays the temperature results from a simulation with a melt temperature of 729 °C, a shot sleeve temperature of 270 °C, a slow shot speed of 0.3 m/s, and a fast shot speed of 1.3 m/s. In Figure 4.6(a) represents the start of filling, where the entire shot sleeve is still hot with minimal cooling visible. Figure 4.6(b) taken at 900 ms after the start of filling, shows initial cooling beginning at the biscuit end of the shot sleeve. This simulation suggests that cooling initiates near the biscuit rather than the plunger end. Figure 4.6(c) captured at 1100 ms after the start of filling, reveals significantly increased cooling at the biscuit end of the plunger and some cooling starting at the plunger end. This view highlights that cooling in the shot sleeve occurs at both ends and along the bottom, as seen in Figure 4.5.

The cooler regions of the shot sleeve, such as near the die cavity, plunger, and along the bottom, are probable sites for Type II ESCs formation due to solidification occurring in these areas. This temperature decrease promotes the formation of a finer microstructure along the boundary edge.

Figure 4.7 presents the side view of the temperature profile of the shot sleeve from a simulation conducted with a melt temperature of 703 °C, a shot sleeve temperature of 270 °C, a slow shot speed of 0.3 m/s, and a fast shot speed of 1.3 m/s. Figure 4.7(a) depicts the start of filling, where minimal cooling is observed in the shot sleeve. Figure 4.7(b) captured at 900 ms after the start of filling, shows some cooling, particularly more noticeable on the biscuit side compared to the plunger side due to the lower melt temperature. However, there is some cooling at the plunger side, which is characteristic of the lower melt temperature leading to overall cooler temperatures and increased solidification in the shot sleeve.

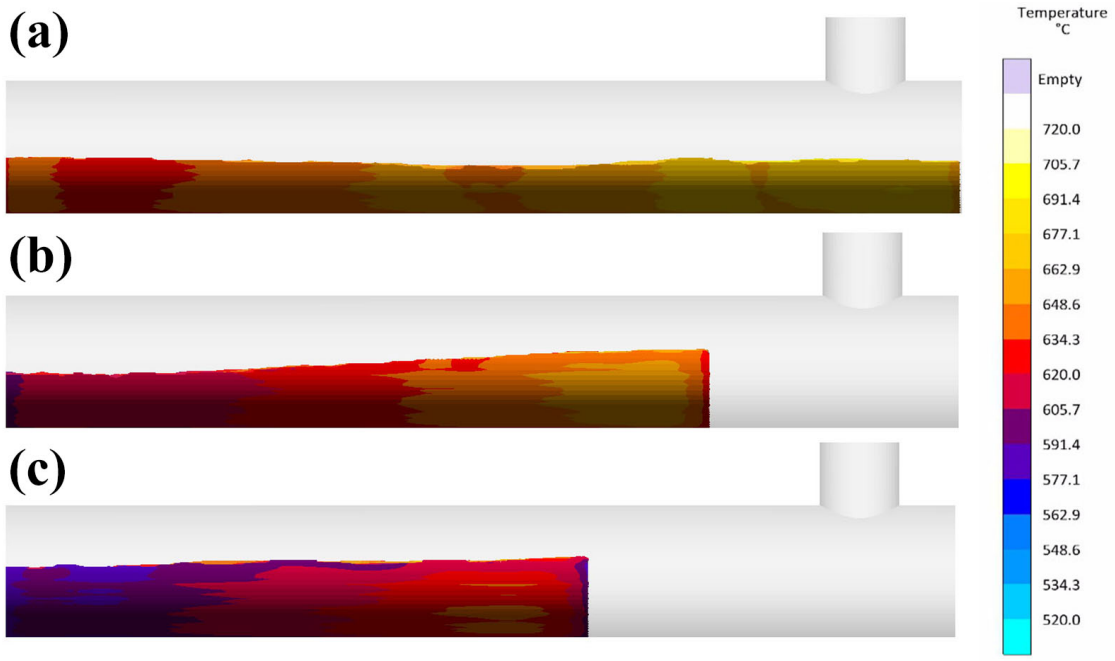

Figure 4.6: The temperature profile of the shot sleeve from the simulation conducted with a melt temperature of 729 °C and a shot sleeve temperature of 270 °C. (a) depicts the start of filling, (b) shows the situation at 900 ms after the start of filling, and (c) represents the condition at 1100 ms after the start of filling.

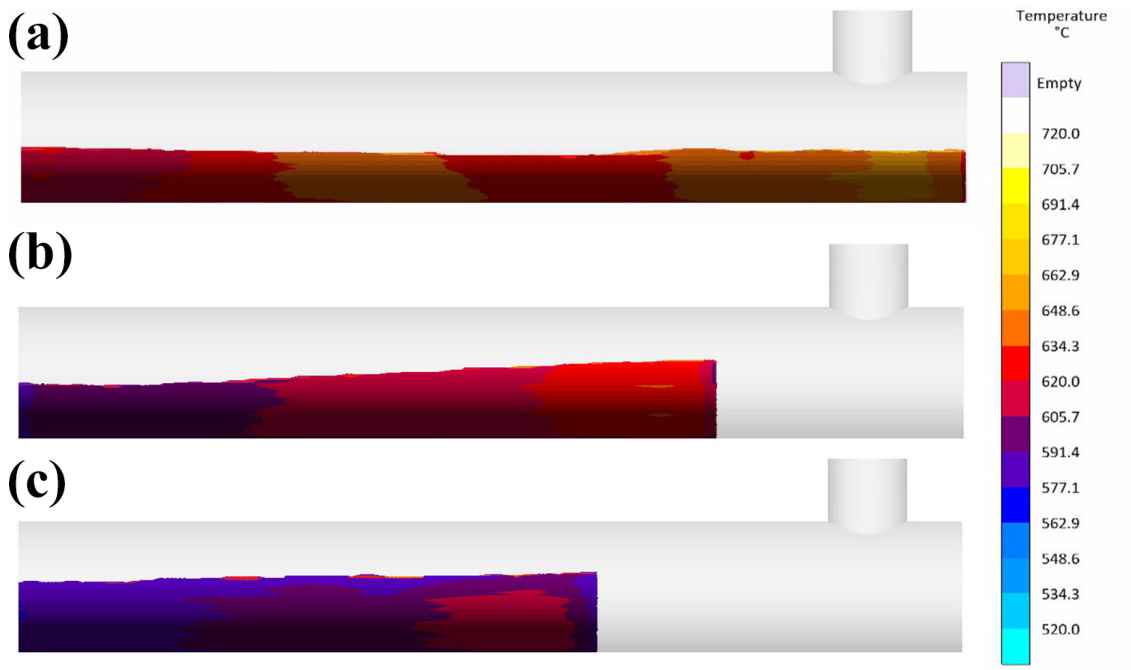

Figure 4.7: The temperature profile along the side view of the shot sleeve during the simulation with a melt temperature of 703 °C and a shot sleeve temperature of 270 °C. (a) corresponds to the beginning of filling, (b) shows the situation at 900 ms after the start of filling, and (c) depicts the condition at 1100 ms after the start of filling.

Figure 4.7(c) at 1100 ms after the start of filling, reveals significantly more cooling. The metal near the die cavity end of the shot sleeve is predominantly cool and below the liquidus temperature of A380 (588 °C). In contrast, the metal closer to the plunger remains hotter, with some portions still above the liquidus temperature. The cooling and potential solidification occur more rapidly with a lower melt temperature. Therefore, using a lower melt temperature would increase the amount of ESCs formed in the shot sleeve due to enhanced solidification.

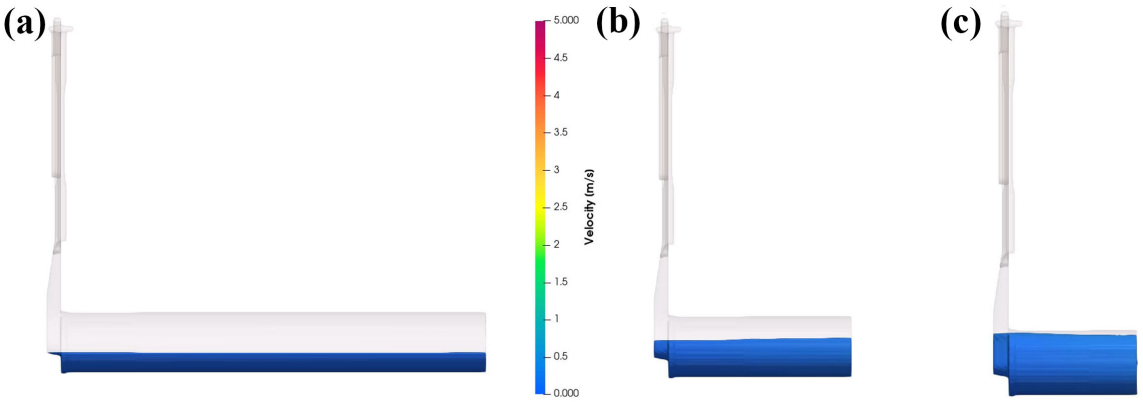

Figure 4.8: The velocity profiles from a simulation with a slow shot speed of 0.3 m/s and a fast shot speed of 1.75 m/s. (a) represents the flow at the beginning of filling, (b) shows the simulation at 2.2 seconds after the start of filling, and (c) depicts the simulation close to the end of filling at 2.4 seconds after the start.

4.4.2 FLOW-3D Results

Figure 4.8 presents the velocity results from a simulation with a melt temperature of 728 °C, a shot sleeve temperature of 300 °C, a slow shot speed of 0.3 m/s, and a fast shot speed of 1.75 m/s. Figure 4.8(a), taken at the beginning of filling when the plunger is just starting to move, shows the initial stage of metal flow. In Figure 4.8(b), captured during the middle of filling at 2.2 seconds after the start, the metal is seen moving towards the casting with minimal predicted turbulence and no wave forming. Figure 4.8(c), near the end of filling at 2.4 seconds after the start, depicts the metal about to enter the die cavity without any turbulence in the shot sleeve. The metal is smoothly pushed into the die cavity without forming a wave, which is beneficial for reducing defects; however, this outcome is unexpected. The absence of turbulence in the shot sleeve implies that ESCs are broken up through an alternative mechanism.

The temperature profiles were analyzed to observe cooling along the shot sleeve wall. Figure 4.9 illustrates the front of the shot sleeve for a simulation with a shot sleeve temperature of 300 °C, a melt temperature of 708 °C, a slow shot speed of 0.3 m/s, and a fast shot speed of 2.5 m/s. Figure 4.9(a) the initial state of the simulation where the metal is at the melt temperature, with no visible cooling along the sides of the shot sleeve. In Figure 4.9(b), taken 0.77 seconds after the start of plunger movement, all of the liquid metal in the shot sleeve appears to be uniformly cooled, without a visible temperature gradient, which is not typical. The cooler shot sleeve is expected facilitate cooling closer to the walls, while the center of the melt remains hotter.

Figure 4.9(c), captured at 2.47 seconds after the start of plunger movement as the metal begins to fill the die cavity, shows hotter metal along the shot sleeve wall and cooler metal near the center. This observation contradicts expectations and conflicts with the result from MAGMASOFT® simulations. One possible explanation could be the viewing angle: the hotter metal at the edges might be from the center of the shot sleeve being pushed outward during plunger movement. The metal filling the die cavity is hot, so the cooler metal near the plunger may obscure the view of the hotter metal in front of it.

These unexpected results diverge from other simulation findings and existing literature, suggesting potential discrepancies that warrant further investigation.

The side view of the shot sleeve was also examined to observe solidification at both ends. Figure 4.10 presents the temperature results from a simulation using a melt temperature of 708 °C, a shot sleeve temperature of 200 °C, a slow shot speed of 0.3 m/s, and a fast shot speed of 1.78 m/s. Figure 4.10(a), taken at the start of plunger

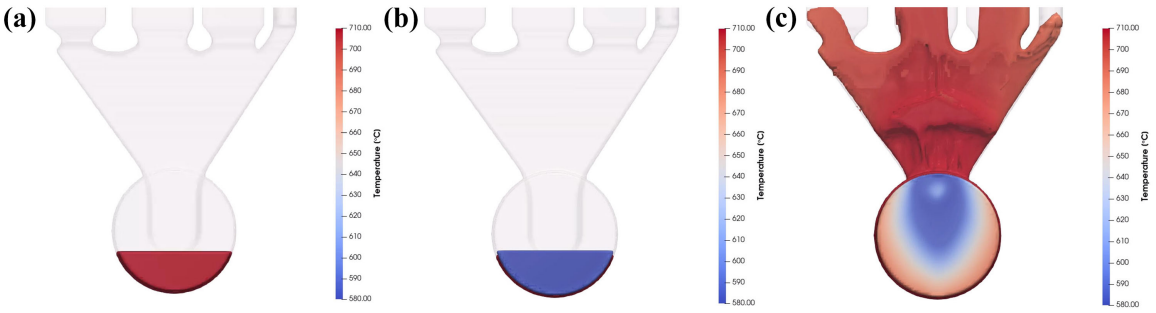

Figure 4.9: The temperature result from a simulation with a shot sleeve temperature of 300 °C and a melt temperature of 708 °C. (a) show the temperature profile at the start of the simulation, (b) depicts the situation at 0.77 seconds after the start, and (c) illustrates the conditions at 2.47 seconds after the start of the simulation.

movement, shows initial cooling near the plunger. In Figure 4.10(b), captured 1.6 seconds after the start of filling, more pronounced cooling is evident at the plunger end, as well as noticeable cooling in the biscuit and runner areas. By the end of filling, shown in Figure 4.10(c), solidification near the plunger is more prominent, with the shot sleeve fully filled and some cooling observed along the top. Cooling along the top of the shot sleeve could also be a location for Type II ESC formation. The top of the shot sleeve has less contact with hot metal, resulting in cooler temperatures compared to the bottom and sides. This cooler temperature promotes nucleation of a finer microstructure. Additionally, the cooling metal in the biscuit area has been pushed into the die cavity, demonstrating how some ESCs enter the the die cavity.

The cooling pattern observed in the shot sleeve corresponds to findings from MAGMASOFT® simulations (see Figure 4.7 and Figure 4.6), which also demonstrate substantial cooling. However, there are discrepancies in the cooling location between these results. MAGMASOFT® indicates initial cooling at the biscuit end,

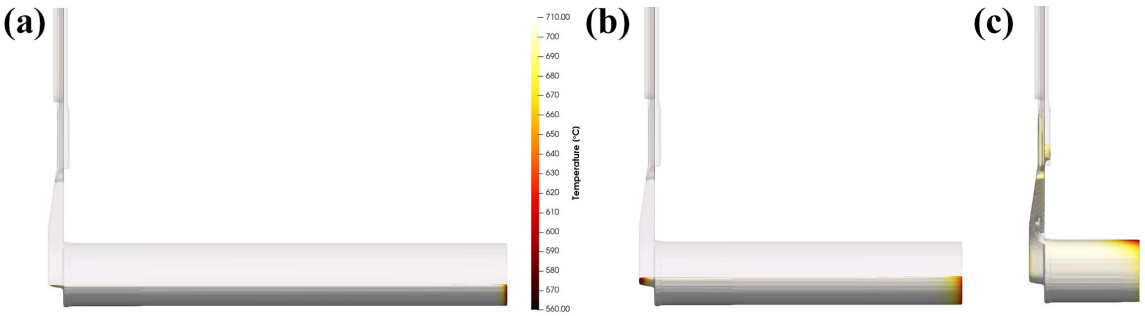

Figure 4.10: The temperature results for a simulation with a melt temperature of 708 °C and a shot sleeve temperature of 200 °C are shown. (a) is from the start of plunger movement, (b) is from 1.6 seconds after the start of filling, and (c) is from 2.4 seconds after the start of filling, close to the end of filling.

with cooling at the plunger end occurring later in the simulation. In contrast, FLOW-3D shows more cooling near the plunger and minimal cooling near the runner. This variation may result in differences when predicting the occurrence of Type II ESCs in different regions of the shot sleeve. Both ends of the shot sleeve exhibit lower temperatures, aligning with expectations from the simulation outcomes. Future studies investigating the influence of die temperature and plunger temperature on ESC formation could offer deeper insights into the specific locations where Type II ESCs are prone to form.

4.4.3 ProCAST Results

Figure 4.11 presents the temperature results for a simulation with a fast shot speed of 3 m/s and a melt temperature of 700 °C. In Figure 4.11(a), taken at the start of filling before the plunger begins moving, some turbulence is visible in the shot sleeve. Figure 4.11(b), captured 0.1 seconds after the start, shows a wave forming

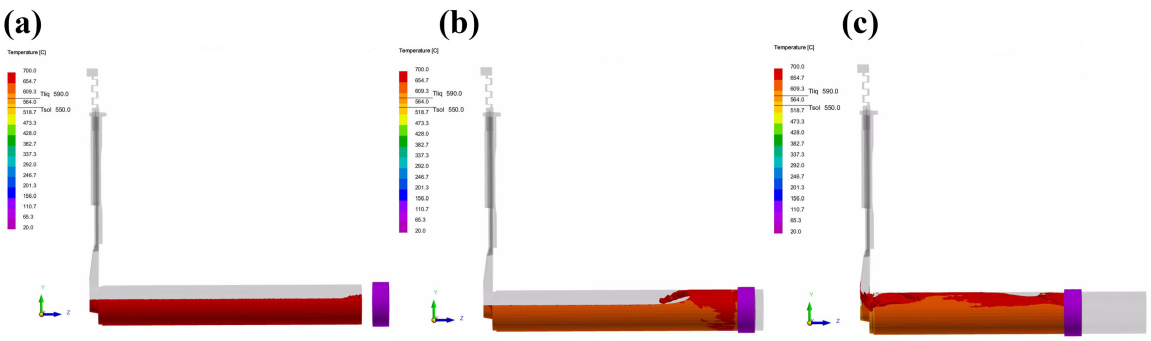

Figure 4.11: The temperature results for a simulation with a fast shot speed of 3 m/s and a melt temperature of 700 °C are shown. (a) is from the start of the simulation, (b) is from the middle of filling, 0.1 seconds after the start, and (c) is from the near the end of filling, 0.2 seconds after the start.

in the shot sleeve and curling over. Figure 4.11(c), from 0.2 seconds after the start and near the end of filling, illustrates the metal about to enter the die cavity with significant turbulence. These results indicate that wave formation in the shot sleeve, leads to turbulence, which can entrap air and break up ESCs. These findings contrast with the FLOW-3D results shown in Figure 4.8, likely due to differences in the turbulence models used by each software. The occurrence of a wave in the shot sleeve is extensively documented in the literature [86] and is typically considered undesirable. The wave can crash and trap air in the shot sleeve, potentially breaking apart Type II ESCs before they enter the die cavity.

Furthermore, Figure 4.11 depicts cooling occurring within the shot sleeve. Figure 4.11(a) shows the start of filling before the plunger begins to move, with all visible metal still at the pouring temperature. In Figure 4.11(b), cooling appears to initiate at the biscuit end and extends through most of the shot sleeve, with some cooling also observed at the plunger end. The hottest metal is found in the wave

and near the plunger. In Figure 4.11(c), the metal near the die cavity begins to drop below the liquidus temperature. These findings align with the results obtained from the MAGMASOFT® simulations, particularly Figures 4.7 and 4.6, which similarly indicated more pronounced cooling at the biscuit end of the shot sleeve.

4.5 Experimental Results and Discussion

4.5.1 Water Analog Experiment Results

As established in Section 3.4.1, the water analog results demonstrated good repeatability. In this study, the application of water analog experiments was extended to model some aspects of solidification in the shot sleeve. Figure 4.12 illustrates the placement of beads within the shot sleeve. These beads were strategically positioned closer to the die cavity to ensure their movement into the cavity during the filling process. Conversely, beads located nearer to the plunger did not enter the cavity and remained within the shot sleeve and biscuit region. This observation aligns with the temperature results from both the MAGMASOFT® and ProCAST simulations. The relatively cooler die cavity, typically around 200 °C, would promote solidification.

Figure 4.13 displays the results of the water analog experiments with the beads added. Figure 4.13(a) represents the beginning of filling, (b) the middle, and (c) the end. The slow shot speed was 0.3 m/s, while the fast shot speed was 1.3 m/s. In Figure 4.13(a), the beads are located in the gate region of both the 5 mm and 2 mm plates. By Figure 4.13(b), the beads have moved past the gate and are filling the 5 mm plate, while also beginning to enter the 3 mm plate and the round bar. At the end of the filling process, shown in Figure 4.13(c), the beads have reached the top of the 5 mm plate but remain in the gate of the 2 mm and 3 mm plates.

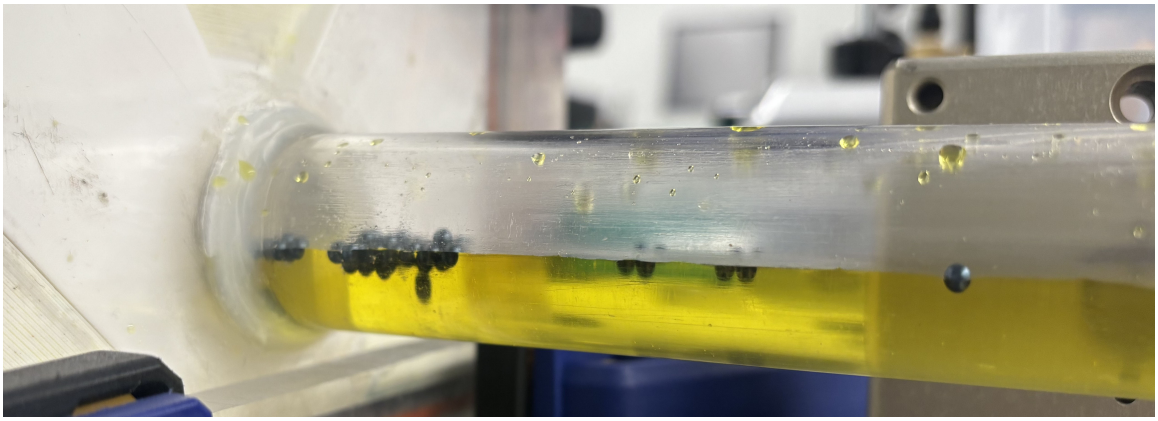

Figure 4.12: The beads in the shot sleeve before plunger movement starts.

This distribution could be attributed to the relative size of the beads compared to the thickness of the plates. The predominance of beads entering the 5 mm plate is expected, as it is centrally located in the die cavity, allowing a direct flow from the shot sleeve. This is corroborated in Section 3.4.1, where the 5 mm plate was the first to fill. Additionally, the presences of one bead in the round bar suggests that some ESCs might flow into this region as well. Using smaller beads might potentially enable them to flow through the 2 mm and 3 mm plates as well.

4.5.2 Microstructure of the Biscuits

Figure 4.14(a) depicts a biscuit from the A380 trial conducted at a fast shot speed of 65 in/s. During tensile testing of the round bar, a Type II ESC was observed on the fracture surface. Optical microscope images in Figure 4.14(b) and (c) show Type II ESCs within the biscuit. Figure 4.14(c) is a magnified view of the region shown in (b), clearly showing the ESC boundary in both images. The lower part of the images shows the ESC region, where a finer microstructure is evident. The microstructure

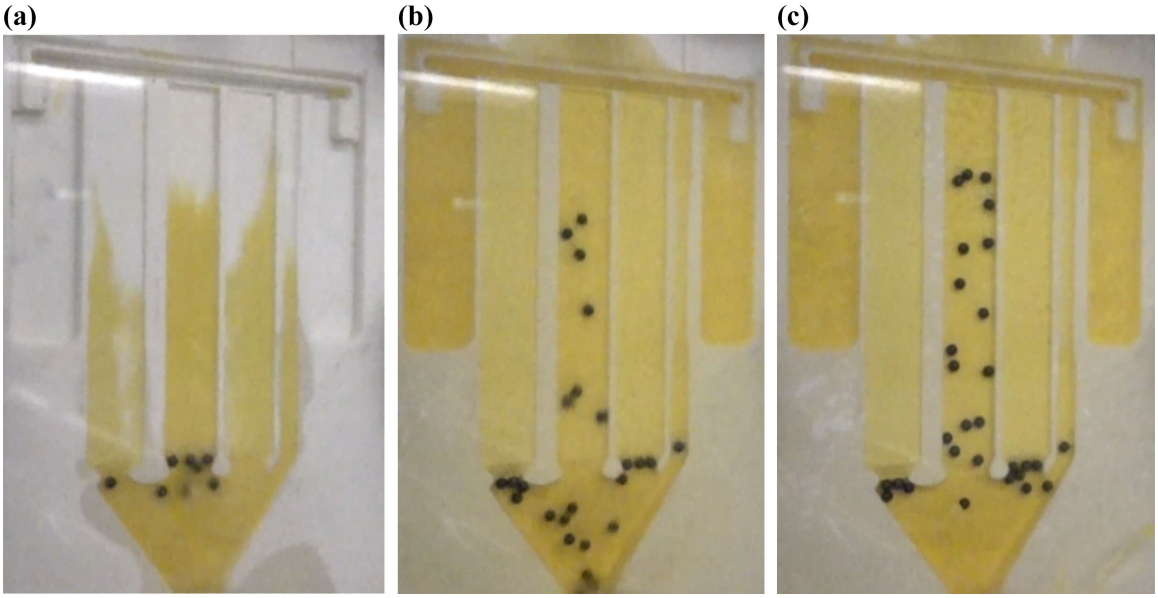

Figure 4.13: The water analog results with beads added: (a) depicts the start of filling, (b) shows the middle stage of filling, and (c) is from the end of filling.

near the boundary appears finer and coarsens further away from it. The presence of Type II ESCs in the biscuit indicates that ESCs form in the shot sleeve and are broken up by the turbulence during filling, pushing them towards the center of the melt. The cooler shot sleeve wall imitates solidification, forming a boundary layer where subsequent metal solidification results in a finer microstructure. Metal farther from the boundary coarsens due to slower cooling rates away from the wall.

4.5.3 EDS Analysis of the 5mm Plate

After conducting water analog experiments, SEM analysis was performed on the 5 mm plates. Figure 4.15 presents the SEM image and EDS maps of the top region of the A380 5 mm plate. This sample was cast with a melt temperature of 694 °C, a slow shot speed of 0.28 m/s, and a fast shot speed of 1.65 m/s. In Figure 4.15(a), a Type II

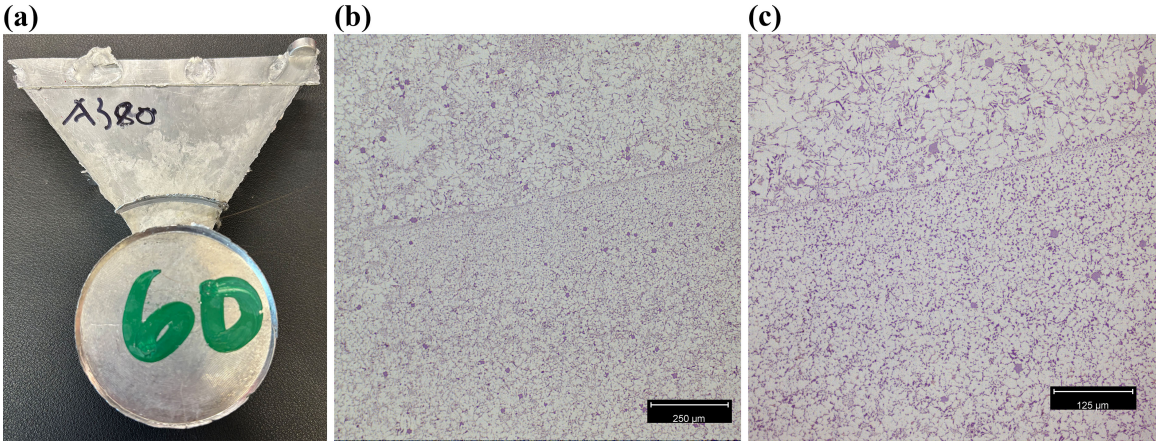

Figure 4.14: A sample from the A380 trial. (a) is an image of the biscuit, while (b) and (c) are optical microscope images of the biscuit showing Type II ESCs.

ESC is visible on the right side of the SEM back-scattered image. Figure 4.15(b)-(d) depict results from the EDS maps.

Figure 4.15(b) shows the aluminum map, illustrating significant microstructural differences between the Type II ESC and the matrix. The ESC exhibits a finer microstructure with smaller dendrites compared to the matrix. Figure 4.15(c) presents the silicon EDS map, revealing finer silicon distribution in the ESC compared to the matrix, indicating that the ESC cooled at a faster cooling rate. Figure 4.15(d) displays the copper EDS map, showing less copper in the boundary region relative to both the matrix and ESC. This observation suggests that copper phases may not nucleate initially on the shot sleeve wall, contributing to their reduced presence in the boundary region.

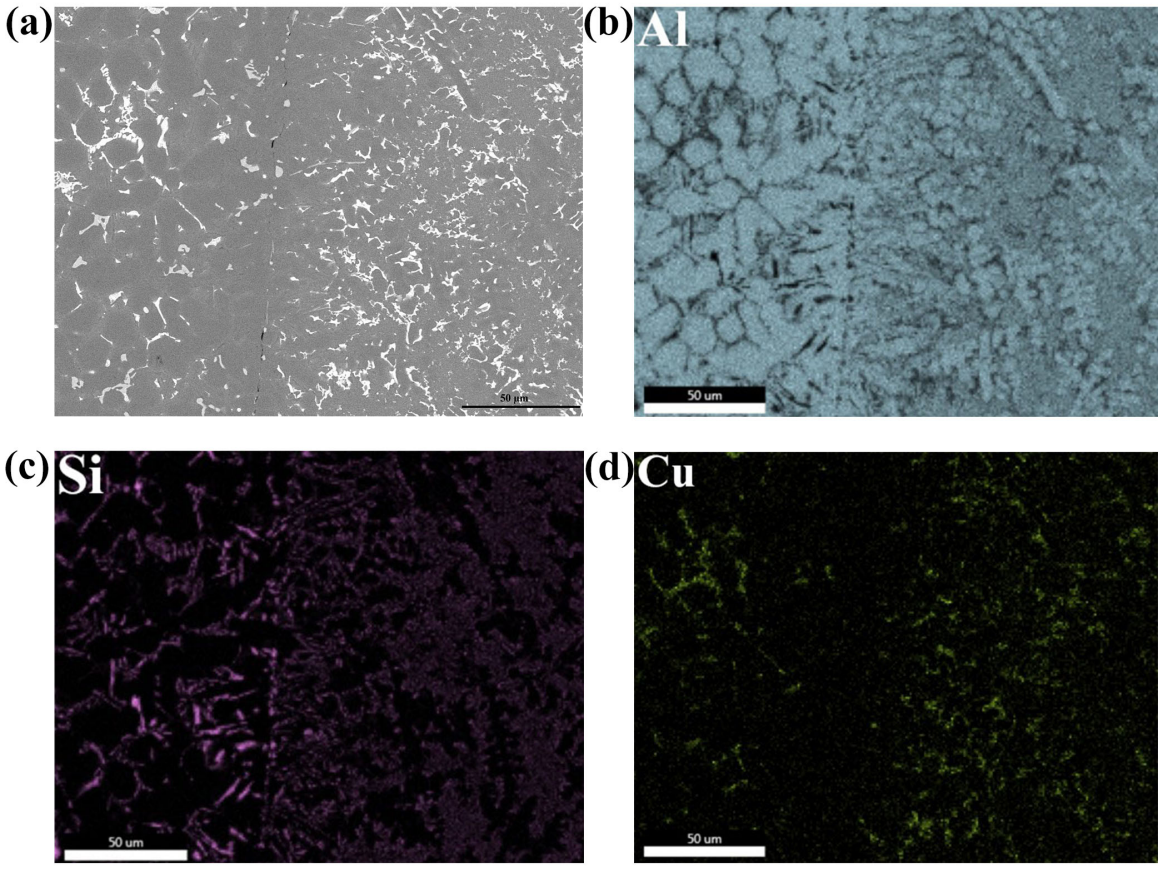

Figure 4.15: The SEM and EDS map of the top of a 5 mm plate from the A380 trial. (a) is the SEM image of a Type II ESC. (b) is the Al EDS map, (c) is the Si EDS map, and (d) is the Cu EDS map.

4.5.4 Microstructure of the Logs

Figure 4.16(a) displays half of the log from the NS-2 alloy trial, cast at the trial's conclusion. The bump at the top left of the log image is due to the pouring of the metal into the shot sleeve, as the bubble is located at the pour hole. This hollow bubble that was commonly observed in most of the logs produced. Figure 4.16(b) presents the microstructure from the bottom of the log at the plunger end, while Figure 4.16(c) offers a more zoom-in view. The microstructure near the wall is much finer compared to the areas further away. suggesting that the cooler wall promoted solidification, leading to the formation of Type II ESCs. The boundary layer would be at the bottom of this image, along the wall. These findings are consistent with the simulation results in Figures 4.3 and 4.4 which showed the metal cooling at the bottom of the shot sleeve. The cooler metal would solidify, forming the Type II ESCs. This finer microstructure is then pushed into the die cavity during filling, leading to Type II ESCs in the biscuit like in Figure 4.14.

Figure 4.17 presents the SEM results from same sample shown in Figure 4.16. The bottom of the images corresponds to the wall of the shot sleeve. The EDS maps clearly reveal finer microstructure closer to the wall. In Figure 4.17(b), the aluminum EDS map shows finer aluminum dendrites near the wall, which coarsen as they move away from it. Similarly, in Figure 4.17(c), the silicon map also has finer microstructure nearer to the wall. These images suggest a faster cooling rate along the wall, promoting a finer microstructure. The fast cooling rate encourages nucleation, but restricts grain growth. Type II ESCs tend to form on the wall, with a fast cooling rate, while Type I ESCs form further away from the wall. Near the top of Figure 4.17(b), a Type I ESC can be observed, indicating larger dendrites that

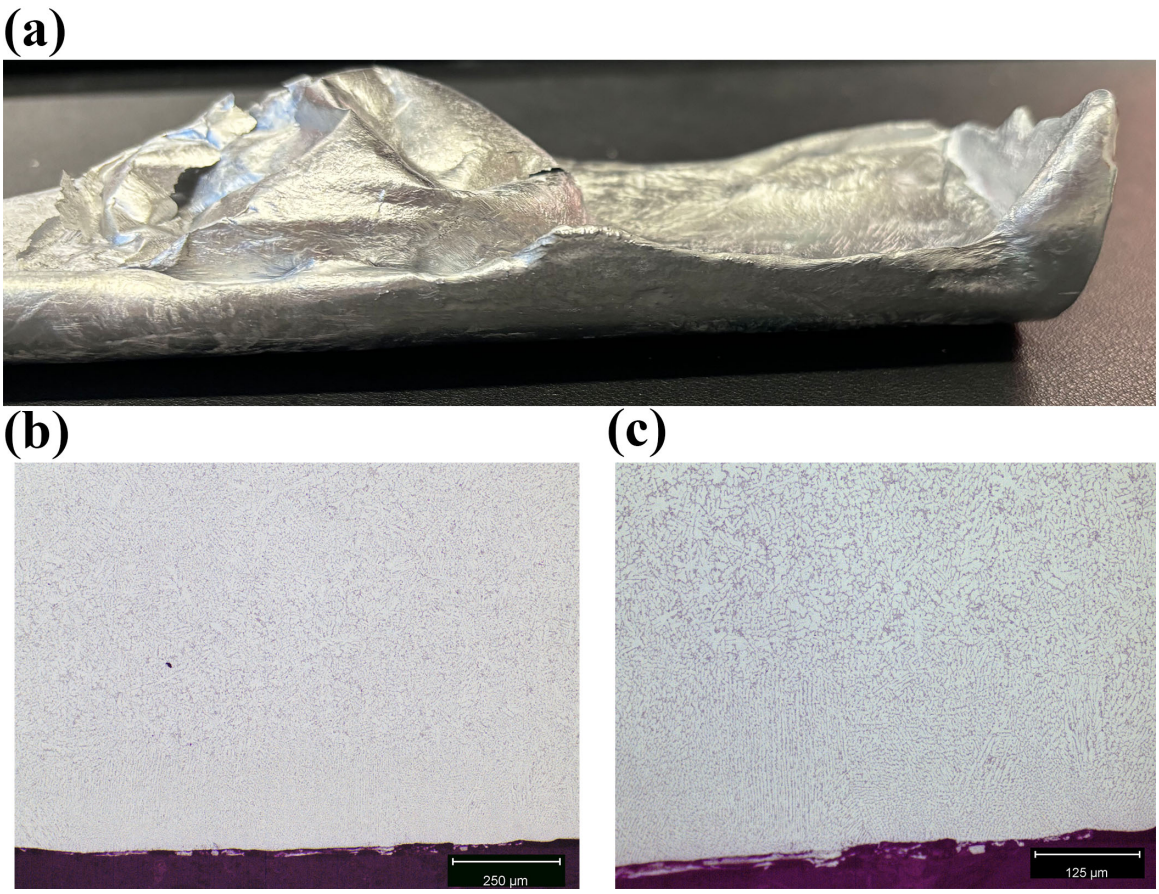

Figure 4.16: The log from the NS-2 alloy trial is shown. (a) is a picture of the plunger side of the log, (b) shows the microstructure along the bottom edge of the log, and (c) provides a zoomed-in view of the microstructure along the bottom edge of the log.

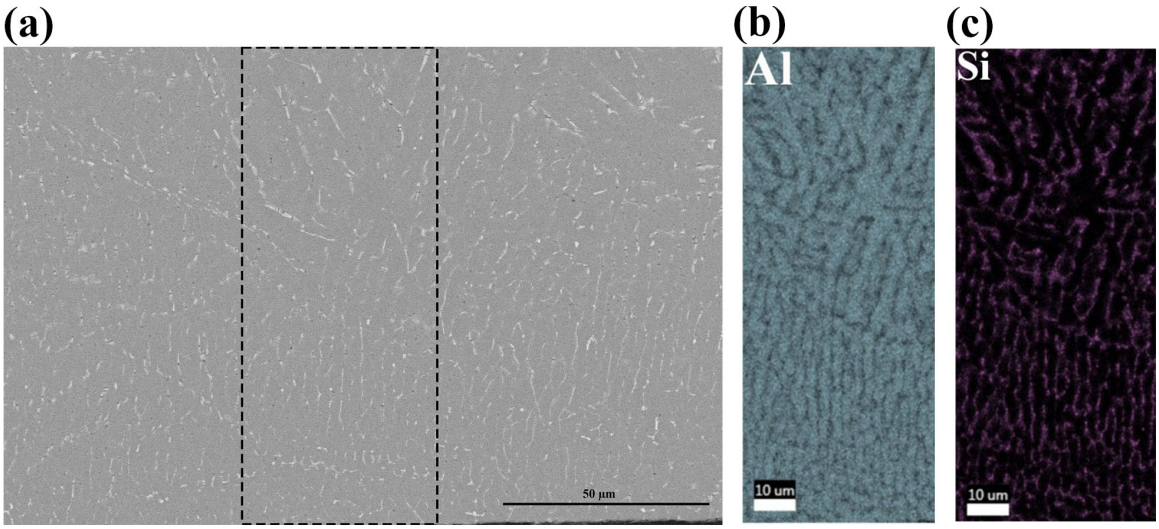

Figure 4.17: The SEM image and EDS maps of the bottom of a log from the NS-2 alloy trial. (a) is the SEM image of the bottom of the log, (b) is the Al EDS map of the area within the rectangle in (a), and (c) is the Si EDS map of the same area within the rectangle in (a).

are more likely to form at slower cooling rates away from the wall. Slower cooling allows dendrites more time to grow, resulting in much larger sizes compared to faster cooling rates. These findings are consistent with the simulations results depicted in Figures 4.3 and 4.4.

Additional images were captured further away from the shot sleeve wall. Figure 4.18 shows an SEM image and EDS maps of the microstructure from further away from the wall. In Figure 4.18(a), a secondary electron image shows larger grains compared to those in Figure 4.17. Figure 4.18(b) shows the aluminum EDS map of the area within the rectangle in (a), highlighting large aluminum grains. Figure 4.18(c) displays the silicon EDS map, where the silicon appears coarser than those in Figure 4.17(c).

These figures indicate that further away from the shot sleeve wall, the cooling rate slows significantly. Type I ESCs are therefore more likely to form away from the shot sleeve wall in the liquid metal. Typically, during a casting trial, this metal would be pushed into the die cavity where it would solidify. However, some Type I ESCs may solidify in the shot sleeve and subsequently by pushed into the die cavity.

4.5.5 Microstructure of Partial Shots

Figure 4.19 depicts the partial shot log from the RS-3 alloy trial. This log was cast at the end of the trial by pouring the metal into the shot sleeve and manually pushing in the plunger partway. In Figure 4.19(a), the entire partial log is shown, with the plunger side on the left where the turbulence during filling is evident. Although this turbulence is expected during filling, it contradicts the simulation results shown in Figure 4.8. However, turbulence is observed in Figure 4.11, suggesting that ProCAST provides a more accurate solver. The turbulence in the shot sleeve contributes to the breakup of the Type II ESCs.

Figure 4.19(b) presents an optical microscope image from the bottom of the log, revealing a finer microstructure closer to the wall of the shot sleeve. In contrast, Figure 4.19(c) also captures an image from the bottom of the log but shows a much coarser microstructure along the wall. The shot sleeve, although cooler than the molten metal, does not maintain uniform cooling, resulting om varying solidification patterns along the wall. Therefore, Type II ESCs are not formed uniformly across the shot sleeve wall; they occur primarily in cooler regions where fast cooling rates can be achieved.

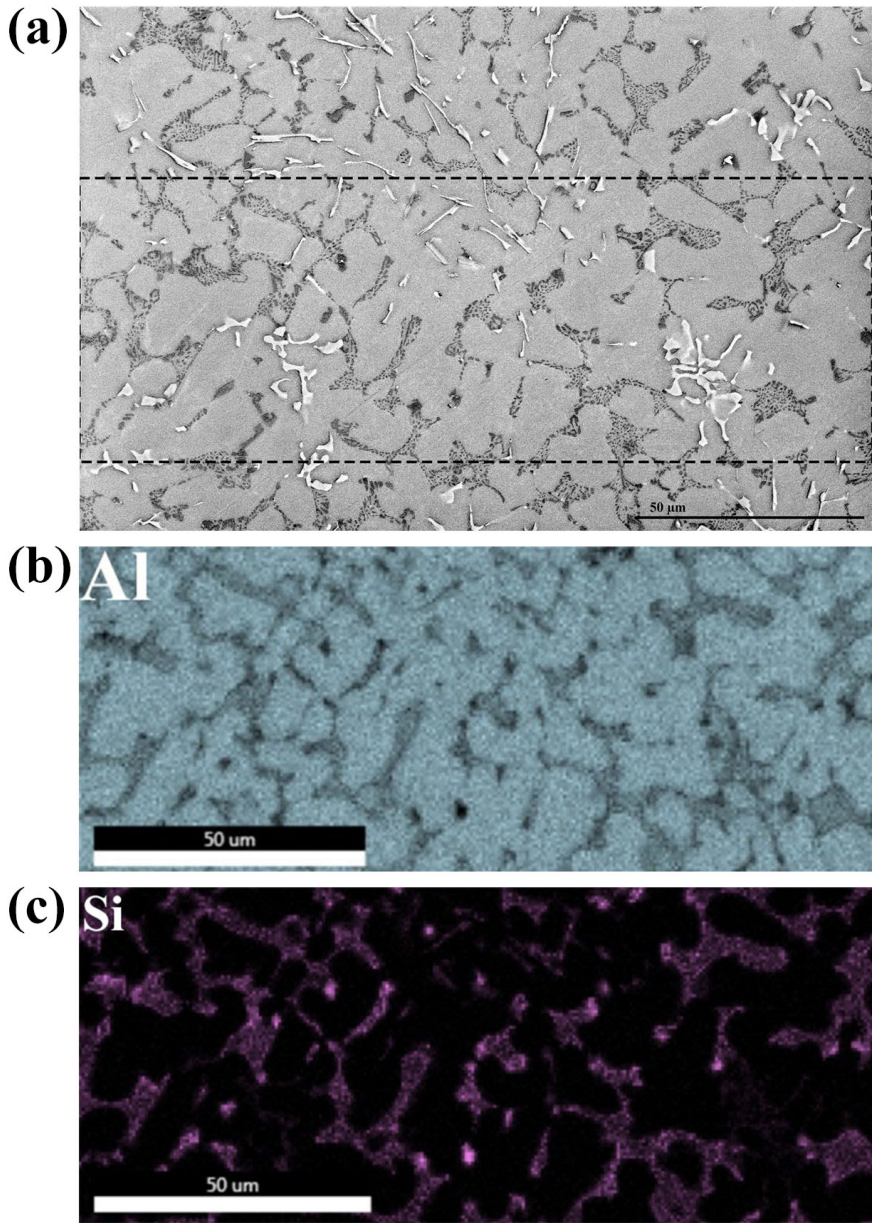

Figure 4.18: The SEM image and EDS maps depict the middle section of a log from the NS-2 alloy trial. (a) shows the secondary electron image of the log. (b) displays the Al EDS map of the area inside the rectangle, and (c) shows the Si EDS map of the same area within the rectangle in (a).

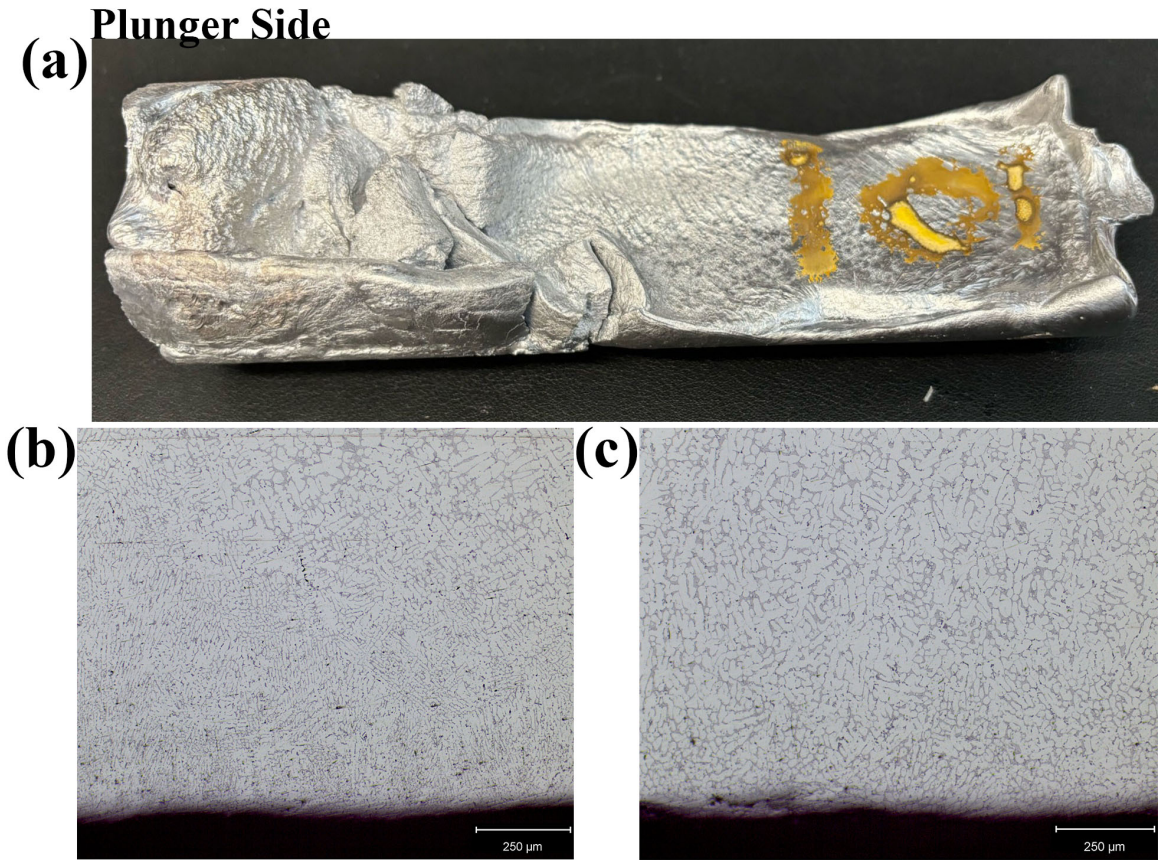

Figure 4.19: The partial shot log from the RS-3 trial. In (a), a picture of the log shows the plunger side on the left. (b) and (c) show optical images of the microstructure along the bottom of the log on the plunger side.

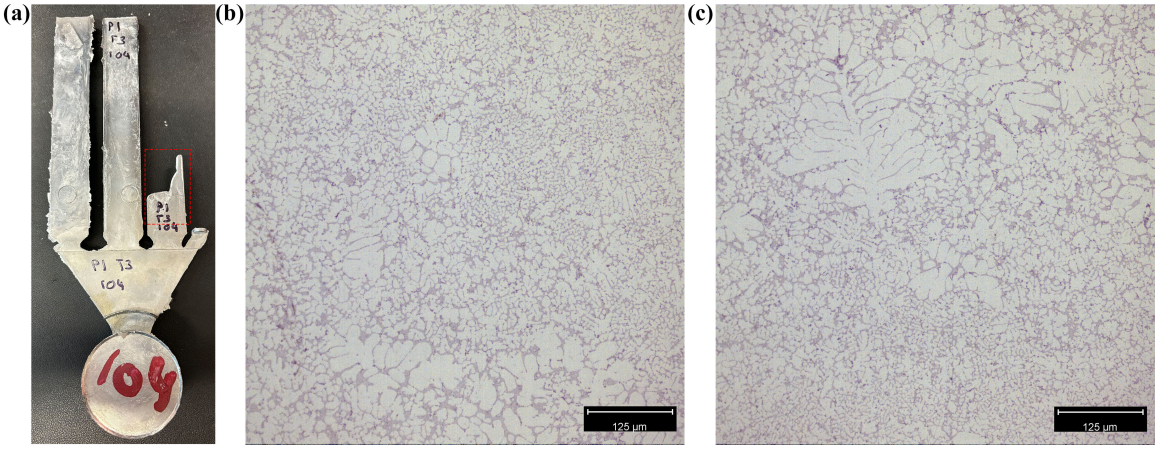

Figure 4.20: The partially filled sample from the Phase 1 trial. (a) displays the sample, while (b) and (c) are optical images of the microstructure taken from the 3 mm plate located within the red box in (a).

Partial shots can also result from other methods. Figure 4.20 showcases a sample that was incompletely filled due to inappropriate casting parameters. Specifically, the sample in Figure 4.20 was cast with a slow shot speed of 8 m/s, a fast shot speed of 12 m/s and no intensification pressure. This combination of a slow fast shot speed and lack of intensification pressure caused the metal to solidify before filling the cavity. In Figure 4.20(a), the round bar had been removed for tensile testing, and no Type II ESCs were found on the fracture surface of the round bar.

Figure 4.20(b) and (c) depict optical images taken from the 3 mm plate within the red box shown in Figure 4.20(a). Both images reveal prominent Type I ESCs. In 4.20(b), Type I ESCs are observed near the bottom of the image, while 4.20(c) shows a large dendrite near the top. These images are from the center of the plate. According to literature, Type I ESCs typically migrate towards the center of the casting sample and are less commonly found at the edges.

Melt Temperature (°C)	Shot Sleeve Temperature (°C)	Slow Shot Speed (in/s)	Fast Shot Speed (in/s)	Percent Type II ESCs (%)
728	283	12	69	0
703	270	12	68	28

Table 4.3: The average casting parameters used in the die casting trials of NS-2 alloy.

4.5.6 Mechanical Testing Results and Discussion

ESCs are difficult to detect in the castings via non-destructive methods, like CT scanning, because their chemical composition is the same as the matrix. Therefore, mechanical testing is done to determine whether Type II ESCs are present in the sample. For each casting trial, different parameters were varied to see the effect of different parameters on whether Type II ESCs would be present on the fracture surface. Table 4.3 shows the average conditions used for two castings trials. The alloy used for these trials was NS-2 which has a liquidus temperature of 602 °C. The main difference between these two trials is the temperature of the molten aluminum and the amount of ESCs found on the fracture surface. The first trial had a melt temperature of 728 °C, and the second trial had a melt temperature of 703 °C. The trial with the lower melt temperature had more Type II ESCs present. This is due to the difference of super-heat in the metal, 126 °C versus 101 °C. The greater amount of super-heat, means less solidification will occur when the metal is poured into the cooler shot sleeve. Therefore, less Type II ESCs will be formed in the shot sleeve and be pushed into the die cavity.

Comparing two different alloys cast with the same conditions except different amounts of superheat showed a similar trend. Table 4.4 shows the casting parameters used during a casting trial of A380, and a casting trial of NS-1. In both trials, the fast shot was varied and the amount of superheat used in the two trials was different. The first two rows are with the same fast shot speed of around 51 in/s. The A380 samples were cast with a superheat of 109 °C and about 70 % of the samples tested had Type II ESCs present on their fracture surfaces. While the NS-1 samples were cast with a superheat of 126 °C and did not have any Type II ESCs on their fracture surfaces. The difference in superheat greatly changed the amount of ESCs in the samples, due to less solidification in the shot sleeve. The bottom two rows in Table 4.4 were casting with a faster fast shot speed of around 67 in/s. While the two fast shot speeds are 4 in/s different, that amount is very small and is only about 0.1 m/s, so it is considered to be a similar speed. However, the superheat of the two trials shows more difference. The different amount of superheat led to the A380 samples having 50 percent of samples with Type II ESCs on the fracture surface, compared to the NS-1 samples having no Type II ESCs on the fracture surface. This is in agreement with the literature, especially Kopper and Monroe [71], who found the melt temperature had the greatest impact on solidification using computer simulations. These results are also in agreement with the computer simulation results shown in Figure 4.5. Those results use the same conditions and melt temperatures and show a greater decrease in temperature along the shot sleeve wall with a decrease in melt temperature. This decrease in temperature promotes solidification and can lead to Type II ESCs forming in the shot sleeve.

Alloy	Superheat (°C)	Shot Sleeve Temperature (°C)	Slow Shot Speed (in/s)	Fast Shot Speed (in/s)	Percent Type II ESCs (%)
A380	109	270	11	51	70
NS-1	126	270	12	52	0
A380	106	270	11	65	50
NS-1	127	270	11	69	0

Table 4.4: The average casting parameters used in the die casting trials of A380 and NS-1 alloys.

The impact of melt temperature and superheat can be seen for the same alloy cast in two different die casting trials with different melt temperatures. Table 4.5 shows the mechanical properties cast with different melt temperature. Both samples were the NS-2 alloy and were cast with a slow shot speed of 0.3 m/s, and a fast shot speed of 1.7 m/s. The liquidus temperature of this alloy is 602 °C This means that the alloy with a melt temperature of 729 °C had a superheat of 127 °C, while the other sample had a super heat of 101 °C. The sample with the higher melt temperature has higher elongation and ultimate tensile strength. This is because the sample with the lower melt temperature had a Type II ESC present on the fracture surface. The Type II ESC cause the elongation and ultimate tensile strength to decrease. The Type II ESC was able to form due to the lower melt temperature that allowed more solidification in the shot sleeve. It should be noted that the yield strength is very similar in the two samples and it does not appear that the Type II ESC has an impact on the yield strength.

The mechanical properties of the same alloys cast with the same conditions can differ due to the presence of Type II ESCs. Figure 4.21 shows the stress-strain graphs

Melt Temperature	Yield Strength (MPa)	Elongation (%)	Ultimate Tensile Strength (MPa)
729	154	3.5	285
703	151	1.9	241

Table 4.5: The mechanical properties from two NS-2 alloy casting trials. These samples were both cast with a slow shot speed of 0.3 m/s and a fast shot speed of 1.7 m/s.

With or without Type II ESC	Yield Strength (MPa)	Elongation (%)	Ultimate Tensile Strength (MPa)
Without Type II ESC	148	4.16	252
With Type II ESC	123	1.88	189

Table 4.6: The mechanical properties from the Phase 1 alloy casting trial. These samples were both cast with a slow shot speed of 0.3 m/s and a fast shot speed of 2.1 m/s.

and Table 4.6 shows the mechanical properties of two Phase 1 alloy samples cast with the same parameters. The samples were cast with a slow shot speed of 0.3 m/s and a fast shot speed of 2.1 m/s. The melt temperature was 674 °C and the shot sleeve temperature was 265 °C. Due to the presence of a Type II ESC, one of the samples has much lower properties. The elongation changes from 4.16% to 1.88% because of a Type II ESC. However, the casting parameters that were studied in this investigation are very similar between the two samples, so the reason one sample has an ESC and the other does not still needs to be investigated further.

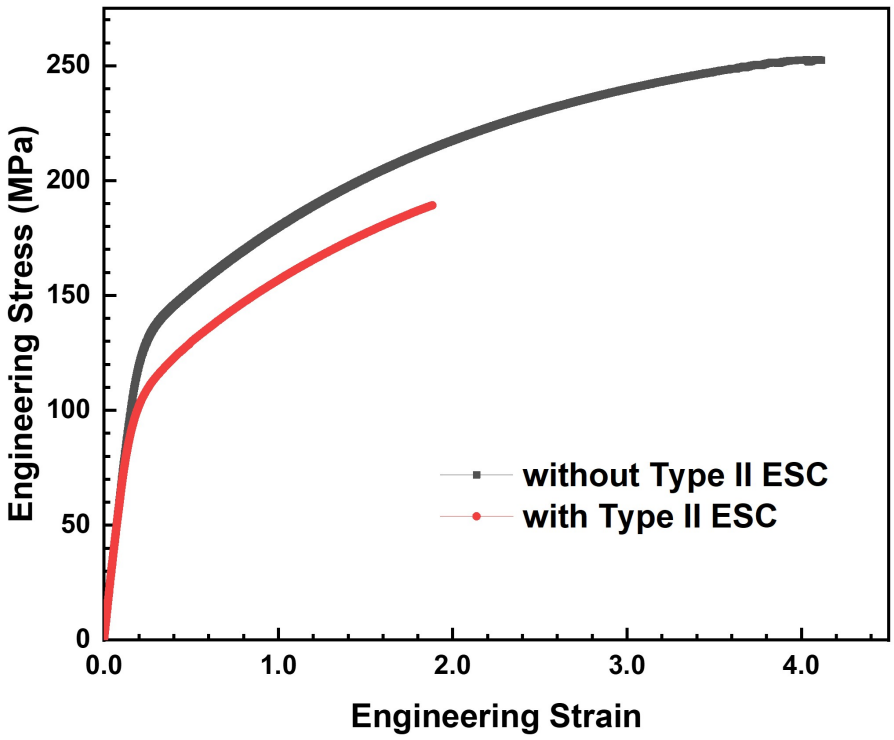

Figure 4.21: The stress-strain graphs of two samples from the Phase 1 alloy casting trial.

With or without Type II ESC	Yield Strength (MPa)	Elongation (%)	Ultimate Tensile Strength (MPa)
Without Type II ESC	122	4.83	239
With Type II ESC	109	1.46	170

Table 4.7: The mechanical properties from the Phase 1 alloy casting trial. These samples were both cast with a slow shot speed of 0.3 m/s and a fast shot speed of 2.8 m/s.

The mechanical properties from two more samples from the same casting trial are shown in Table 4.7. These samples were cast with a slow shot speed of 0.3 m/s and a fast shot speed of 2.8 m/s. The melt temperature was 675 °C and the shot sleeve temperature was 270 °C. Compared to the previous samples the fast shot speed is much faster and can cause more turbulence. In general, the properties are lower at a faster fast shot speed. The presence of a Type II ESC causes a large decrease in mechanical properties, especially elongation. However, the reason one sample had an ESC and the other did not is not known. There is still more to learn about Type II ESCs and another casting parameter not studied in this investigation is possibly the cause.

4.6 Machine Learning

This section is about the potential for using machine learning to predict the presence of Type II ESCs in die cast samples. A preliminary study on using machine learning to predict the presence of Type II ESCs in die cast samples was conducted.

4.6.1 Introduction

High Pressure Die Casting is a complex process with many different variables. Especially in industry, many parts are produced every hour and stopping due to defects can have major impacts on production [88]. Therefore machine learning can be beneficial in determining what parameters are more important and how to change the parameters to ensure quality parts.

As shown in Section 4, Type II ESCs harm the mechanical properties of die cast parts and are impacted by numerous casting parameters. Due to the large variety of parameters, machine learning (ML) is seen as a solution to designing ESC free parts. Previous researchers have used machine learning and artificial intelligence (AI) to better understand various defects in the casting process [124]. Kopper et al [88] used machine learning to predict the ultimate tensile strength of tensile bars based on various parameters in die casting. Other researchers studied the impact of processing parameters on the formability of magnesium sheet [125].

Using the die casting trials from the previous section a preliminary study on using machine learning to predict the presence of Type II ESCs was conducted. While the data collected is limited previous studies have found success using a limited dataset as well [125]. Machine learning is better for small datasets than using deep learning models [88].

4.6.2 Methods

To determine the presence of Type II ESCs in the castings tensile tests were conducted on round tensile bars, machined 3 mm plates and 5 mm plates. The

Superheat (°C)	Melt Temperature (°C)	Slow Shot Speed (m/s)	Fast Shot Speed (m/s)	Percent ESC (%)
109	697	0.28	1.29	70
106	694	0.28	1.65	50

Table 4.8: Two rows of cleaned data from the A380 trial.

extension was measured using an extensometer, with a speed of 0.005 mm/s. All samples were tested in the as-cast condition.

If an ESC is present in the sample, the fracture will occur at that location. Nine different alloy compositions were cast with varying casting parameters, including liquidus temperature, melt temperature, shot sleeve temperature, slow shot speed, fast shot speed, intensification pressure, and die temperature. At least three samples per condition were tested. The cleaned machine learning dataset used in this study is detailed in Appendix A. Samples were grouped by similar casting parameters, and the percent of Type II ESCs in each group was calculated. Table 4.8 shows an example of two rows of data from one of the A380 alloy casting trials, which has a liquidus temperature of 588 °C. The machine learning analysis also utilized shot number, and vacuum pressure. In total, the dataset includes 11 columns of data and 37 observations.

4.7 Conclusions

This study compared computer simulations, water analog experiments, and high pressure die casting trials to evaluate the influence of different die casting parameters on the formation of externally solidified crystals in die-cast aluminum alloy samples.

The investigate parameters included liquidus temperature, superheat amount, melt temperature, shot sleeve temperature, slow shot speed, and fast shot speed. These parameters were varied to observe their impact on the quantity of Type II ESCs. Additionally, die temperature, shot number, vacuum strength, and intensification pressure were monitored. These parameters were kept relatively consistent throughout the die-casting trials.

The computer simulations revealed cooling takes place within the shot sleeve and highlighted turbulence during the filling process. Both increasing the shot sleeve temperature and raising the melt temperature proved effective in minimizing solidification within the shot sleeve. While both MAGMASOFT® and Flow-3D simulations indicated cooling within the shot sleeve, they differed on where the most significant cooling occurred. MAGMASOFT® suggested more cooling near the die cavity and biscuit, whereas Flow-3D indicated greater cooling adjacent to the plunger. Additionally, MAGMASOFT® indicated cooling occurring at the bottom of the shot sleeve, whereas the Flow-3D results showed minimal cooling of the metal along the shot sleeve walls.

The simulations were also utilized to simulate turbulence in the shot sleeve during filling. Only the ProCAST results depicted a wave forming in the shot sleeve. In contrast, Flow-3D indicated the metal being pushed into the die cavity smoothly without turbulence or wave formation. However, the partial shot did exhibit turbulence in the shot sleeve. Previous studies have demonstrated that turbulence occurs in the shot sleeve during filling [86]. This turbulence can break apart ESCs before they enter the die cavity.

Water analog experiments demonstrated that particles originating closer to the die cavity and biscuit are more prone to being pushed into the die cavity during filling. These particles are also more likely to enter the 5 mm plate positioned at the center of the sample.

In the samples from the die casting trials, a finer microstructure was observed on the shot sleeve walls, and Type II ESCs were found in the biscuit of the casting samples. Type II ESCs solidify on the shot sleeve wall and are broken up by turbulence during filling. The fast cooling rate promotes a finer microstructure, which leads to a shell along the shot sleeve wall. During filling the plunger pushes the finer microstructure shell into the die cavity. Conversely, Type I ESCs solidify farther from the shot sleeve wall, where the cooling rate is slower, promoting the growth of larger grains. Type I ESCs are also pushed into the die cavity during filling, where turbulence can also break them up.

Mechanical testing results indicated that when the superheat was below 110 °C, Type II ESCs were more likely to appear on the fracture surface. Both die casting trials and computer simulations demonstrated that increasing the metal temperature is a crucial method for reducing the amount of Type II ESCs in die cast samples.

Further die casting trials are required to determine the significant parameters influencing Type II ESC formation. Additionally, investigating the formation locations of Type I ESCs would be advantageous. Better understanding of ESC formation mechanisms of ESCs will facilitate reducing ESC amount occurrence in die-cast parts and improvement of their mechanical properties.

Machine learning shows promise for advancing the understanding of ESC formation mechanisms and predicting ESC formation in die-cast samples. Expanding

machine learning models to include other die casting machines and die cavity shapes could greatly benefit the die casting industry.

Chapter 5: Summary and Future Work

Defects in both welded and cast aluminum have been studied, with their formation mechanisms identified and methods to avoid them examined. Hydrogen porosity, air entrapment, and externally solidified crystals negatively impact the mechanical properties of aluminum parts. Understanding these defects is essential for enhancing the use of aluminum in lightweight applications. This chapter will summarize the conclusion from the previous three content chapters and provide suggestions for future research to further understand and mitigate these defects.

5.1 Summary and Conclusions

5.1.1 Hydrogen Porosity in Laser Welds of Aluminum

The effect of anodized aluminum on hydrogen porosity in aluminum laser welds was investigated using a cellular automaton model. Welding was performed on 0.2 mm thick aluminum tabs, both bare and anodized, with varying laser powers and speeds. The results showed significantly higher porosity in welds made with anodized aluminum tabs compared to those with bare tabs. Anodized aluminum can introduce more hydrogen into the welds, leading to hydrogen supersaturation in the liquid metal. This supersaturation can cause hydrogen porosity to nucleate and grow. Additionally,

the aluminum oxide layer can served as heterogeneous nucleation sites for hydrogen porosity.

To reduce porosity in laser welds, several strategies can be employed: cleaning the material prior to welding, using shielding gas during welding, and opting for other corrosion resistant materials. Substituting anodized aluminum with alternatives like nickel-coated aluminum might also help in reducing hydrogen porosity in the welds.

The CA model aligns well with the results from the welding experiments. The effects of varying laser speed, power, and hydrogen concentration produced comparable outcomes in both the model and experiments. Increasing the laser speed resulted in less porosity in the weld zone due to a reduction in the melt pool size and the duration it remains molten. Conversely, increasing the laser power had the opposite effect, leading to more porosity in the weld zone. Higher laser power increases the energy density, raising the temperature of the molten aluminum and creating more liquid metal. This higher temperature allows more hydrogen to dissolve in the liquid, resulting in larger porosity. Additionally, increasing the hydrogen concentration in the liquid aluminum provides more hydrogen for diffusion into the pores, enabling them to grow larger. This effect was observed in the model by increasing the initial hydrogen concentration, which led to larger pores.

5.1.2 Air Entrapment in High Pressure Die Casting

The impact of vacuum on entrapped air during High Pressure Die Casting of aluminum was investigated using water analog experiments, computer simulations and HPDC trials. The computer simulations generally aligned well with the water analog experiments in terms of flow behavior and the effect of vacuum during the

filling process. Both methods indicated that the addition of a vacuum reduced the amount of air bubbles and entrapped air. Furthermore, a stronger vacuum proved more effective at minimizing entrapped air compared to a weaker vacuum.

Samples from the HPDC trials, cast both with and without the addition of a vacuum, were analyzed using density measurements, mechanical testing, and CT scans. The results showed that using a vacuum during die casting increased the density, tensile strength and elongation of the samples. The microstructure analysis also revealed a reduction in porosity with the addition of a vacuum. CT scans confirmed this reduction in porosity between vacuum die cast samples and those cast without a vacuum. Samples cast with the strongest vacuum exhibited the highest density and yield strength. Overall, the use of a vacuum during die casting significantly improves the quality and soundness of the cast parts.

5.1.3 Externally Solidified Crystals in Die Casting

The formation mechanism of externally solidified crystals (ESCs) and methods to mitigate their presence in aluminum high-pressure die castings were investigated. Type II ESCs form when the metal is poured into the shot sleeve and begins to solidify. The cooler shot sleeve promotes a fast cooling rate and a finer microstructure. As the metal solidifies on the shot sleeve wall, a boundary layer forms. During filling, this solidified metal layer is broken up by turbulent flow and spraying, and fragments are injected into the die cavity.

The study compared computer simulations, water analog experiments, and HPDC trials with different casting parameters. Generally, the computer simulations aligned

with the die casting results. Both indicated that higher melt temperatures decreased Type II ESCs by reducing solidification within the shot sleeve.

5.1.4 Machine Learning for ESCs Prediction

Machine learning can be used to predict the presence of Type II ESCs in die castings. Machine learning can determine the impact of multiple die casting parameters have on the formation of Type II ESCs.

5.2 Future Perspectives

5.2.1 Hydrogen Porosity in Aluminum Welds

Although shielding gas was not used in these experiments, future research on its effectiveness in reducing porosity would be valuable. Specifically, investigating the use of shielding gas when welding anodized aluminum could be beneficial. If protective gas reduces porosity welded anodized aluminum, this material could see increased use in battery applications.

Further development of the CA model would be highly beneficial. Comparing the model with a broader range of experimental data, including various laser speeds and powers, would enhance its accuracy. Incorporating different types of porosity, such as shrinkage or keyhole collapse porosity, would improve the model's utility. Additionally, integrating fluid flow dynamics and enabling the escape of hydrogen bubbles from the weld pool would significantly advance future studies.

5.2.2 Entrapped Air in Aluminum Die Casting

Conducting more water analog experiments would be beneficial for understanding the impact of vacuum. Improved sealing would allow the use of a two-stage shot

profile, better aligning with the die casting trials. Additionally, adding another liquid into the water used in these experiments to better match the viscosity and surface tension of molten aluminum would enhance the accuracy of the results.

Additional die casting trials with varying vacuum levels would be beneficial for a better understanding of the vacuum's effect. As shown in Section 3.4.4, the samples cast in this project had numerous defects that could be eliminated with better control of casting conditions. Conducting a die casting trial with controlled parameters while only varying the vacuum level would provide clearer insights into the vacuum's impact. Testing a super-vacuum could also reveal further improvements in density and mechanical properties. Furthermore, using a micro-CT machine to examine the porosity near the fracture surface and within the sample before fracture would provide valuable data.

5.2.3 Externally Solidified Crystals in Aluminum High Pressure Die Castings

Type II ESCs are very detrimental to mechanical properties. Further work to better understand which die casting parameters have the most impact would be beneficial. More die castings with varying shot sleeve temperatures would prove useful in understanding ESCs formation. Other die casting parameters including but not limited to cycle time, biscuit thickness, cavity fill time, fast shot transition location, dwell time, dosing time, and ladle pour time should be noted and studied further. While these parameters were not studied in this investigation they are still relevant to the formation of Type II ESCs.

The water analog experiments can be improved by adding different shaped and sized particles. The addition of a thin layer of some substance at the bottom of the

shot sleeve could serve as a model for the Type II ESCs forming in the shot sleeve. Additionally, testing a variety of slow shot speeds and fast shot speeds, similar to the ones tested during die casting would allow for more comparison to die casting results.

Further work also needs to be done to understand how Type I ESCs form. While not as harmful to mechanical properties as Type II, their formation mechanism should still be studied.

5.2.4 Machine Learning for Defect Prediction in Die Casting

Machine learning holds significant promise for predicting defects in die-cast samples. Future work would include expanding the database to encompass various machines and dies. Furthermore, conducting additional die casting trials with changing more parameters would enhance prediction capabilities. Collaboration with industry partners and leveraging industry data would greatly advance and refine the prediction models.

Models from the scikit-learn library should be used. Additionally, regression models should be studied due to the objective of this project.

5.2.5 Outlook

Aluminum die casting and welding hold significant potential across various industries. Despite the need for better understanding and control of defects, the growing trends of lightweighting and electric vehicles present numerous opportunities for aluminum. Welding aluminum to other metals, such as copper, is particularly crucial for applications in electric vehicles, which are expected to see a rise in production

in the coming years, thereby increasing in the demand for welded aluminum components. Additionally, the trend towards light-weighting is anticipated to expand, further enhancing the potential use of die-cast aluminum.

Already, large single-piece castings for electric vehicles are being produced, underscoring the importance of improving defect understanding. Advancements in this area will positively impact the utilization of aluminum in both electric and light-weight vehicles, and bolstering its outlook across other industries as well.

Bibliography

[1] G. Verhaeghe, P. Hilton, and S. Barnes, "Achieving low-porosity laser welds in aerospace aluminum alloy," *Aerospace Manufacturing Technology Conference*, 2003.

[2] P. Anyalebechi, "Hydrogen solubility in liquid and solid pure aluminum - critical review of measurement methodologies and reported values," *Materials Sciences and Applications*, vol. 13, no. 04, pp. 158–212, 2022.

[3] X. Cao, W. Wallace, C. Poon, and J. Immarigeon, "Research and progress in laser welding of wrought aluminum alloys in laser welding processes," *Materials and Manufacturing Processes*, vol. 18, no. 1, pp. 1–22, 2003.

[4] W. Tao and S. Yang, "Weld zone porosity elimination process in remote laser welding of aa5182-o aluminum alloy lap-joints," *Journal of Materials Processing Technology*, p. 116826, November 2020.

[5] J. Hou, R. Li, C. Xu, T. Li, and Z. Shi, "A comparative study on microstructure and properties of pulsed laser welding and continuous laser welding of al-25si-4cu-mg high silicon aluminum alloy," *Journal of Manufacturing Processes*, vol. 68, pp. 657–667, 2021.

[6] S. Auwal, S. Ramesh, F. Yusof, and S. Manladan, "A review on laser beam welding of copper alloys," *International Journal of Advanced Manufacturing Technology*, vol. 97, no. 1-4, pp. 1071–1098, 2018.

[7] L. Huang, X. Hua, D. Wu, and F. Li, "Numerical study of keyhole instability and porosity formation mechanism in laser welding of aluminum alloy and steel," *Journal of Materials Processing Technology*, vol. 252, pp. 421–431, October 2018.

[8] B. Hu and I. Richardson, "Autogenous laser keyhole welding of aluminum alloy 2024," *Journal of Laser Applications*, vol. 17, no. 2, pp. 70–80, 2005.

[9] S. Yan and Y. Shi, "Influence of laser power on microstructure and mechanical property of laser-welded al/cu dissimilar lap joints," *Journal of Manufacturing Processes*, vol. 45, no. 7089, pp. 312–321, 2019.

[10] M. Pastor, H. Zhao, R. Martukanitz, and T. Debroy, "Porosity, underfill, and magnesium loss during continuous wave nd: Yag laser welding of thin plates of aluminum alloys 5182 and 5754," *Welding Journal*, vol. 78, no. 6, pp. 207–216, 1999.

[11] A. Haboudou, P. Peyre, A. Vannes, and G. Peix, "Reduction of porosity content generated during nd:yag laser welding of a356 and aa5083 aluminum alloys," *Materials Science and Engineering A*, vol. 363, pp. 40–52, 2003.

[12] M. Courbiere, "Welding aluminum alloys," in *Metallurgy and Mechanics of Welding* (R. Blondeau, ed.), pp. 433–471, London: Wiley, 2008.

[13] D. Dispinar and J. Campbell, "Critical assessment of reduced pressure test. part 1: Porosity phenomena," *International Journal of Cast Metals Research*, vol. 17, no. 5, pp. 280–286, 2004.

[14] C. Gu, C. Ridgeway, E. Cinkilic, J. Miao, A. Klarner, Y. Lu, and A. Luo, "Predicting gas and shrinkage porosity in solidification microstructure: A coupled three-dimensional cellular automaton model," *Journal of Materials Science and Technology*, vol. 49, pp. 91–105, 2020.

[15] J. Lancaster, *Metallurgy of Welding*. Allen Unwin, fourth ed., 1987.

[16] K. Leong, K. Sabo, B. Altshuller, T. Wilkinson, and C. Albright, "Laser beam welding of 5182 aluminum alloy sheet," *Journal of Laser Applications*, vol. 11, no. 3, pp. 109–118, 1999.

[17] M. Vyskoc, M. Sahul, and M. Sahul, "Effect of shielding gas on the properties of aw 5083 aluminum alloy laser weld joints," *Journal of Materials Engineering and Performance*, vol. 27, no. 6, pp. 2993–3006, 2018.

[18] S. Wu, X. Yu, R. Zuo, W. Zhang, H. Xie, and J. Jiang, "Porosity, element loss, and strength model on softening behavior of hybrid laser arc welded al-zn-mg-cu alloy with synchrotron radiation analysis," *Welding Journal*, vol. 92, no. 3, pp. 64–72, 2013.

[19] L. Huang, X. Hua, D. Wu, and F. Li, "Experimental investigation and numerical study on the elimination of porosity in alumnium alloy laser welding and laser-gma welding," *Journal of Materials Engineering and Performance*, vol. 28, no. 3, pp. 1618–1627, 2019.

[20] M. Atabki, N. Yazdian, and R. Kovacevic, "Partial penetration laser-based welding of aluminum alloy (aa 5083-h32)," *Optik*, vol. 127, no. 16, pp. 6782–6804, 2016.

[21] C. Tan, Y. Liu, B. Xu, H. Wang, F. Liu, X. Gong, Z. Zeng, B. Chen, and X. Song, "Numerical and experimental study of thermal fluid flow and keyhole dynamic in laser welding of aluminum alloy assisted by electromagnetic field," *Optics and Laser Technology*, vol. 157, p. 108718, 2023.

[22] Z. Wang, H. Cao, H. Li, D. Wang, H. Xia, H. Butt, M. Li, and D. Liu, "Effects of laser welding parameters on the porosity and acicular phaser in sicp/6092 aluminum matrix composite welded joints," *Journal of Materials Research and Technology*, vol. 23, pp. 5127–5141, 2023.

[23] Y. Kang, X. Zhan, S. He, T. Liu, and L. Sun, "Poroisty-grain growth relationships in the laser beam deep penetration welding of 6061 aluminum alloy," *Journal of Adhesion Science and Technology*, vol. 35, no. 13, pp. 1372–1392, 2021.

[24] K. Mathivanan and P. Plapper, "Correlation of optical signal during laser fusion welding of copper to aluminum," *Journal of Laser Applications*, vol. 33, no. 1, p. 012037, 2021.

[25] W. Huang, H. Wang, T. Rinker, and W. Tan, "Investigation of metal mixing in laser keyhole welding of dissimilar metals," *Materials and Design*, vol. 195, p. 109056, 2020.

[26] A. Fritzsche, K. Hilgenberg, F. Teichmann, H. Pries, K. Dilger, and M. Rethmeier, "Improved degassing in laser beam welding of aluminum die casting by an electromagnetic field," *Journal of Materials Processing Technology*, vol. 253, pp. 51–56, June 2018.

[27] A. Paleocrassas and J. Tu, "Inherent instability investigation for low speed laser welding of aluminum using a single-mode fiber laser," *Journal of Materials Processing Technology*, vol. 210, no. 10, pp. 1411–1418, 2010.

[28] J. Han, Y. Shi, G. Zhang, K. Volodymyr, and W. Le, "Minimizing defects and controlling the morphology of laser welded aluminum alloys using power modulation-based laser beam oscillation," *Journal of Manufacturing Processes*, vol. 83, pp. 49–59, July 2022.

[29] T. Kikuchi, Y. Suzuki, M. Iwai, and R. Suzuki, "Anodizing aluminum and its alloys in etidronic acid to enhance their corrosion resistance in a sodium chloride solution," *Journal of the Electrochemical Society*, vol. 167, no. 12, p. 121502, 2020.

[30] J. Han, Y. Shi, J. Guo, K. Volodymyr, W. Le, and F. Dai, "Porosity inhibition of aluminum alloy by power-modulated laser welding and mechanism analysis," *Journal of Manufacturing Processes*, vol. 102, pp. 827–838, 2023.

[31] H. Kwon, U. Shah, X. Liu, T. Rinker, and W. Cai, "Ultrasonic-assisted resistance spot welding of multilayered al foil stacks for li-ion battery applications," *Journal of Materials Processing Technology*, vol. 317, p. 117990, 2023.

[32] K. Ono, K. Adachi, I. Miyamoto, and I. Takashi, "Influence of oxide film on weld characteristics of mild steel in carbon dioxide laser welding," *Journal of Laser Applications*, vol. 73, no. 2002, pp. D83–D91, 2018.

[33] P. Yousefian and M. Tiryakioglu, "Pore formation during solidification of aluminum: Reconciliation of experimental observations, modeling assumptions, and classical nucleation theory," *Metallurgical and Materials Transactions A: Physical Metallurgy and Materials Science*, vol. 49, pp. 563–575, 2018.

[34] S. Hu, A. Haselhuln, Y. Ma, Y. Li, B. Carlson, and Z. Lin, "Influencing mechanism of inherent aluminum oxide film on coach peel performance of baked al-steel rsw," *Materials Design*, vol. 197, p. 109250, 2021.

[35] M. El-Sayed, H. Hassanin, and K. Essa, "Bifilm defects and porosity in al cast alloys," *The International Journal of Advanced Manufacturing Technology*, vol. 86, pp. 1173–1179, 2016.

[36] L. Liu, A. Samuel, F. Samuel, H. Doty, and S. Valtierra, "Influence of oxides on porosity formation in sr-treated al-si casting alloys," *Journal of Materials Science*, vol. 38, pp. 1255–1267, 2003.

[37] W. Griffiths and R. Raiszadeh, "Hydrogen, porosity and oxide film defects in liquid al," *Journal of Materials Science*, vol. 44, pp. 3402–3407, March 2009.

[38] C. Gu, C. Ridgeway, M. Moodispaw, and A. Luo, "Multi-component numerical simulation and experimental study of dendritic growth during solidification processing," *Journal of Materials Processing Technology*, vol. 286, p. 116829, July 2020.

[39] Q. Zhang, D. Sun, S. Pan, and M. Zhu, "Microporosity formation and dendrite growth during solidification of aluminum alloys: modeling and experiment," *International Journal of Heat and Mass Transfer*, vol. 146, p. 118838, 2020.

[40] C. Gu, Y. Lu, E. Cinkilic, J. Miao, A. Klarner, X. Yan, and A. Luo, "Predicting grain structure in high pressure die casting of aluminum alloys: A coupled cellular automaton and process model," *Computational Materials Science*, vol. 161, pp. 64–75, October 2019.

[41] C. Gu, Y. Lu, C. Ridgeway, E. Cinkilic, and A. Luo, "Three-dimensional cellular automaton simulation of coupled hydrogen porosity and microstructure during solidification of ternary aluminum alloys," *Scientific Reports*, pp. 1–12, August 2019.

[42] E. Cinkilic, A. Klarner, Y. Lu, J. Brevick, A. Luo, M. Zolnowski, X. Yan, K. Sadayappan, and G. Birsan, "High integrity structural aluminum castings produced with vacuum high pressure die casting," *Transactions of North American Die Casting Association*, pp. 24–29, November 2018.

[43] D. Twarog, D. Apelian, and A. Luo, *High Integrity Casting of Lighweight Components*. North American Die Casting Association, 2016.

[44] A. Klarner, *Development of Mg-Al-Sn and Mg-Al-Sn-Si alloys and optimization of super vacuum die casting process for lightweight applications*. PhD thesis, Ohio State University, 2018.

[45] P. Cleary, J. Ha, M. Prakash, and T. Nguyen, "Short shots and industrial case studies: Understanding fluid dlow and solidification in high pressure die casting," *Applied Mathematical Modelling*, vol. 34, no. 8, pp. 2018–2033, 2010.

[46] K. Dou, E. Lordan, Y. Zhang, A. Jacot, and Z. Fan, "A complete computer aided engineering (cae) modelling and optimization of high pressuere die casting (hpdc) process," *Journal of Manufacturing Processes*, vol. 60, pp. 435–446, October 2020.

[47] Y. Karni, *Selection of process variables for die casting*. PhD thesis, Ohio State University, 1991.

[48] S. Janudom, J. Wannasin, J. Basem, and S. Wisutmethangoon, "Characterization of flow behavior of semi-solid slurries containing low solid fractions in high-pressure die casting," *Acta Materialia*, vol. 61, no. 16, pp. 6267–6275, 2013.

[49] S. Li, D. Li, X. Zeng, and W. Ding, "Microstructure and mechanical properties of mg-6gd-3y-0.5zr alloy processed by high-vacuum die-casting," *Transactions of Nonferrous Metals Society of China*, vol. 24, no. 12, pp. 3769–3776, 2014.

[50] M. Yoo, J. Song, J. Oh, S. Kang, K. Kim, S. Yang, and M. Moon, "Development of a bus armrest fabrication process with a high-vacuum, high-pressure die casting process using the am60 alloy," *Robotics and Computer-Integrated Manufacturing*, vol. 55, pp. 154–159, November 2019.

[51] H. Cao, M. Hao, C. Shen, and P. Liang, "The influence of different vacuum degree on the porosity and mechanical properties of aluminum die casting," *Vacuum*, vol. 146, pp. 278–281, 2017.

[52] C. Hu, H. Zhao, X. Wang, and J. Fu, "Microstructure and properties of alsi12fe alloy high pressure die-castings under different vacuum levels," *Vacuum*, vol. 180, p. 109561, June 2020.

[53] H. Cao, Z. Luo, C. Wang, J. Wang, T. Hu, L. Xiao, and J. Che, "The stress concentration mechanism of pores affecting the tensile properties in vacuum die casting metals," *Materials*, vol. 13, no. 13, p. 3019, 2020.

[54] X. Niu, B. Hu, I. Pinwill, and H. Li, "Vacuum assisted high pressure die casting of aluminum alloys," *Journal of Materials Processing Technology*, vol. 105, no. 1-2, pp. 119–127, 2000.

[55] H. Bo, X. Shoumei, M. Murakami, Y. Matsumoto, and S. Ikeda, "Study on vacuum die casting process of aluminum alloys," *World Foundry Congress*, pp. 1–9, 2006.

[56] B. Wang and S. Xiong, "Effect of multi-step slow shot speed on microstructure of vacuum die cast az91d magnesium alloy," *Transactions of Nonferrous Metals Society of China*, vol. 25, no. 2, pp. 375–380, 2015.

[57] X. Dong, X. Zhu, and S. Ji, "Effect of super vacuum assisted high pressure die casting on the repeatability of mechanical properties of al-si-mg-mn die-cast alloys," *Journal of Materials Processing Technology*, vol. 266, pp. 105–113, August 2019.

[58] D. Brungs, "Light weight design with light metal castings," *Materials and Design*, vol. 18, no. 4-6, pp. 285–291, 1997.

[59] T. Magnusson and L. Arnberg, "Density and solidification shrinkage of hypoeutectic aluminum-silicon alloys," *Metallurgical and Materials Transactions*, vol. 250, no. 10, p. 2605, 2001.

[60] X. Jiao, C. Liu, J. Wang, Z. Guo, J. Wang, Z. Wang, J. Gao, and S. Xiong, "On the characterization of microstructure and fracture in a high-pressure die-casting al-10wt

[61] S. Lee and A. Gokhale, "Formation of gas induced shrinkage porosity in mg-alloy high-pressure die-castings," *Scripta Materialia*, vol. 55, no. 4, pp. 387–390, 2006.

[62] Z. Li, Y. Jing, H. Guo, X. Sun, K. Yu, A. Yu, X. Jiang, and X. Yang, "Study of 3d pores and its relationship with crack initiaion factors of aluminum alloy die castings," *Metallurgical and Materials Transactions B: Metallurgy and Materials Processing Science*, vol. 50, no. 3, pp. 1204–1212, 2019.

[63] R. Helenius, O. Lohne, L. Arnberg, and H. Laukli, "The heat transfer during filling of a high-pressure die-casting shot sleeve," *Materials Science and Engineering A*, vol. 413-414, pp. 52–55, 2005.

[64] X. Jiao, Y. Zhang, J. Wang, H. Nishat, Y. Liu, W. Liu, H. Chen, and S. Xiong, "Characterization of externally solidified crystals in a high-pressure die-cast alsi10mnmg alloy and their effect on porosities and mechanical properties," *Journal of Materials Processing Technology*, vol. 298, p. 117299, April 2021.

[65] C. Gourlay, H. Laukli, and A. Dahle, "Segregation band formation in al-si die castings," *Metallurgical and Materials Transactions A: Physical Metallurgical and Materials Science*, vol. 35, no. 9, pp. 2881–2891, 2004.

[66] G. Timelli and A. Fabrizi, "The effects of microstructure heterogeneities and casting defects on the mechanical properties of high-pressure die-cast alsi9cu3(fe) alloys," *Metallurgical and Materials Transactions A: Physical Metallurgy and Materials Science*, vol. 45, no. 12, pp. 5486–5498, 2014.

[67] C. Bi, S. Xiong, X. Li, and Z. Guo, "Development of a fluid-particle model in simulating the motion of external solidified crystals and the evolution of defect bands in high-pressure die casting," *Metallurgical and Materials Transactions B: Process Metallurgy and Materials Processing Science*, vol. 47, no. 2, pp. 929–947, 2016.

[68] Q. Han and J. Zhang, "Fluidity of alloys under high-pressure die casting conditions: flow-choking mechanisms," *Metallurgical and Materials Transactions B: Process Metallurgy and Materials Processing Science*, vol. 51, no. 4, pp. 1795–1804, 2020.

[69] Z. Yuan, Z. Guo, and S. Xiong, "Effect of as-cast microstructure heterogeneity on aging behavior of a high-pressure die-cast a380 alloy," *Materials Caracterization*, vol. 135, pp. 278–286, November 2018.

[70] S. Otarawanna, C. Gourlay, H. Laukli, and A. Dahle, "The thicknesss of defect bands in high-pressure die castings," *Materials Characterization*, vol. 60, pp. 1432–1441, 2009.

[71] A. Kopper and A. Monroe, "Reducing externally solidified products - essential for structural die castings," *NADCA Transactions*, 2015.

[72] K. Dou, E. Lordan, Y. Zhang, A. Jacot, and Z. Fan, "A novel approach to optimize mechanical properties for aluminum alloy in high pressure die casting (hpdc) process combining experiment and modelling," *Journal of Materials Processing Technology*, vol. 296, p. 117193, April 2021.

[73] X. Qin, Y. Su, J. Chen, and L. Liu, "Finite element analysis for die casting parameters in high-pressure die casting process," *China Foundry*, pp. 2–7, 2019.

[74] P. Zhang, Z. Li, B. Liu, and W. Ding, "Tensile properties and deforming behaviors of a new aluminum alloy for high pressure die casting," *Journal of Materials Science and Technology*, vol. 33, no. 4, pp. 367–378, 2017.

[75] C. Jin and C. Kang, "Fabrication process analysis and experimental verification for aluminum bipolar plates in fuel cells by vacuum die-casting," *Journal of Power Sources*, vol. 196, no. 20, pp. 8241–8249, 2011.

[76] S. Jeong, C. Jin, H. Seo, J. Kim, and C. Kang, "Mold structure design and casting simulation of the high-pressure die casting for aluminum automotive clutch housing manufacturing," *International Journal of Advanced Manufacturing Technology*, vol. 84, no. 5-8, pp. 1561–1572, 2016.

[77] D. Gunasegaram, B. Finnin, and F. Polivka, "Melt flow velocity in high pressure die casting: its effect on microstructure and mechanical properties in an al-si alloy," *Materials Science and Technology*, vol. 23, no. 7, pp. 847–856, 2007.

[78] M. Rudach, A. Buhrig-Polaczek, and U. Vroomen, "Simulation driven analysis of shot end operating parameters and their impact on the fluid dynamical evolution of the alloy in a horizontal cold chamber hpdc process," *American Foundry Society*, vol. 010, pp. 1–11, 2020.

[79] L. Wang, T. Nguyen, G. Savage, and C. Davidson, "Thermal and flow modelling of ladling and injection in high pressure die casting process," *International Journal of Cast Metals Research*, vol. 16, no. 4, pp. 409–417, 2003.

[80] P. Cleary, G. Savage, J. Ha, and M. Prakash, "Flow analysis and validation of numerical modeling for a thin walled high pressure die casting using sph," *Computational Particle Mechanics*, vol. 1, no. 3, pp. 229–243, 2014.

[81] P. Cleary, J. Ha, M. Prakash, and T. Nguyen, "3d sph flow predictions and validation for high pressure die casting of automotive compornets," *Applied Mathematical Modelling*, vol. 130, no. 11, pp. 1406–1427, 2006.

[82] J. Hao, Y. Nie, F. Ji, and F. Cha, "Two-phase flow modeling of air entrapment in high pressure die casting considering air compressibility and surface tension," *Computers and Fluids*, vol. 190, pp. 192–205, 2019.

[83] R. Zamora, F. Faura, J. Lopez, and J. Hernandez, "Experimental verification of numerical predictions for the optimum plunger speed in the slow phase of a high-pressure die casting machine," *International Journal of Advanced Manufacturing Technology*, vol. 33, no. 3-4, pp. 266–276, 2007.

[84] A. Viswanath, M. Manu, S. Savithri, and U. Pillai, "Numberical simulation and experimental validation of free surface flows during low pressure casting

process," *Journal of Materials Processing Technology*, vol. 244, pp. 320–330, 2017.

[85] B. Park, *Effect of cavity pre-fill and geometry on filling patterns and air entrapment in cold chamber die casting*. PhD thesis, Ohio State University, 2001.

[86] L. Garber, "Theoretical analysis and experimental observation of air entrapment during cold chamber filling," *Die Casting Engineer*, vol. 26, no. 3, pp. 14–22, 1982.

[87] S. Hao, B. Hu, X. Niu, and R. Pehlke, "Atomization in high pressure die casting - a problem and a challenge," *Die Casting Engineer*, vol. 41, no. 5, 1998.

[88] A. Kopper, R. Karkare, R. Paffenroth, and D. Apelian, "Model selection and evaluation for machine learning: Deep learning in materials processing," *Integrating Materials and Manufacturing Innovation*, vol. 9, pp. 287–300, 2020.

[89] E. Lorfan, J. Lazaro-Nebreda, Y. Zhang, and Z. Fan, "Effective degassing for reduced variability in high-pressure die casting performance," *JOM*, vol. 71, no. 2, pp. 824–830, 2019.

[90] J. Zhou and H. Tsai, "Porosity formation and prevention in pulsed laser welding," *Journal of Heat Transfer*, vol. 129, no. 8, pp. 1014–1024, 2007.

[91] Y. Aoki, H. Fujii, and K. Nogi, "Effect of atomic oxygen exposure on bubble forming in aluminum alloy," *Journal of Materials Sciences*, vol. 39, no. 5, pp. 1779–1783, 2004.

[92] L. Jiang, L. Shi, Y. Lu, Y. Xiang, C. Zhang, and M. Gao, "Effects of sidewall grain growth on pore formation in narrow gas oscillating laser welding," *Optics and Laser Technology*, vol. 156, p. 108483, April 2022.

[93] M. Miyagi, Y. Kawahito, H. Kawakami, and T. Shoubu, "Dynamics of solid-liquid interface and porosity formation determined through x-ray phase-contrast in laser welding of pure al," *Journal of Materials Processing Technology*, vol. 250, pp. 9–15, June 2017.

[94] in *Welding Handbook* (L. Griffing, ed.), pp. 69.1–69.161, American Welding Society, sixth ed., 1972.

[95] D. Cheever, D. Howden, and R. Monroe, "Welding 99.9999 percent pure aluminum," *Welding Journal*, pp. 25–30, 1971.

[96] M. Mazur, "Porosity in aluminum welds," in *Encyclopedia of Aluminum and Its Alloys*, p. 1973, 2018.

[97] C. Gu, Y. Lu, and A. Luo, "Three-dimensional visualization and quantification of microporosity in aluminum castings by x-ray micro-computed tomography," *Journal of Materials Science and Technology*, vol. 65, pp. 99–107, 2021.

[98] Y. Zhao, X. Li, Z. Liu, J. Wang, Y. Li, and X. Zhan, "Stability enhancement of molten pool and keyhole for 2196 al-li alloy using fiber diode laser hybrid welding," *Journal of Manufacturing Processes*, vol. 85, pp. 724–741, 2023.

[99] W. Ke, X. Bu, J. Oliveira, W. Xu, Z. Wang, and Z. Zeng, "Modeling and numerical study of keyhole-induced porosity formation in laser beam oscillating welding of 5a06 aluminum alloy," *Optics and Laser Technology*, vol. 133, p. 106540, 2021.

[100] L. Yuan, L. Peng, J. Han, B. Liu, Y. Wu, and J. Chen, "Effect of cu addition on microstructures and tensile properties of high-pressure die-casting al-5.5mg-0.7mn alloy," *Journal of Materials Science Technology*, vol. 35, no. 6, pp. 1017–1026, 2019.

[101] F. Bonollo, N. Gramegna, and G. Timelli, "High-pressire die-casting: Contradictions and challenges," *JOM*, vol. 67, no. 5, pp. 901–908, 2015.

[102] A. Niklas, S. Orden, A. Bakedano, M. da Silva, E. Nogués, and A. Fernández-Calvo, "Effect of solution heat treatment on gas porosity and mechanical properties in a die cast step test part manufactured with a new alsi10mnmg(fe) secondary alloy," *Materials Science and Engineering A*, vol. 667, pp. 376–382, 2016.

[103] X. Jiao, C. Liu, Z. Guo, G. Tong, S. Ma, Y. Bi, Y. Zhang, and S. Xiong, "The characterization of fe-rich phases in a high-pressure die cast hypoeutectic aluminum-silicon alloy," *Journal of Materials Science and Technology*, vol. 51, pp. 54–62, 2020.

[104] Y. Zhou, Z. Guo, and S.-M. Xiong, "Effect of runner design on the externally solidified crystals in vacuum die-cast mg-3.0nd-0.3zn-0.6zr alloy," *Journal of Materials Processing Technology*, vol. 267, pp. 366–375, December 2019.

[105] L. Wan, Z. Hu, S. Wu, and X. Liu, "Mechanical properties and fatigue behavior of vacuum-assist die cast almgsimn alloy," *Materials Science and Engineering A*, vol. 576, pp. 252–258, 2013.

[106] P. Szalva and I. Orbulov, "Fatigue testing and non-destructive characterization of alsi9cu3(fe) die cast specimens by computer tomography," *Fatigue and Fracture of Engineering Materials and Structures*, vol. 43, no. 9, pp. 1949–1958, 2020.

[107] W. Yu, C. Ma, Y. Ma, and S. Xiong, "Correlation of 3d defect-band morphologies and mechanical properties in high pressure die casting magnesium alloy," *Journal of Materials Preocessing Technology*, vol. 288, p. 116853, June 2021.

[108] P. Szalva and I. Orbulov, "Effects of artificial and natural defects on fatigue strength of a cast aluminum alloy," *Fatigue and Fracture of Engineering Materials and Structures*, vol. 44, no. 11, pp. 3214–3218, 2021.

[109] R. Liu, J. Zheng, L. Godlewski, J. Zindel, M. Li, W. Li, and S. Huang, "Influence of pore characteristics and eutectic particles on the tensile properties of al-si-mn-mg high pressure die casting alloy," *Materials Science and Engineering A*, vol. 783, March 2020.

[110] P. Szalva and I. Orbulov, "Influence of vacuum support on the fatigue life of alsi9cu3(fe) aluminum alloy die castings," *Journal of Materials Engineering and Performance*, vol. 29, no. 9, pp. 4585–5695, 2020.

[111] Y. Zhang, E. Lordan, K. Dou, S. Wang, and Z. Fan, "Influence of porosity characteristics on the variabilty in mechanical properites of high pressure die casting (hpdc) alsi7mgmn alloys," *Journal of Manufacturing Processes*, vol. 56, pp. 500–509, March 2020.

[112] P. Sharifi, J. Jamali, K. Sadayappan, and J. Wood, "Grain size distribution and interfacial heat transfer coefficient during solidification of magnesium alloys using hihg pressure die casting process," *Journal of Materials Science and Technology*, vol. 34, no. 2, pp. 324–334, 2018.

[113] Y. Cengel and M. Boles, *Thermodynamics: An Engineering Approach*. New York, NY: McGraw-Hill, 2014.

[114] *Primary aluminum foundry alloys*. Rio Tinto, fourth ed., 2019.

[115] H. Kato, T. Suzuki, Y. Annou, and K. Kageyama, "Nondestructive detection of cold flakes in aluminum alloy die-cast plate with ultrasonic measurement," *Materials Transactions*, vol. 45, no. 7, pp. 2403–2409, 2004.

[116] Y. Jiang, H. Zheng, F. Liu, and H. Zhao, "Effect of zn addition on the microstructural heterogeneity and mechanical properties of vacuum-assisted high-pressure die casting al-si-mg-cu alloys," *Advanced Engineering Materials*, vol. 25, p. 2201457, 2023.

[117] H. Laukli, O. Lohne, S. Sannes, H. Gjestland, and L. Arnberg, "Grain size distribution in a complex am60 magnesium alloy die casting," *International Journal of Cast Metals Research*, vol. 16, no. 6, pp. 515–521, 2003.

[118] S. Ji, Y. Wang, D. Watson, and Z. Fan, "Microstructural evolution and solidification behavior of al-mg-si alloy in high-pressure die casting," *Metallurgical and Materials Transactions A: Physical Metallurgy and Materials Science*, vol. 44, pp. 3185–3197, July 2013.

[119] B. Wang and S. Xiong, "Effects of shot speed and biscuit thickness on externally solidified crystals of high-pressure die cast am60b magnesium alloy," *Transactions of Nonferrous Metals Society of China*, vol. 21, no. 4, pp. 767–772, 2011.

[120] K. Dou, Y. Zhang, E. Lordan, A. Jacot, and Z. Fan, "Understanding the initial solidification behavior for al-si alloy in cold chamber high-pressure die casting (cc-hpdc) process combining experimental and modeling approach," *Metallurgical and Materials Transactions A: Physical Metallurgy and Materials Science*, vol. 53, no. 8, pp. 3110–3124, 2022.

[121] Y. Hao, H. Zhao, X. Shen, X. Wang, and H. Zheng, "Simulation of alpha-al grain formation in high vacuum die-casting al-si-mg alloys with multi-component quantitative cellular automaton method," *China Foundry*, vol. 19, no. 2, pp. 99–108, 2022.

[122] A. Aziz Ahamed, H. Kato, K. Kageyama, and T. Komazaki, "Acoustic visualization of cold flakes and crack propagation in aluminum alloy die-cast plate," *Materials Science and Engineering A*, vol. 423, pp. 313–323, 2006.

[123] B. Dybowski, A. Kielbus, and L. Poloczek, "Effects of die-casting defects on the blister formation in high-pressure die-casting aluminum structural components," *Engineering Failure Analysis*, vol. 150, p. 107223, 2023.

[124] Z. Li, H. Tan, A. Jarfors, P. Jansson, and L. Lattanzi, "Smart-cast: An ai-based system for semisolid casting process control," *Procedia Computer Science*, pp. 2440–2447, 2024.

[125] R. Yang, R. Shi, and A. Luo, "Unveilding the alloying-processing-microstructure correlations in high-formability sheet magnesium alloys," *Metals*, vol. 13, no. 4, 2023.

Appendix A: Type II Machine Learning Data

The cleaned dataset used in the Machine Learning model. Each table is for each alloy used. The vacuum used is between 31-50 mbar. The super-heat is the melt temperature minus the liquidus temperature. The liquidus temperatures for the alloys used are listed in Table 4.2.

Descriptor	Range	Unit
Melt Temperature	671-729	°C
Superheat	70-128	°C
Slow Shot Speed	8-12	in/s
Fast Shot Speed	14-219	in/s
Intensification Pressure	0-17193	psi
Die Temperature	150-205	°C
Percentage of ESCs Present	0-75	%

Table A.1: The data for the Phase 1 alloy used in Machine Learning.

Descriptor	Range	Unit
Melt Temperature	688-697	°C
Superheat	100-109	°C
Slow Shot Speed	11-12	in/s
Fast Shot Speed	51-113	in/s
Intensification Pressure	12000	psi
Die Temperature	185-209	°C
Percentage of ESCs Present	50-100	%

Table A.2: The data for the A380 alloy used in Machine Learning.

Descriptor	Range	Unit
Melt Temperature	704-743	°C
Superheat	86-125	°C
Slow Shot Speed	11-12	in/s
Fast Shot Speed	51-52	in/s
Intensification Pressure	12000-18750	psi
Die Temperature	115-170	°C
Percentage of ESCs Present	0	%

Table A.3: The data for the EZCAST alloy used in Machine Learning.

Descriptor	Range	Unit
Melt Temperature	728-729	°C
Superheat	126-127	°C
Slow Shot Speed	11-12	in/s
Fast Shot Speed	52-69	in/s
Intensification Pressure	13500-13637	psi
Die Temperature	170-190	°C
Percentage of ESCs Present	0	%

Table A.4: The data for the NS-1 alloy used in Machine Learning.

Descriptor	Range	Unit
Melt Temperature	703-730	°C
Superheat	101-128	°C
Slow Shot Speed	11-12	in/s
Fast Shot Speed	21-169	in/s
Intensification Pressure	12700-13702	psi
Die Temperature	185-265	°C
Percentage of ESCs Present	0-28	%

Table A.5: The data for the NS-2 alloy used in Machine Learning.

Descriptor	Range	Unit
Melt Temperature	726-727	°C
Superheat	124-125	°C
Slow Shot Speed	11-12	in/s
Fast Shot Speed	52-69	in/s
Intensification Pressure	13326-13702	psi
Die Temperature	173-180	°C
Percentage of ESCs Present	0	%

Table A.6: The data for the NS-3 alloy used in Machine Learning.

Descriptor	Range	Unit
Melt Temperature	737-738	°C
Superheat	127	°C
Slow Shot Speed	12	in/s
Fast Shot Speed	50-53	in/s
Intensification Pressure	12716-12977	psi
Die Temperature	198-205	°C
Percentage of ESCs Present	0-50	%

Table A.7: The data for the RS-1-3 alloys used in Machine Learning.